Theory of Josephson Junction Resonators

Author:
Thomas George McDermott

Supervisors:
Dr. Eros Mariani
Prof. Saverio Russo

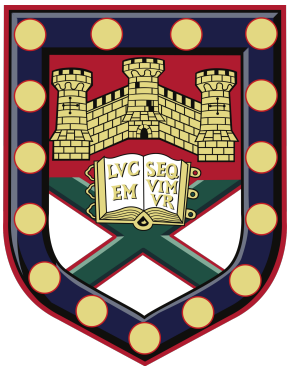

Submitted by Thomas George McDermott to the University of Exeter as a thesis for the degree of Doctor of Philosophy in Physics in September 2019.

I certify that all material in this thesis which is not my own work has been identified and that no material has previously been submitted and approved for the award of a degree by this or any other University.

Signature: _____

for my parents and brother

Abstract

Superconductivity is a result of quantum coherence at macroscopic scales. Two superconductors separated by a metallic or insulating weak link exhibit the AC Josephson effect: the conversion of a DC voltage bias into an AC supercurrent. This current may be used to activate mechanical oscillations in a suspended weak link, acting as an electromechanical resonator. As the DC voltage bias condition is remarkably difficult to achieve in experiments, here the experimentally relevant purely DC current bias case is analyzed thoroughly. It shall be demonstrated that the Josephson effect can be exploited to activate and detect mechanical oscillations, eliminating the need for AC bias conditions that are generally required for nanoelectromechanical systems (NEMS). The coupling between the electronic and mechanical degrees of freedom may be tuned by an external magnetic field, allowing the exploration of the Josephson effect in two distinct coupling regimes. In the weak coupling regime, Shapiro-like plateaus and mechanically induced hysteresis loops develop in the junction's current-voltage (I-V) characteristic which allow for precision measurements of the resonator's resonance frequency by simple DC voltage measurements. In contrast, in the strong coupling regime there are sudden mechanically induced transitions to a zero voltage state which will be explained by energy sharing between the electronic and mechanical degrees of freedom. These transitions are intimately linked to the mechanical damping of the resonator, and may be used to determine the junction's quality factor, again with only DC voltage measurements. It is further revealed that these sudden transitions may be eliminated by using a setup consisting of two suspended weak links connected in parallel forming a superconducting quantum interference device (SQUID), and tuning the external magnetic flux appropriately. Finally, the quantum nature of Josephson junctions is explored more thoroughly by considering Bloch-like oscillations that develop in the junction. These oscillations, when coupled to mechanical vibrations, generate non-classical mechanical states that are intimately linked to the quantum dynamics of the junction.

Contents

1 Introduction

Superconductivity is a macroscopic quantum phenomenon in which an electrical current flows without dissipation. Below a critical temperature, electrons bind together into so-called Cooper pairs due to an effective attractive interaction mediated by phonons. These electron pairs form a macroscopic condensate characterized by a finite energy gap in its quasiparticle energy spectrum. The Cooper pair condensate can thus flow without producing dissipation, leading to a zero resistance supercurrent [1].

A mini energy gap may open in a normal metal's density of states when it is placed in close proximity to a superconductor. This proximity effect is due to electrons in the normal metal picking up correlations from the superconductor, resulting in a finite density of Cooper pairs inside the normal metal [2]. A supercurrent may then flow between two superconductors separated by an insulating or metallic weak link, via either direct tunneling of Cooper pairs or by the proximity effect in a phenomenon known as the Josephson effect. Brian Josephson made this surprising discovery in 1962 when he was a PhD student and he was subsequently awarded the Nobel prize [3]. Josephson also predicted that if a DC voltage bias is maintained across such a (Josephson) junction, the supercurrent alternates due to interference between the macroscopic wave functions of the two superconductors. This AC supercurrent was soon observed experimentally by coupling it to external AC radiation, resulting in new constant voltage steps in the current-voltage (I-V) characteristic when the frequencies of the supercurrent and external radiation match [4, 5].

The proportionality constant between the supercurrent frequency and the applied DC voltage is simply $2e/h$, depending only on the elementary charge e and Planck's constant h. This exact conversion between frequency and voltage has a profound impact in precision metrology, with the Josephson effect providing the internationally recognised definition of the volt [6]. The Josephson voltage standard defines one volt as the voltage that produces a Josephson supercurrent of frequency $2e/h = 483597.84841698...$GHz, with Hertz being defined by the caesium frequency standard.

Recently the Josephson effect has been extended, both theoretically and experimentally, to the case in which the weak link itself acts as a mechanical resonator in attempts to excite, cool and quantum mechanically 'squeeze' vibrational states [7–20]. Experimental signatures of the excitation of mechanical resonances in vibrating weak links have been reported in atomic scale oscillators produced in break junctions [16], in torsional resonators [18] and in suspended nanowires [20]. These early observations testify the potential of current experimental setups to fully

explore novel electromechanical effects in the context of superconductivity, but these are rather isolated, sample specific, measurements without a systematic exploration.

In contrast to these very few observations in superconducting setups, the interplay between electronic currents and vibrations has been explored extensively in the context of quantum transport through non-superconducting nanoelectromechanical systems (NEMS). The most striking manifestations of the excitation of mechanical vibrations by the electronic currents through the NEMS are the appearance of vibrational sidebands to the Coulomb-blockade peaks in the I-V characteristic, accompanied by a dramatic suppression of current at low bias (Franck-Condon blockade) when the electromechanical coupling is strong enough [21–24]. The analogous effects associated with the strong coupling regime in suspended Josephson junctions have never been explored so far. Moreover, the theoretical analysis of the I-V characteristic of suspended Josephson junctions has so far been limited to the voltage bias case [11–13, 15]. While this is a convenient theoretical approach, it has serious limitations in addressing the response of experimental devices due to a major constraint in the operation of Josephson junctions: their small impedance in comparison to that of the external circuit makes them invariably operate in the current bias regime even if one attempts to maintain a fixed voltage bias across them [25].

Throughout this thesis, the electromechanical coupling in superconducting devices will be explored extensively and, by means of numerical as well as analytical investigations, it will be demonstrated that existing experimental setups can be used to induce and detect high-frequency mechanical oscillations in suspended weak links using purely DC current bias conditions.

The structure of the thesis is as follows. In chapters 2 and 3, we will briefly discuss the background theory of superconductivity and of the Josephson effect. Then, in chapter 4, by exploiting a setup that allows one to tune the coupling strength between electronic and mechanical degrees of freedom, the Josephson effect will be explored in regimes that have not been studied before, revealing several new features in the junction's DC I-V characteristic. These features include mechanically-induced Shapiro plateaus, a variety of new hysteretic behaviours, abrupt energy-induced transitions to a zero voltage state and fractal-like structures. The predicted large current range of the Shapiro plateau in particular should result in the relatively simple detection of vibrational effects and the possibility of new sensing and metrology applications. This work has important consequences on the experimental research on NEMS, as high frequency mechanical oscillations may be conveniently activated and detected in a resonator without the need for any AC equipment. Direct experimental measurements of the systems DC I-V curve suffice to unveil all the fundamental

properties of the resonator, including its resonance frequency and quality factor.

For many applications of the Josephson effect such as in magnetometers and qubits, rather than using a single junction, two junctions are connected in parallel forming a loop, producing a so-called superconducting quantum interference device (SQUID) [26, 27]. An external magnetic flux penetrating the loop can then be used to controllably alter the supercurrent flowing through the device. In chapter 5 we will analyze SQUIDs where both weak links are suspended and may be coupled to mechanical oscillations independently, forming a natural extension to the work of the previous chapters. In this way, we will show that ordinary SQUID magnetometers may be improved upon considerably. We will also unveil that one can choose which of the two arms to excite, or even whether they oscillate in a symmetric or antisymmetric mode, just by the application of the external flux.

In chapter 6 we explore the quantum nature of Josephson junctions, and in particular their ability to produce oscillations that are a direct analogue of Bloch oscillations in conventional electronic systems, with the DC current bias playing the role of the external electric field. We show that, in a specific low energy limit, these Bloch oscillations dominate with respect to the usual Josephson ones and may be coupled to mechanical oscillations in the weak link. This allows the generation of non-classical mechanical states that are intimately coupled with the quantum dynamics of the junction.

The experimental realization of our theoretical proposals in state-of-the-art devices is carefully discussed in each case. One paper has been published from the work presented in chapter 4, focusing on the mechanically induced retrappings [28], while another is in the process of being submitted that will focus on the mechanically induced hysteresis. Two further papers are in production that will discuss the mechanically induced effects in SQUIDS, and due to Bloch oscillations as discussed in chapters 5 and 6 respectively.

2 Superconductivity

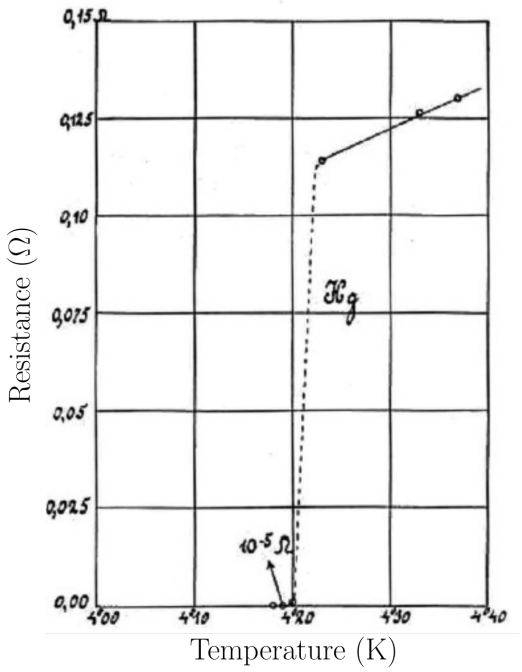

Figure 1: The original data obtained by Kamerlingh Onnes showing superconductivity [29]. The resistance of mercury drops to zero (within experimental error) abruptly as the temperature is decreased below $T_c \approx 4.2$K.

Superconductivity is a result of quantum coherence at macroscopic scales. In a superconductor, below a critical temperature a fraction of electrons become condensed into a 'superfluid' which extends over the whole system. This macroscopic condensate is responsible for the amazing properties of superconductors such as their zero DC electrical resistance and perfect diamagnetism [1].

Superconductivity was discovered in 1911 when Kamerlingh Onnes first observed that the electrical resistance of metals such as mercury, lead and tin decreased to zero abruptly when the temperature T is decreased below a critical value T_c, as shown in Fig. 1 [29]. The perfect diamagnetism of superconductors was discovered by Meissner and Ochsenfeld in 1933 [30]. They found that a magnetic field is not only excluded from a superconductor, but that a magnetic field in an originally normal metal sample is actively expelled when the temperature is lowered below T_c. This 'Meissner effect' only occurs up to some temperature dependent critical magnetic field $B_c(T)$, above which superconductivity is broken and the material enters a normal conducting state.

In 1935 the brothers Fritz and Heinz London proposed a phenomenological theory which produces both perfect conductivity and the Meissner effect [31]. They

considered a two-fluid model which separated the total electron density n into two contributions $n = n_{\mathrm{n}} + n_{\mathrm{s}}$ from 'normal' electrons n_{n} and 'superconducting' electrons n_{s}. The normal electron current density is given by the usual expression $\mathbf{J}_{\mathrm{n}} = \sigma_{\mathrm{n}}\mathbf{E}$ with a finite conductivity σ_{n}, while the superconducting current density $\mathbf{J}_{\mathrm{s}}$ is postulated to satisfy

$$\frac{\partial \mathbf{J}_{\mathrm{s}}}{\partial t} = \frac{n_{\mathrm{s}} e^2}{m}\mathbf{E}, \tag{1}$$

$$\nabla \times \mathbf{J}_{\mathrm{s}} = -\frac{n_{\mathrm{s}} e^2}{m}\mathbf{B}. \tag{2}$$

The first of these equations is simply Newton's second law applied to a set of particles with charge $-e$ and mass m, indicating that the superconducting electrons do not experience the scattering mechanisms that usually give rise to a finite normal conductivity. The second equation, when combined with Ampere's law produces

$$\nabla^2 \mathbf{B} = \frac{1}{\lambda_{\mathrm{L}}^2}\mathbf{B}, \tag{3}$$

which predicts that a magnetic field is attenuated inside a superconductor over the London penetration depth $\lambda_{\mathrm{L}} = \sqrt{m/\mu_0 n_{\mathrm{s}} e^2}$, where μ_0 is the vacuum permeability. This is the Meissner effect. If one instead eliminates B from Eq. (2), a similar equation is found for the supercurrent density

$$\nabla^2 \mathbf{J}_{\mathrm{s}} = \frac{1}{\lambda_{\mathrm{L}}^2}\mathbf{J}_{\mathrm{s}}, \tag{4}$$

showing that the supercurrent is confined to a thin layer at the boundary of the superconductor.

In 1950 Ginzburg and Landau extended the phenomenological London theory by allowing the superconducting electron density n_{s} to vary in space [32]. They introduced a complex 'macroscopic wave function' ψ which is related to the superconducting electron density n_{s} by

$$|\psi|^2 \propto n_{\mathrm{s}}, \tag{5}$$

and is to be determined at every point in space by minimizing the free energy of the system. By expanding the free energy in powers of $|\psi|^2$ they derived the following

equations for ψ and the supercurrent density $\mathbf{J}_\mathrm{s}$

$$\alpha\psi + \beta|\psi|^2\psi + \frac{1}{2m^*}(-i\hbar\nabla - q^*\mathbf{A})^2\psi = 0, \tag{6}$$

$$\mathbf{J}_\mathrm{s} = \frac{q^*\hbar}{2m^*i}\left(\psi^*\nabla\psi - \psi\nabla\psi^*\right) - \frac{q^{*2}}{m^*}|\psi|^2\mathbf{A}, \tag{7}$$

where m^* and q^* are the effective mass and charge of the superconducting charge carriers, while $\mathbf{A}$ is the magnetic vector potential and i is the imaginary unit. The parameters α and β are phenomenological expansion coefficients, but may be expressed in terms of physical parameters by ensuring agreement with the London model, these expressions will be derived in section 2.2 when we discuss the Ginzburg-Landau theory in more detail. The Ginzburg-Landau equations have a clear physical interpretation, Eq. (6) bears a similarity to the time independent Schrödinger equation except for the addition of a non-linear term, while Eq. (7) is identical in form to the usual probability current equation except that it describes a real electronic current. The Ginzburg-Landau theory is able to predict important features outside the scope of the London theory, such as non-linear effects of fields strong enough to change n_s and the spatial variation of n_s, but its first major accomplishment was its ability to treat regions where superconducting and normal domains overlap.

Despite the success of these macroscopic phenomenological theories, it was not until the 1950s, 40 years after Onnes' first discovery, that the basic microscopic origin of superconductivity was first being understood. In 1950 Reynolds [33] and Maxwell [34] independently discovered that the critical temperature and magnetic field vary with the isotopic mass of the material m_iso as $T_\mathrm{c}, B_\mathrm{c} \propto 1/\sqrt{m_\mathrm{iso}}$. This 'isotope effect' showed that the superfluid interacts with the ion cores of the metal and gave support to Fröhlich's point of view that an effective interaction between electrons arising from lattice vibrations was of primary importance in developing superconductivity [35].

A further clue came from the precise measurements of the specific heat capacity of superconductors C_s made by Corak *et al.* [36, 37]. They showed that in the superconducting state near $T = 0$ the specific heat is dominated by the scaling

$$C_\mathrm{s} \propto \exp(-1.75T_\mathrm{c}/T). \tag{8}$$

Such a scaling implies that the quasiparticle excitations have a minimum excitation energy of $\Delta(T = 0) \approx 1.75k_\mathrm{B}T_\mathrm{c}$. The existence of an energy gap between the ground state and the quasiparticle excitations was predicted earlier by Daunt and Mendelssohn [38], and subsequently confirmed by additional experiments in

electromagnetic absorption [39] and electron tunnelling [40].

Finally in 1956, Cooper showed that an arbitrarily weak attractive force between electrons is sufficient to cause them to combine into bound pairs that lower their total energy [41]. These 'Cooper pairs' were interpreted as the primary reason for the energy gap in superconductors and led to the development of a complete microscopic theory by Bardeen, Cooper and Schrieffer (BCS) in 1957 [42]. The BCS theory shows that below T_c, Cooper pairs condense into a macroscopic superfluid that extends over the whole superconductor. In terms of the two-fluid model, these Cooper pairs give rise to the superconducting electron density n_s while the quasiparticle excitations, having minimum energy Δ, act as the 'normal electrons' n_n. In this chapter we give a detailed description of the BCS theory, followed by a description of the phenomenological Ginzburg-Landau theory in preparation of its use in providing a simple derivation of the Josephson effect in the following chapter.

2.1 BCS Theory

2.1.1 One Pair Problem

Following Cooper we consider a pair of electrons interacting with each other above an inert Fermi sea. The electrons in the Fermi sea are non-interacting and serve only to forbid the interacting pair from entering states below the Fermi level $|\mathbf{k}| < k_F$ by the Pauli exclusion principle. To describe a state with zero current, we will consider a pair with zero net momentum. The pair wave function $\Psi(\mathbf{r})$ then depends only on the relative coordinate $\mathbf{r} = \mathbf{r}_1 - \mathbf{r}_2$ and we can expand it as a sum of plane waves with momentum $|\mathbf{k}| > k_F$ as follows

$$\Psi(\mathbf{r}) = \sum_{|\mathbf{k}|>k_F} g_{\mathbf{k}} e^{i\mathbf{k}\cdot\mathbf{r}} = \sum_{|\mathbf{k}|>k_F} g_{\mathbf{k}} e^{i\mathbf{k}\cdot\mathbf{r}_1} e^{-i\mathbf{k}\cdot\mathbf{r}_2}. \tag{9}$$

The total wave function is thus a superposition of pair states with $g_{\mathbf{k}}$ being the probability amplitude to find the pair in the state $(\mathbf{k}, -\mathbf{k})$. The Schrödinger equation is then

$$-\frac{\hbar^2}{2m}(\nabla_1^2 + \nabla_2^2)\Psi(\mathbf{r}) + V(\mathbf{r})\Psi(\mathbf{r}) = (E + 2E_F)\Psi(\mathbf{r}), \tag{10}$$

where $V(\mathbf{r})$ is the interaction potential and the energy E is measured from $2E_F$ with $E_F = \hbar^2 k_F^2/2m$ being the Fermi energy. Substituting Eq. (9) into (10) one obtains

$$(E + 2E_F - 2\varepsilon_{\mathbf{k}})g_{\mathbf{k}} = \sum_{|\mathbf{k}'|>k_F} V_{\mathbf{k},\mathbf{k}'} g_{\mathbf{k}'}, \tag{11}$$

which is simply the Schrödinger equation in Fourier space, where $\varepsilon_{\mathbf{k}} = \hbar^2\mathbf{k}^2/2m$ and

$$V_{\mathbf{k},\mathbf{k}'} = \int V(\mathbf{r})e^{-i(\mathbf{k}-\mathbf{k}')\cdot\mathbf{r}}\mathrm{d}\mathbf{r}. \tag{12}$$

Cooper chose a simple factorizable potential that captures the essential physics

$$V_{\mathbf{k},\mathbf{k}'} = \lambda w_{\mathbf{k}} w_{\mathbf{k}'} \tag{13}$$

where

$$w_{\mathbf{k}} = \begin{cases} 1, & \text{for } E_{\mathrm{F}} < \varepsilon_{\mathbf{k}} < E_{\mathrm{F}} + \hbar\omega_{\mathrm{D}} \\ 0, & \text{otherwise} \end{cases} \tag{14}$$

indicating that electrons only interact within an energy window $\hbar\omega_{\mathrm{D}}$ above the Fermi level, and interact with a constant strength λ. The Debye frequency ω_{D} is chosen since $\hbar\omega_{\mathrm{D}}$ is the characteristic energy scale of phonons, and it was already understood that the electron pairing was due to lattice vibrations. Inserting this potential into Eq. (11) we obtain

$$(E + 2E_{\mathrm{F}} - 2\varepsilon_{\mathbf{k}})g_{\mathbf{k}} = \lambda w_{\mathbf{k}} \sum_{|\mathbf{k}'|>k_{\mathrm{F}}} w_{\mathbf{k}'} g_{\mathbf{k}'} = \lambda w_{\mathbf{k}} G, \tag{15}$$

where G is a constant given by

$$G = \sum_{|\mathbf{k}'|>k_{\mathrm{F}}} w_{\mathbf{k}'} g_{\mathbf{k}'}. \tag{16}$$

The energy eigenvalues are calculated by inserting $g_{\mathbf{k}}$ from Eq. (15) into Eq. (16) to obtain the self-consistency equation

$$\frac{1}{\lambda} = \sum_{|\mathbf{k}|>k_{\mathrm{F}}} \frac{w_{\mathbf{k}}^2}{E - 2(\varepsilon_{\mathbf{k}} - E_{\mathrm{F}})} = \Theta(E). \tag{17}$$

The function $\Theta(E)$ is plotted in Fig. 2 for a one-dimensional system with N electrons in the Fermi sea. For $E > 0$, singularities occur whenever $E = 2(\varepsilon_{\mathbf{k}} - E_{\mathrm{F}})$ whereas for $E < 0$ the function is negative, approaching zero when $E \to -\infty$.

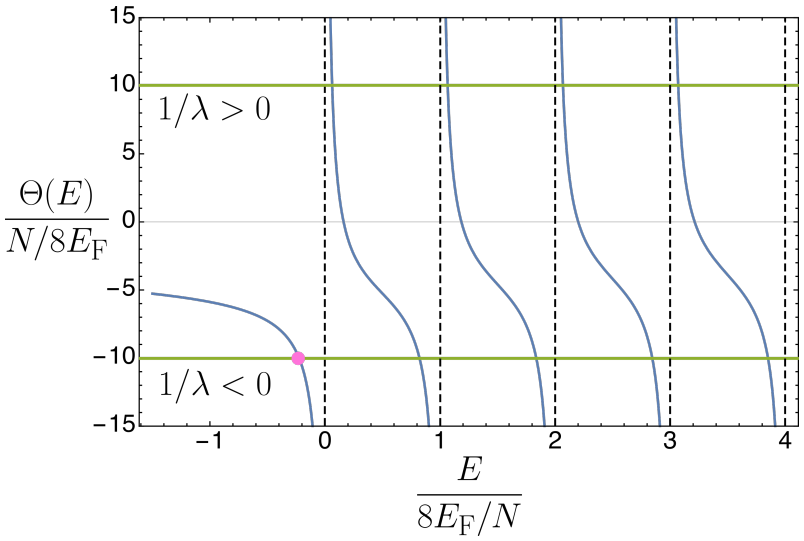

Figure 2: Plot of the function $\Theta(E)$ (blue lines) for a one-dimensional system with N electrons in the Fermi sea. Singularities occur whenever $E = 2(\varepsilon_{\mathbf{k}} - E_{\mathbf{F}})$[1]. Intersections with the line $1/\lambda$ give the solutions to the self-consistency equation (17) and thus the energy eigenvalues. Two example values of $1/\lambda$ are plotted (green lines). The repulsive interaction $1/\lambda > 0$ gives trivial solutions for unbound pairs with a positive energy only slightly renormalized with respect to the non-interacting case while the attractive interaction $1/\lambda < 0$ gives a unique bound state solution with $E < 0$ (pink dot).

The solutions to Eq. (17), and thus the energy eigenvalues E are found from the intersections of $\Theta(E)$ with the constant value $1/\lambda$. For a repulsive interaction $\lambda > 0$, the solutions are all positive and differ only a little from the non-interacting results at $2(\varepsilon_{\mathbf{k}} - E_{\mathrm{F}})$. An attractive interaction $\lambda < 0$ also allows these trivial positive energy solutions, but there is one unique solution at $E < 0$ corresponding to a bound state of the electron pair. Crucially, this 'Cooper pair' bound state exists no matter how weakly the electrons attract.

To actually carry out the summation in Eq. (17) and find the bound state energy E we transform the summation into an integral over energy via the density of states $\nu(\varepsilon)$

$$\frac{1}{\lambda} = \int_0^{\hbar\omega_{\mathrm{D}}} \nu(\varepsilon) \frac{1}{E - 2\varepsilon} \mathrm{d}\varepsilon, \tag{18}$$

where we have defined $\varepsilon = \varepsilon_{\mathbf{k}} - E_{\mathrm{F}}$. Since $\hbar\omega_{\mathrm{D}} \ll E_{\mathrm{F}}$ in ordinary metals, the density of states does not change appreciably in the thin shell from E_{F} to $E_{\mathrm{F}} + \hbar\omega_{\mathrm{D}}$ and we

[1]The singularities appear linearly spaced because we can expand $\varepsilon_k = \hbar^2(k_{\mathrm{F}} + \Delta k)^2/2m \approx E_{\mathrm{F}} + \hbar^2 k_{\mathrm{F}} \Delta k/m$. This is valid since $\Delta k/k_{\mathrm{F}} \ll 1$ by virtue of the fact that the only terms that enter the summation are in the thin shell $\hbar\omega_{\mathrm{D}} \ll E_{\mathrm{F}}$. For a one-dimensional system of length L we then have $\Delta k = n\pi/L$ where n is an integer, and we can write $\varepsilon_k - E_{\mathrm{F}} \approx 2\pi n E_{\mathrm{F}}/k_{\mathrm{F}} L = 4nE_{\mathrm{F}}/N$ where in the last equality we have used $k_{\mathrm{F}} = \pi N/2L$.

can use the approximation $\nu(\varepsilon) \approx \nu(0)$. The integral is then easily carried out

$$-\frac{1}{\nu(0)\lambda} = \frac{1}{2}\ln\left(1 - 2\frac{\hbar\omega_{\mathrm{D}}}{E}\right), \tag{19}$$

to find the energy

$$E = \frac{2\hbar\omega_{\mathrm{D}}}{1 - \exp(-2/\nu(0)\lambda)}. \tag{20}$$

In the case of an attractive interaction we have $\lambda = -|\lambda|$, and if this interaction is weak ($\nu(0)|\lambda| \ll 1$) the bound state energy reduces to

$$E \approx -2\hbar\omega_{\mathrm{D}} \exp(-2/\nu(0)|\lambda|). \tag{21}$$

Thus the Cooper pair bound state exists for arbitrarily small attractive interactions. We also see that the bound state energy is non-analytical in the dimensionless interaction strength $\nu(0)|\lambda|$ and thus does not permit any perturbative solutions. This is the reason why early theories by Fröhlich [35] and Bardeen [43] based on a perturbative treatment ran into mathematical difficulties and it took 46 years since Onnes' discovery to develop a correct microscopic theory.

As a consequence of our choice of the interaction $V_{\mathbf{k},\mathbf{k}'}$, the pair wave function Eq. (9) with $g_{\mathbf{k}}$ given by Eq. (15) is isotropic in real space, depending only on $|\mathbf{r}|$. A real space wave function that is symmetric means that the Cooper pair must be in a singlet state where the two electrons have opposite spins ($\mathbf{k}\uparrow, -\mathbf{k}\downarrow$). This so-called s-wave pairing is the one considered by BCS theory, and is dominant in the majority of superconductors. However, in materials with large anisotropy other pairings such as p-wave or d-wave may be important and are thought to be crucial in explaining unconventional superconductors with high T_{c}, although this remains a contentious issue [44].

2.1.2 BCS State

Motivated by the insight from Cooper's analysis, Bardeen, Cooper and Schrieffer (BCS) considered a many-body wave function where all electrons take part in the pairing process. Following their lead we use the formalism of second quantization and consider a ground state where each singlet pair ($\mathbf{k}\uparrow, -\mathbf{k}\downarrow$) has a probability amplitude $u_{\mathbf{k}}$ to be unoccupied and amplitude $v_{\mathbf{k}}$ to be occupied. For simplicity we take $u_{\mathbf{k}}$ and $v_{\mathbf{k}}$ to be real, and by probability conservation we must have $u_{\mathbf{k}}^2 + v_{\mathbf{k}}^2 = 1$.

The BCS state is then

$$|\text{BCS}\rangle = \prod_{\mathbf{k}} (u_{\mathbf{k}} + v_{\mathbf{k}} c^{\dagger}_{\mathbf{k}\uparrow} c^{\dagger}_{-\mathbf{k}\downarrow}) \, |0\rangle \, . \tag{22}$$

where $|0\rangle$ is the vacuum while $c^{\dagger}_{\mathbf{k}\sigma}$ and $c_{\mathbf{k}\sigma}$ are creation and annihilation operators for fermions with wavevector $\mathbf{k}$ and spin σ. These satisfy the usual anti-commutation relations

$$\{c_{\mathbf{k}\sigma}, c_{\mathbf{k}'\sigma'}\} = 0, \tag{23}$$

$$\{c^{\dagger}_{\mathbf{k}\sigma}, c^{\dagger}_{\mathbf{k}'\sigma'}\} = 0, \tag{24}$$

$$\{c_{\mathbf{k}\sigma}, c^{\dagger}_{\mathbf{k}'\sigma'}\} = \delta_{\mathbf{k}\mathbf{k}'}\delta_{\sigma\sigma'}, \tag{25}$$

where δ_{ij} is the Kronecker delta. Around the same time that BCS were working on their theory, Schafroth, Blatt and Butler (SBB) attempted a description of the superconducting state as a Bose-Einstein condensate of electron pairs [45]. This is a nice qualitative idea but is not completely correct as can be shown by considering the commutation relations obeyed by the pair operator $b_{\mathbf{k}} = c_{-\mathbf{k}\downarrow} c_{\mathbf{k}\uparrow}$

$$[b_{\mathbf{k}}, b_{\mathbf{k}'}] = 0, \tag{26}$$

$$[b^{\dagger}_{\mathbf{k}}, b^{\dagger}_{\mathbf{k}'}] = 0, \tag{27}$$

$$[b_{\mathbf{k}}, b^{\dagger}_{\mathbf{k}'}] = \delta_{\mathbf{k}\mathbf{k}'}(1 - n_{\mathbf{k}\uparrow} - n_{-\mathbf{k}\downarrow}), \tag{28}$$

where $n_{\mathbf{k}\sigma} = c^{\dagger}_{\mathbf{k}\sigma} c_{\mathbf{k}\sigma}$ is the number operator. These are not the commutation relations required by Bose-Einstein statistics, in fact the Pauli principle acting on individual electrons is evident from the fact that $(b^{\dagger}_{\mathbf{k}})^2 = 0$.

The only interaction processes which have a non-vanishing amplitude on the ground state $|\text{BCS}\rangle$ are those which preserve the pairing structure, scattering a pair from $(\mathbf{k}' \uparrow, -\mathbf{k}' \downarrow)$ into $(\mathbf{k} \uparrow, -\mathbf{k} \downarrow)$. Considering only these processes we have the effective BCS Hamiltonian

$$H_{\text{BCS}} = \sum_{\mathbf{k},\sigma} \varepsilon_{\mathbf{k}} n_{\mathbf{k},\sigma} + \sum_{\mathbf{k},\mathbf{k}'} V_{\mathbf{k},\mathbf{k}'} c^{\dagger}_{\mathbf{k}\uparrow} c^{\dagger}_{-\mathbf{k}\downarrow} c_{-\mathbf{k}'\downarrow} c_{\mathbf{k}'\uparrow}. \tag{29}$$

Following the approach of Bogoliubov [46] and Valatin [47] we perform a mean field analysis of H_{BCS} and diagonalize the resulting Hamiltonian to find the ground state

energy and the quasiparticle excitation spectrum. The mean field Hamiltonian is

$$\begin{aligned} H_{\text{BCS}}^{\text{M-F}} - \mu_{\text{cp}}\hat{N} = &\sum_{\mathbf{k}\sigma}(\varepsilon_{\mathbf{k}} - \mu_{\text{cp}})n_{\mathbf{k},\sigma} \\ &+ \sum_{\mathbf{k}\mathbf{k}'} V_{\mathbf{k}\mathbf{k}'}\left(\langle c^\dagger_{\mathbf{k}\uparrow}c_{\mathbf{k}\uparrow}\rangle c^\dagger_{-\mathbf{k}'\downarrow}c_{-\mathbf{k}'\downarrow} + \langle c^\dagger_{-\mathbf{k}'\downarrow}c_{-\mathbf{k}'\downarrow}\rangle c^\dagger_{\mathbf{k}\uparrow}c_{\mathbf{k}\uparrow}\right) \\ &+ \sum_{\mathbf{k}\mathbf{k}'} V_{\mathbf{k}\mathbf{k}'}\left(\langle c^\dagger_{\mathbf{k}\uparrow}c^\dagger_{-\mathbf{k}\downarrow}\rangle c_{-\mathbf{k}'\downarrow}c_{\mathbf{k}'\uparrow} + \langle c_{-\mathbf{k}'\downarrow}c_{\mathbf{k}'\uparrow}\rangle c^\dagger_{\mathbf{k}\uparrow}c^\dagger_{-\mathbf{k}\downarrow}\right), \end{aligned} \tag{30}$$

where $\langle \ldots \rangle$ are expectation values taken on $|\text{BCS}\rangle$, $\hat{N} = \sum_{\mathbf{k}\sigma} n_{\mathbf{k},\sigma}$ is the total particle number operator and we have introduced a chemical potential μ_{cp}. Using Eq. (22) the 'normal averages' in the second line are found to be

$$\langle c^\dagger_{\mathbf{k}\sigma}c_{\mathbf{k}\sigma}\rangle = v^2_{\mathbf{k}}, \tag{31}$$

and contrary to the non-interacting ground state, the BCS state allows non-zero 'anomalous averages'

$$\langle c_{-\mathbf{k}\downarrow}c_{\mathbf{k}\uparrow}\rangle = \langle c^\dagger_{\mathbf{k}\uparrow}c^\dagger_{-\mathbf{k}\downarrow}\rangle = u_{\mathbf{k}}v_{\mathbf{k}}. \tag{32}$$

The mean field Hamiltonian then becomes

$$H_{\text{BCS}}^{\text{M-F}} - \mu_{\text{cp}}\hat{N} = \sum_{\mathbf{k}\sigma}\tilde{\varepsilon}_{\mathbf{k}}n_{\mathbf{k}\sigma} - \sum_{\mathbf{k}}\left(\Delta_{\mathbf{k}}c^\dagger_{\mathbf{k}\uparrow}c^\dagger_{-\mathbf{k}\downarrow} + \Delta^*_{\mathbf{k}}c_{-\mathbf{k}\downarrow}c_{\mathbf{k}\uparrow}\right), \tag{33}$$

where we have introduced

$$\tilde{\varepsilon}_{\mathbf{k}} = \varepsilon_{\mathbf{k}} - \mu_{\text{cp}} + \sum_{\mathbf{k}'} v^2_{\mathbf{k}'}V_{\mathbf{k},\mathbf{k}'}, \tag{34}$$

and

$$\Delta_{\mathbf{k}} = -\sum_{\mathbf{k}'} V_{\mathbf{k},\mathbf{k}'}\langle c_{-\mathbf{k}'\downarrow}c_{\mathbf{k}'\uparrow}\rangle. \tag{35}$$

Thus we see that the normal average terms simply renormalize the single particle energies while all the interesting behaviour will result from the anomalous terms. Our task is then to diagonalize this mean field Hamiltonian, i.e. to put it in the form

$$H_{\text{BCS}}^{\text{M-F}} - \mu_{\text{cp}}\hat{N} = E_{\text{GS}} + \sum_{\mathbf{k}\sigma} E_{\mathbf{k}}\gamma^\dagger_{\mathbf{k}\sigma}\gamma_{\mathbf{k}\sigma}, \tag{36}$$

where E_{GS} is the ground state energy and $\gamma_{\mathbf{k}\sigma}$ is a new quasiparticle operator describing particles with an energy spectrum $E_{\mathbf{k}}$. It is important to realize that adding an electron to $|\text{BCS}\rangle$ in the state $\mathbf{k}\uparrow$ is equivalent to removing an electron from the state $-\mathbf{k}\downarrow$ except that the total number of pairs differs by unity. Based on this

idea, Bogoliubov and Valatin independently introduced the following operators

$$\gamma_{\mathbf{k}\uparrow} = u_{\mathbf{k}} c_{\mathbf{k}\uparrow} - v_{\mathbf{k}} c^{\dagger}_{-\mathbf{k}\downarrow}, \tag{37}$$

$$\gamma_{-\mathbf{k}\downarrow} = u_{\mathbf{k}} c_{-\mathbf{k}\downarrow} + v_{\mathbf{k}} c^{\dagger}_{\mathbf{k}\uparrow}. \tag{38}$$

One can readily check that as long as the condition $u_{\mathbf{k}}^2 + v_{\mathbf{k}}^2 = 1$ is preserved, these operators obey the anticommutation relations

$$\{\gamma_{\mathbf{k}\sigma}, \gamma_{\mathbf{k}'\sigma'}\} = 0, \tag{39}$$

$$\{\gamma^{\dagger}_{\mathbf{k}\sigma}, \gamma^{\dagger}_{\mathbf{k}'\sigma'}\} = 0, \tag{40}$$

$$\{\gamma_{\mathbf{k}\sigma}, \gamma^{\dagger}_{\mathbf{k}'\sigma'}\} = \delta_{\mathbf{k}\mathbf{k}'}\delta_{\sigma\sigma'}, \tag{41}$$

and thus describe fermions. We can now express the Hamiltonian in terms of these operators and then diagonalize the system[2]. The terms proportional to $\gamma\gamma$ and $\gamma^{\dagger}\gamma^{\dagger}$ can be forced to vanish by imposing the following condition on $u_{\mathbf{k}}$ and $v_{\mathbf{k}}$

$$u_{\mathbf{k}}^2 - v_{\mathbf{k}}^2 = \frac{2\tilde{\varepsilon}_{\mathbf{k}}}{\Delta_{\mathbf{k}}} u_{\mathbf{k}} v_{\mathbf{k}}. \tag{42}$$

Together with $u_{\mathbf{k}}^2 + v_{\mathbf{k}}^2 = 1$ this completely determines $u_{\mathbf{k}}$ and $v_{\mathbf{k}}$. The latter condition can be imposed by writing

$$u_{\mathbf{k}}^2 = \frac{1}{2}\left(1 + \frac{\tilde{\varepsilon}_{\mathbf{k}}}{E_{\mathbf{k}}}\right), \tag{43}$$

$$v_{\mathbf{k}}^2 = \frac{1}{2}\left(1 - \frac{\tilde{\varepsilon}_{\mathbf{k}}}{E_{\mathbf{k}}}\right), \tag{44}$$

and $E_{\mathbf{k}}$ is then determined by Eq. (42), yielding

$$E_{\mathbf{k}} = \sqrt{\tilde{\varepsilon}_{\mathbf{k}}^2 + \Delta_{\mathbf{k}}^2}. \tag{45}$$

With this choice of parameters, our Hamiltonian is diagonalized in the form Eq. (36) and the operators $\gamma^{\dagger}_{\mathbf{k}\sigma}/\gamma_{\mathbf{k}\sigma}$ create/annihilate quasiparticles with energy $E_{\mathbf{k}}$. The ground state energy measured relative to $\mu_{\mathrm{cp}}\hat{N}$ is given by

$$E_{\mathrm{GS}} = -\sum_{\mathbf{k}} \frac{\Delta_{\mathbf{k}}^2}{E_{\mathbf{k}} + \tilde{\varepsilon}_{\mathbf{k}}}. \tag{46}$$

Thus we see from Eq. (45) that a finite $\Delta_{\mathbf{k}}$ can be interpreted as a gap in the quasi-

[2]This is now a common-place treatment of many-body systems, known as a Bogoliubov or Bogoliubov-Valatin transformation, although it was first developed in this BCS context.

particle energy spectrum, and from Eq. (46) that the existence of this energy gap causes the total energy of the ground state to be reduced below the non-interacting value $E_{\mathrm{GS}} = 0$. The last thing to do is solve for $\Delta_{\mathbf{k}}$ from the definition Eq. (35). One obtains

$$\Delta_{\mathbf{k}} = -\sum_{\mathbf{k}'} V_{\mathbf{k},\mathbf{k}'} \frac{\Delta_{\mathbf{k}'}}{2E_{\mathbf{k}'}} \left(1 - \langle \gamma^{\dagger}_{\mathbf{k}'\uparrow}\gamma_{\mathbf{k}'\uparrow}\rangle - \langle \gamma^{\dagger}_{\mathbf{k}'\downarrow}\gamma_{\mathbf{k}'\downarrow}\rangle\right), \tag{47}$$

the operator $\gamma^{\dagger}_{\mathbf{k}\sigma}\gamma_{\mathbf{k}\sigma}$ is just the number operator for the fermionic quasiparticle, and as such its expectation value in thermal equilibrium is given by the Fermi-Dirac distribution

$$\langle \gamma^{\dagger}_{\mathbf{k}\sigma}\gamma_{\mathbf{k}\sigma}\rangle = \frac{1}{e^{E_{\mathbf{k}}/k_{\mathrm{B}}T} + 1}. \tag{48}$$

Eq. (47) then becomes

$$\Delta_{\mathbf{k}} = -\sum_{\mathbf{k}'} V_{\mathbf{k},\mathbf{k}'} \frac{\Delta_{\mathbf{k}'}}{2E_{\mathbf{k}'}} \tanh\left(\frac{E_{\mathbf{k}'}}{2k_{\mathrm{B}}T}\right). \tag{49}$$

This is the BCS gap equation which determines the energy gap when the form of interaction is specified. Using the simplified attractive interaction

$$V_{\mathbf{k},\mathbf{k}'} = \begin{cases} -|\lambda|, & \text{for } |\tilde{\varepsilon}_{\mathbf{k}}| < \hbar\omega_{\mathrm{D}} \\ 0, & \text{otherwise} \end{cases} \tag{50}$$

we see that the right hand side of Eq. (49) no longer depends on $\mathbf{k}$ and thus $\Delta_k \to \Delta$. We can solve the equation by transforming the summation into an integral over the density of states $\nu(\tilde{\varepsilon})$ and again making the approximations $\nu(\tilde{\varepsilon}) \approx \nu(0)$ since we operate only in a thin shell around the Fermi energy. We obtain

$$\frac{1}{\nu(0)|\lambda|} = \int_{-\hbar\omega_{\mathrm{D}}}^{\hbar\omega_{\mathrm{D}}} \frac{\tanh\left(\sqrt{\tilde{\varepsilon}^2 + \Delta^2}/2k_{\mathrm{B}}T\right)}{2\sqrt{\tilde{\varepsilon}^2 + \Delta^2}} \mathrm{d}\tilde{\varepsilon}, \tag{51}$$

which is easily solved in the $T = 0$ limit by performing the change of variable $\tilde{\varepsilon} = \Delta \sinh(x)$, yielding

$$\Delta(0) = \frac{\hbar\omega_{\mathrm{D}}}{\sinh\left(\frac{1}{\nu(0)|\lambda|}\right)}. \tag{52}$$

In the weak coupling limit $\nu(0)|\lambda| \ll 1$ this reduces to

$$\Delta(0) \approx 2\hbar\omega_{\mathrm{D}} \exp(-1/\nu(0)|\lambda|) \tag{53}$$

which is very similar to Eq. (21) originally obtained by Cooper.

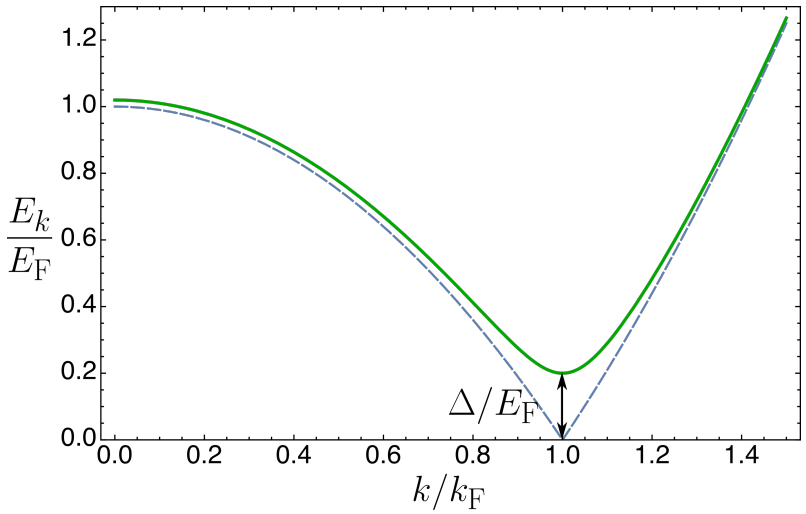

Figure 3: The quasiparticle energy spectrum $E_{\mathbf{k}}$ from Eq. (45) sketched for $\Delta/E_F = 0.2$ (green line), compared with the non-interacting case (dashed blue line). In the superconducting state an energy gap of size Δ opens at the Fermi energy.

With Δ determined, the quasiparticle energy spectrum and ground state energies are fully determined from Eqs. (45) and (46). The energy spectrum $E(k)$ is plotted in Fig. 3, one sees that it differs from the non-interacting case by the small energy gap Δ that opens at the Fermi level. Thus there is always a finite energy to pay in order to create excitations, explaining the observed gap in absorption and tunneling experiments. Most importantly, the superfluidity is explained as there is now a critical phase velocity v_c and thus electronic current density $J_c = -n_s e v_c$ below which there is no dissipation. This critical current density is given by[3]

$$J_c = -n_s e \min\left(\frac{E_{\mathbf{k}}}{\hbar \mathbf{k}}\right) = -n_s e \frac{\Delta}{\hbar k_{\mathbf{F}}}. \tag{54}$$

2.1.3 Critical Temperature

Eq. (51) gives the full temperature dependence of $\Delta(T)$ and allows one to determine the critical temperature T_c above which $\Delta(T)$ becomes zero and superconductivity is destroyed. Setting $T = T_c$ and $\Delta = 0$ and performing the integral yields

$$k_B T_c \approx 1.13 \hbar \omega_D \exp(-1/\nu(0)|\lambda|), \tag{55}$$

which when combined with Eq. (53) produces the very useful expression

$$\frac{\Delta(0)}{k_B T_c} \approx 1.764, \tag{56}$$

[3]Note that the effects of the pairing on $n_s \to n_s/2$ and $e \to 2e$ cancel eachother.

which is well confirmed experimentally. The full temperature dependence of $\Delta(T)$ must be calculated numerically from Eq. (51) but close to T_c it can be expressed conveniently in terms of T_c as

$$\frac{\Delta(T)}{\Delta(0)} \approx 1.74 \left(1 - \frac{T}{T_c}\right)^{1/2}. \tag{57}$$

The full temperature dependence and this approximation near T_c are both plotted in Fig. 4.

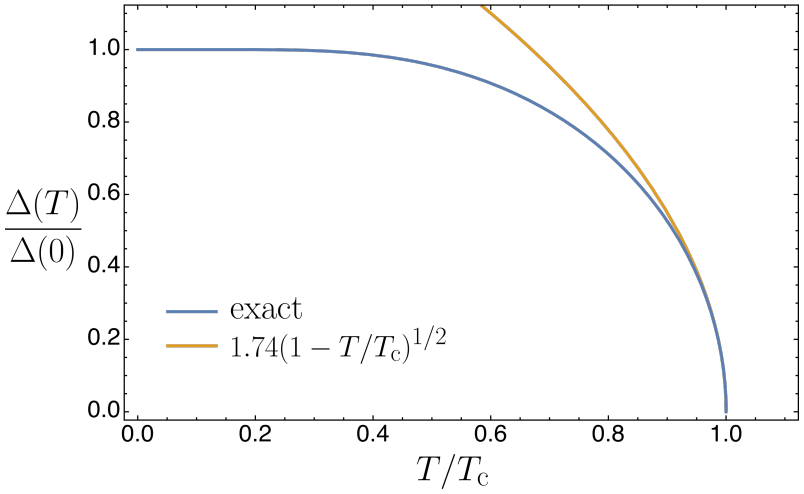

Figure 4: Temperature dependence of the superconducting energy gap $\Delta(T)$. The exact dependence from numerically solving Eq. (51) is plotted in blue, while the analytical solution Eq. (57) valid near T_c is plotted in orange.

2.2 Ginzburg-Landau Theory

The microscopic BCS theory works excellently in cases where the energy gap Δ is constant in space but there are many cases where there is spatial inhomogeneity such as at interfaces between normal metals and superconductors. In these cases the full microscopic theory becomes very difficult and we must use the more macroscopic Ginzburg-Landau (GL) theory. In any case, in 1959 Gor'kov [48] showed that BCS theory reduces to the GL theory at temperatures sufficiently close to T_c. We shall not follow the derivation of Gor'kov but instead postulate the theory phenomenologically as was originally done by Ginzburg and Landau.

They introduced a 'macroscopic wave function' $\psi(\mathbf{r})$ whose squared modulus is equal to the density of superconducting carriers n_s^*

$$|\psi|^2 = n_s^*. \tag{58}$$

Since the charge carriers are Cooper pairs, the density n_s^* is related to the density of 'superconducting electrons' n_s considered by the London brothers by $n_s^* = n_s/2$. Gor'kov showed that $|\psi|^2$ is proportional to the local value of the energy gap $\Delta(\mathbf{r})$ within the BCS theory, with a complex phase arising from the phase difference between the generally complex parameters $u_\mathbf{k}$, $v_\mathbf{k}$. This wave function is then to be determined at each point in space by minimizing the free energy of the system $\int f_s d^3\mathbf{r}$. They focused on the region $T \approx T_c$ and expanded the free energy density f_s as a function of ψ around the normal state value f_n. The phase of ψ is unobservable, so that the free energy should depend only on $|\psi|$. Furthermore, to keep the first derivative continuous at $\psi = 0$, only even powers of $|\psi|$ are included. We thus write the free energy density as

$$f_s = f_n + \alpha|\psi|^2 + \frac{\beta}{2}|\psi|^4 + \frac{1}{2m^*}|(-i\hbar\nabla - q^*\mathbf{A})\psi|^2 + \frac{\mathbf{B}^2}{2\mu_0}, \tag{59}$$

where α and β are phenomenological expansion coefficients to be given an exact form soon. This expression also includes the kinetic energy of the charge carriers with mass m^* and charge q^*, and the energy of the magnetic field $\mathbf{B}$. The kinetic energy term is modified to the usual gauge invariant form using the magnetic vector potential $\mathbf{A}$. For now we will leave q^* and m^* unspecified but the BCS theory gives their values as $q^* = -2e$ and $m^* = 2m$ as expected since the carriers of the supercurrent are Cooper pairs.

Deep in the interior of the superconductor, it is screened from any surface fields or currents and the free energy takes the simple form

$$f_s - f_n = \alpha|\psi|^2 + \frac{\beta}{2}|\psi|^4. \tag{60}$$

We can then determine $|\psi|^2$ by minimizing this quantity. Clearly to obtain a physical solution β must be positive or the minimum would occur for arbitrarily large values of $|\psi|^2$. Minimizing Eq. (60) then gives the following solutions

$$|\psi|^2 = 0, \tag{61}$$

$$|\psi|^2 = -\frac{\alpha}{\beta}. \tag{62}$$

If $\alpha > 0$ then the only real solution is $|\psi|^2 = 0$ which corresponds to the normal state with $n_s = 0$. On the other hand, if $\alpha < 0$, the $|\psi|^2 = 0$ minimum becomes unstable and a new stable solution develops at $|\psi|^2 = -\alpha/\beta$, which corresponds to a superconducting state. This situation is illustrated in Fig. 5. Clearly then, as α transitions from positive to negative there is a second order phase transition where

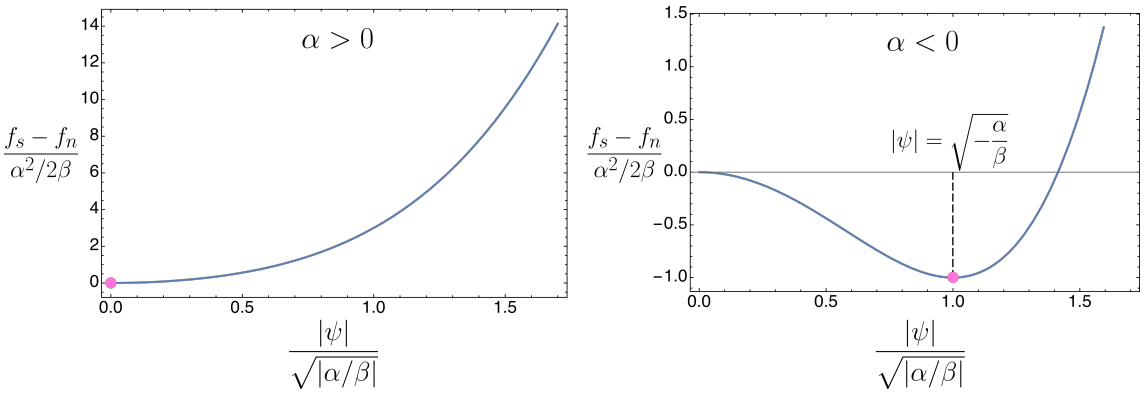

Figure 5: Sketch of $f_s - f_n$, the difference in free energy between the normal and superconducting states, as a function of the macroscopic wave function ψ for $\alpha > 0$ ($T > T_c$) and $\alpha < 0$ ($T < T_c$). The pink dots indicate the equilibirum solutions, which for $\alpha > 0$ is the normal state $|\psi|^2 = 0$ and for $\alpha < 0$ are the states $|\psi|^2 = -\alpha/\beta$ with non-zero density of superconducting carriers.

superconductivity emerges. From what we know about superconductors, we expect α to be a function of temperature, which decreases below zero as the temperature is lowered below T_c.

The free energy difference $f_s - f_n$ in the superconducting state is then obtained by inserting Eq. (62) into Eq. (60) obtaining

$$f_s - f_n = -\frac{\alpha^2}{2\beta} = -\frac{B_c^2}{2\mu_0}. \tag{63}$$

Here we have also used the definition of the critical magnetic field B_c that destroys superconductivity. We thus have in Eq. (63) a relation between α, β and B_c. From Eqs. (58) and (62) we also deduce $n_s^* = -\alpha/\beta$ so that we can express α and β in terms of the physical parameters B_c and n_s^* as

$$\alpha = -\frac{B_c^2}{\mu_0 n_s^*}, \tag{64}$$

$$\beta = \frac{B_c^2}{\mu_0 n_s^{*2}}. \tag{65}$$

It is more common to write these in terms of the London penetration depth $\lambda_L =$

$\sqrt{m^*/\mu_0 n_s^* q^{*2}}$ as follows[4].

$$\alpha = -\frac{B_c^2 \lambda_L^2 q^{*2}}{m^*}, \tag{66}$$

$$\beta = \frac{\mu_0 B_c^2 \lambda_L^4 q^{*4}}{m^{*2}}. \tag{67}$$

In the general case with fields, currents and gradients, $|\psi|^2$ must be calculated by minimizing the total free energy $\int f_s \mathrm{d}^3\mathbf{r}$ with f_s given by the full expression Eq. (59). Using standard variational techniques this leads to the GL equations[5]

$$\alpha\psi + \beta|\psi|^2\psi + \frac{1}{2m^*}(-i\hbar\nabla - q^*\mathbf{A})^2\psi = 0, \tag{68}$$

$$\mathbf{J}_s = \frac{q^*\hbar}{2m^* i}\left(\psi^*\nabla\psi - \psi\nabla\psi^*\right) - \frac{q^{*2}}{m^*}|\psi|^2\mathbf{A}. \tag{69}$$

The first of these is similar in form to the time-independent Schrödinger equation except for the addition of a non-linear term, while the second equation is identical in form to the usual probability current equation, except that it is multiplied by the charge q^* so that it describes a real electronic current. In fact by writing $\psi = |\psi|e^{i\theta}$, this equation takes the simple form

$$\mathbf{J}_s = \frac{q^*}{m^*}|\psi|^2(\hbar\nabla\theta - q^*\mathbf{A}) = |\psi|^2 q^*\mathbf{v}_s, \tag{70}$$

with the identification of the kinematic momentum $m^*\mathbf{v}_s = \hbar\nabla\theta - q^*\mathbf{A}$.

2.2.1 Coherence Length

Let us look at the differential equation (68) in the case where there are no fields $\mathbf{A} = 0$. In this case the differential equation has only real coefficients so that we can choose ψ to be real. We also non-dimensionalize the wave function as $\bar{\psi} = \psi/\psi_\infty$ where $\psi_\infty^2 = -\alpha/\beta > 0$. In one dimension we obtain

$$\frac{\hbar^2}{2m^*|\alpha|}\frac{\mathrm{d}^2\bar{\psi}}{\mathrm{d}x^2} + \bar{\psi} - \bar{\psi}^3 = 0. \tag{71}$$

It is then natural to define the characteristic length scale $\xi(T)$ as follows

$$\xi^2(T) = \frac{\hbar^2}{2m^*|\alpha|}. \tag{72}$$

[4]This definition of λ_L agrees with the one introduced by the London brothers if we take $q^* = -2e$, $m^* = 2m$ and $n_s^* = n_s/2$ since our charge carriers are Cooper pairs.

[5]These equations were already briefly introduced in Eqs. (6) and (7) but I reproduce them here for ease of reference.

So that Eq. (71) becomes

$$\xi^2(T)\frac{\mathrm{d}^2\bar{\psi}}{\mathrm{d}x^2} + \bar{\psi} - \bar{\psi}^3 = 0, \tag{73}$$

from which it is clear that $\xi(T)$, named the Ginzburg-Landau coherence length, gives the length scale over which variations of ψ occur. For example, at a superconductor-normal metal interface, ψ does not immediately drop to zero as we cross from the superconductor to the normal metal but instead continuously decreases to zero over the length scale $\xi(T)$. This implies that the normal metal adopts some superconducting behaviour when in close proximity to a superconductor. This proximity effect was first discussed in a pioneering paper by De Gennes [2]. We explore this further in the following section and see how this gives rise to the Josephson effect in superconducting weak links.

3 Josephson Effect

In 1962 Josephson carried out an analysis of tunneling processes in a system of two superconducting electrodes separated by an insulating barrier [3]. This led to his remarkable prediction that a zero voltage supercurrent may flow between the two electrodes due to the tunneling of Cooper pairs through the insulating barrier. This supercurrent I_s is strongly dependent on the phase difference $\phi = \theta_2 - \theta_1$, where θ_1 and θ_2 are the phases of the macroscopic wave functions in the two electrodes, through the simple relation

$$I_s = I_c \sin \phi, \tag{74}$$

where I_c is a sample dependent critical current. He also predicted that if a voltage bias V is maintained between the two electrodes, then the phase ϕ should evolve as

$$\frac{d\phi}{dt} = \frac{2e}{\hbar} V, \tag{75}$$

so that the supercurrent becomes AC with the frequency $2eV/\hbar$. This so-called Josephson effect was first confirmed experimentally the following year by Anderson and Rowell in the zero voltage case [49], while Shapiro soon after confirmed Eq. (75) in the finite voltage regime [4, 5].

While the Josephson effect was first predicted from a microscopic analysis of tunneling in superconductor-insulator-superconductor (SIS) junctions, it soon became clear that it was much more general, occurring whenever two superconductors are connected by a "weak link". This weak link may be a normal metal, forming superconductor-normal-superconductor (SNS) junctions, as a result of the proximity effect [51], or even a short, narrow constriction in an otherwise continuous superconductor, forming superconductor-constriction-superconductor (SCS) junctions, also known as Anderson-Dayem bridges [50]. The fundamental equations (74) and (75) remain valid in each of these cases. In what follows, we present a very simple derivation of the Josephson effect that follows directly from the Ginzburg-Landau theory, which is general enough to describe all these different weak link structures, rather than do a microscopic tunneling calculation as originally carried out by Josephson himself.

3.1 DC Josephson Effect

We consider two superconducting electrodes separated by a short link of length l and apply the Ginzburg-Landau theory. The one dimensional Ginzburg-Landau

equation is

$$\xi^2 \frac{\mathrm{d}^2\bar{\psi}}{\mathrm{d}x^2} + \bar{\psi} - \bar{\psi}^3 = 0, \tag{76}$$

where we recall that $\bar{\psi} = \psi/\psi_\infty$ is the order parameter in units of ψ_∞ which is the equilibrium value deep inside the superconductor. Assuming that the superconducting electrodes are in equilibrium and there is a phase difference ϕ between them, we must then solve Eq. (76) subject to the boundary conditions $\bar{\psi} = 1$ at $x = 0$ and $\bar{\psi} = \exp(i\phi)$ at $x = l$. The first term of this equation is larger than the other terms by a factor $(\xi/l)^2$ so that in the limit $l \ll \xi$ this equation simply reduces to Laplace's equation $\mathrm{d}^2\bar{\psi}/\mathrm{d}x^2 = 0$. Fixing our boundary conditions we obtain as a solution

$$\bar{\psi} = (1 - x/l) + (x/l)e^{i\phi}. \tag{77}$$

This has a very simple interpretation, with the first bracketed term giving the spread of the order parameter with phase zero from the first superconductor and the second term giving the spread of the order parameter from the second superconductor with phase ϕ.

Now that we know the value of the order parameter we can find the supercurrent density J_s flowing through the weak link by simply inserting this expression into the Ginzburg-Landau expression Eq. (69) which is expressed in terms of $\bar{\psi}$ as

$$J_\mathrm{s} = \frac{e\hbar\psi_\infty^2}{m^* i}\left(\bar{\psi}^* \frac{\mathrm{d}\bar{\psi}}{\mathrm{d}x} - \bar{\psi}\frac{\mathrm{d}\bar{\psi}^*}{\mathrm{d}x}\right) = \frac{2e\hbar\psi_\infty^2}{m^*}|\bar{\psi}|^2\nabla\theta, \tag{78}$$

where θ is the complex phase of $\bar{\psi} = |\bar{\psi}|\exp(i\theta)$ and we have used $q^* = -2e$ as the charge of a Cooper pair. Inserting our solution we obtain

$$J_\mathrm{s} = \frac{2e\hbar\psi_\infty^2}{lm^*}\sin\phi, \tag{79}$$

which upon multiplying by the cross-sectional area of the weak link S, yields the supercurrent I_s and thus the Josephson expression

$$I_\mathrm{s} = I_\mathrm{c}\sin\phi, \tag{80}$$

with the critical current

$$I_\mathrm{c} = \frac{2e\hbar\psi_\infty^2}{m^*}\frac{S}{l}. \tag{81}$$

The modulus square $|\bar{\psi}|^2$ and phase θ of the solution Eq. (77) are plotted in Fig. 6 for various phase differences ϕ. One can see from Eq. (78) that the supercurrent is a product of the two factors $|\bar{\psi}|^2$, proportional to the Cooper pair density in the

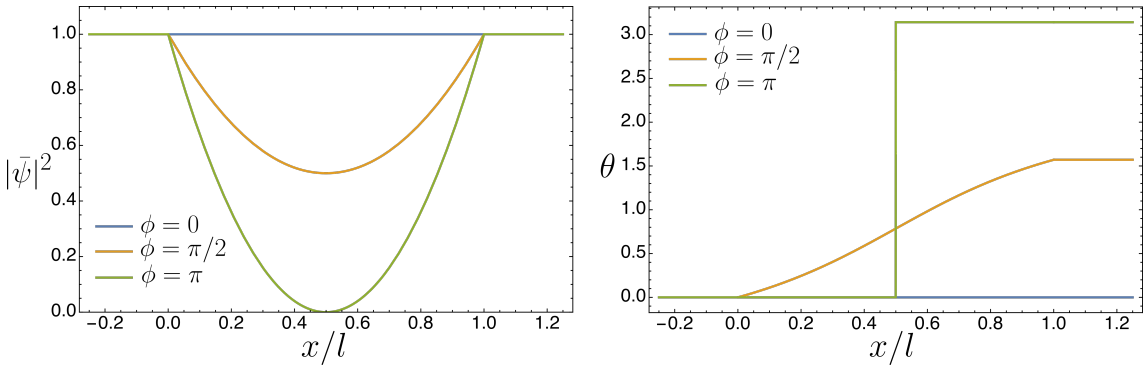

Figure 6: Plots of the modulus square $|\bar{\psi}|^2$ and phase θ of the solution Eq. (77) for the normalized order parameter $\bar{\psi}$, with several values of ϕ, the phase difference between the superconducting electrodes. In the two electrodes at $x \leq 0$ and $x \geq l$ we have $|\bar{\psi}|^2 = 1$ while in the weak link $0 < x < l$ the order parameter is reduced but generally non-zero, this is the proximity effect that gives rise to the Josephson effect. The phase θ evolves from $\theta = 0$ at $x \leq 0$ to $\theta = \phi$ at $x \geq l$.

weak link, and $\nabla\theta$, proportional to their effective velocity. From Fig. 6 we can then interpret the sinusoidal Josephson relation Eq. (80). When $\phi = 0$ there is a high number of carriers $|\bar{\psi}|^2$ but with zero velocity $\nabla\theta$ so there is no supercurrent. When $\phi = \pi$ there is a high velocity, but in the middle of the weak link where the carrier number is zero. However between these two extremes both $|\bar{\psi}|^2$ and $\nabla\theta$ are finite so that a supercurrent can flow, reaching a maximum at $\phi = \pi/2$.

The fact that I_c scales with the length and cross sectional area of the weak link exactly as S/l is an important result that is confirmed experimentally. In fact I_c scales in exactly the opposite way as the normal state resistance $R = \rho_n l/S$, where ρ_n is the normal state resistivity. Thus $I_c R = 2e\hbar\rho_n\psi_\infty^2/m^*$ is an invariant quantity that does not depend on the weak link dimensions, and is named the characteristic voltage. Ambegaokar and Baratoff [52] derived the following exact value for this $I_c R$ product for SIS tunnel junctions using BCS theory

$$I_c R = (\pi\Delta/2e)\tanh(\Delta/2k_B T), \tag{82}$$

which at $T = 0$ reduces to $I_c R = \pi\Delta(0)/2e$. This same formula applies for short constriction weak links except for a small pre-factor of order one [54, 55]. However for SNS junctions I_c decreases exponentially with the thickness of the normal layer l as $\exp(-l/\xi_n)$, where $\xi_n = \hbar v_F/2\pi k_B T$ is the normal metal coherence length. The characteristic voltage $I_c R$ can thus be lower than the ideal value given in Eq. (82) by this same exponential factor.

3.2 AC Josephson Effect

In order to derive the AC Josephson effect Eq. (75), we employ an alternate derivation due to Feynman [56]. Again we consider two superconductors, with a bias voltage V between them and separated by a thin weak link. We denote the effective wave functions of the two superconductors as ψ_L and ψ_R respectively and write down a two level system. Defining the zero point of potential to be between the two electrodes, a Cooper pair in ψ_L has an electrostatic energy $\langle\psi_L|\, H\, |\psi_L\rangle = eV$, while a Cooper pair in ψ_R has an electrostatic energy $\langle\psi_R|\, H\, |\psi_R\rangle = -eV$. Here H is the effective Hamiltonian of the system. We also introduce the probability amplitude for a Cooper pair to transition between the two states as $\langle\psi_R|\, H\, |\psi_L\rangle = \langle\psi_L|\, H\, |\psi_R\rangle^* = K$, which may be due to tunneling or direct conductivity. For more generality we can account for the effects of a magnetic field by including a vector potential $\mathbf{A}$, in this case the transition amplitude is modified from the zero field value K_0 by a correction $K = K_0 \exp(+i\frac{2e}{\hbar}\int \mathbf{A}\cdot \mathrm{d}\mathbf{l})$ in accordance with the usual laws of quantum mechanics [57], where the line integral is taken from the left electrode to the right one. The time dependent Schrödinger equation is then

$$i\hbar\frac{\mathrm{d}}{\mathrm{d}t}\begin{pmatrix}\psi_L\\ \psi_R\end{pmatrix} = \begin{pmatrix} eV & K_0\exp(-i\frac{2e}{\hbar}\int \mathbf{A}\cdot\mathrm{d}\mathbf{l})\\ K_0\exp(+i\frac{2e}{\hbar}\int \mathbf{A}\cdot\mathrm{d}\mathbf{l}) & -eV\end{pmatrix}\begin{pmatrix}\psi_L\\ \psi_R\end{pmatrix}. \tag{83}$$

Denoting the phases of the two superconductors as θ_L and θ_R, as well as their Cooper pair densities as n_L and n_R, we can make the substitutions $\psi_L = \sqrt{n_L}\exp(i\theta_L)$ and $\psi_R = \sqrt{n_R}\exp(i\theta_R)$. The following four equations are then obtained by matching the real and imaginary parts of the two complex equations in Eq. (83)

$$\frac{\mathrm{d}\theta_L}{\mathrm{d}t} = -\frac{eV}{\hbar} - \frac{K_0}{\hbar}\sqrt{\frac{n_R}{n_L}}\cos\left(\phi - \frac{2e}{\hbar}\int \mathbf{A}\cdot\mathrm{d}\mathbf{l}\right), \tag{84}$$

$$\frac{\mathrm{d}n_L}{\mathrm{d}t} = +\frac{2K_0}{\hbar}\sqrt{n_L n_R}\sin\left(\phi - \frac{2e}{\hbar}\int \mathbf{A}\cdot\mathrm{d}\mathbf{l}\right), \tag{85}$$

$$\frac{\mathrm{d}\theta_R}{\mathrm{d}t} = \frac{eV}{\hbar} - \frac{K_0}{\hbar}\sqrt{\frac{n_L}{n_R}}\cos\left(\phi - \frac{2e}{\hbar}\int \mathbf{A}\cdot\mathrm{d}\mathbf{l}\right), \tag{86}$$

$$\frac{\mathrm{d}n_R}{\mathrm{d}t} = -\frac{2K_0}{\hbar}\sqrt{n_L n_R}\sin\left(\phi - \frac{2e}{\hbar}\int \mathbf{A}\cdot\mathrm{d}\mathbf{l}\right), \tag{87}$$

where $\phi = \theta_R - \theta_L$. From these equations we can calculate the current flow, being proportional to $\mathrm{d}n_R/\mathrm{d}t = -\mathrm{d}n_L/\mathrm{d}t$. In reality the two electrodes are connected by a battery so that extra terms should be added to Eqs. (85) and (87) which keep n_R and n_L constant, but our expression for $\mathrm{d}n_R/\mathrm{d}t$ still gives the change due to the flow of current through the weak link. Assuming the superconductors are similar

we can set $n_R = n_L = n$ which produces

$$\frac{\mathrm{d}n_R}{\mathrm{d}t} = -\frac{2K_0}{\hbar} n \sin\left(\phi - \frac{2e}{\hbar}\int \mathbf{A}\cdot\mathrm{d}\mathbf{l}\right). \tag{88}$$

This is proportional to the total electronic supercurrent so that we obtain

$$I_\mathrm{s} = I_\mathrm{c} \sin\left(\phi - \frac{2e}{\hbar}\int \mathbf{A}\cdot\mathrm{d}\mathbf{l}\right), \tag{89}$$

where I_c is a critical current that is highly sample specific, depending on K_0, n and the weak link geometry. This is the Josephson relation Eq. (74) except that the argument of the sine is no longer the real phase difference $\phi = \theta_R - \theta_L$ but a *gauge-invariant phase difference*

$$\varphi = \phi - \frac{2e}{\hbar}\int \mathbf{A}\cdot\mathrm{d}\mathbf{l}. \tag{90}$$

This same modification can be obtained from the Ginzburg-Landau equations by keeping the full gauge invariant gradient expression $(-i\hbar\nabla - 2e\mathbf{A})$.

From Eqs. (84) and (86) we can now see how the phase difference evolves in time when a voltage bias is applied

$$\frac{\mathrm{d}\phi}{\mathrm{d}t} = \frac{\mathrm{d}}{\mathrm{d}t}(\theta_R - \theta_L) = \frac{2e}{\hbar}V, \tag{91}$$

which is the AC Josephson relation Eq. (75). We can write both the Josephson relations in terms of the gauge-invariant φ as

$$I_\mathrm{s} = I_\mathrm{c}\sin\varphi, \tag{92}$$

$$\frac{\mathrm{d}\varphi}{\mathrm{d}t} = \frac{2e}{\hbar}\left(V - \frac{\mathrm{d}}{\mathrm{d}t}\int \mathbf{A}\cdot\mathrm{d}\mathbf{l}\right). \tag{93}$$

In what follows we will make extensive use of these equations. In the absence of external electromagnetic fields $\mathbf{A} = 0$, $\varphi = \phi$ and we recover Eqs. (74) and (75), however when we begin applying external fields and coupling to mechanical oscillations the correction to Eq. (93) will play an important role.

3.3 RCSJ Model

The ratio between the frequency of the supercurrent and the voltage across the weak link as given by the Josephson relation is very large, $2e/\hbar \approx 3\,\mathrm{GHz}\,\mu\mathrm{V}^{-1}$, so that Josephson oscillations in real experiments typically have very large frequencies of

order GHz−THz. At such high frequencies the external circuitry, such as wires and contacts, has a very large impedance compared to the Josephson junction itself. If one then attempts to apply a voltage bias across the junction, most of the voltage drop occurs over the external circuit leaving the actual voltage across the junction hard to control. However, the current is very well defined so that the vast majority of Josephson junction experiments are done assuming a current bias rather than a voltage bias [25]. Under this assumption, Eq. (93) remains valid except that the voltage V is now a dynamic variable that develops naturally due to the current bias.

From Eq. (92) we see that the supercurrent has a maximum amplitude I_c, it is then clear that given a certain DC current bias I_{DC}, if $I_{DC} < I_c$ then all the applied current can be carried by a supercurrent, but if we have $I_{DC} > I_c$ there must arise additional current components. In 1968, the *resistively and capacitively shunted junction* (RCSJ) *model* for current biased Josephson junction dynamics was introduced separately by W. C. Stewart [58] and D. E. McCumber [59]. This model describes an equivalent circuit consisting of three parallel current channels: a pure supercurrent $I_c \sin\varphi$, a normal current V/R with effective resistance R and a displacement current $C\mathrm{d}V/\mathrm{d}t$ where C is the capacitance between the two electrodes. In contrast to the other current components, the displacement current is not carried by real electrons through the weak link but is a result of charge accumulation at the electrodes. Current conservation then yields the following equation

$$I_{DC} = I_c \sin\varphi + \frac{V}{R} + C\frac{\mathrm{d}V}{\mathrm{d}t}, \tag{94}$$

where I_{DC} is the DC bias current and V is the voltage across the junction which is generally time dependent. This voltage drop is related to the phase φ by Eq. (93), inserting this into Eq. (94) produces the following second order differential equation for φ.

$$I_{DC} = I_c \sin\varphi + \frac{\hbar}{2eR}\frac{\mathrm{d}\varphi}{\mathrm{d}t} + \frac{\hbar C}{2e}\frac{\mathrm{d}^2\varphi}{\mathrm{d}t^2}. \tag{95}$$

which is the main equation we will use to model Josephson junction dynamics. For bias currents $I_{DC} < I_c$, one can see by inspection that there is a solution with constant phase difference $\varphi = \arcsin(I_{DC}/I_c)$ where all the bias current is taken by the supercurrent channel and there is zero voltage drop across the junction. However, the supercurrent has a maximum amplitude I_c so that for bias currents $I_{DC} > I_c$, some of the current must be taken by the normal and displacement current channels, which involves developing a finite voltage. In this finite voltage state φ evolves with time due to Eq. (93) and the supercurrent becomes oscillatory.

We can simplify Eq. (95) by introducing a dimensionless current $i_{DC} = I_{DC}/I_c$

and time $\tau_c = \omega_c t$ where $\omega_c = 2eI_cR/\hbar$ is the characteristic frequency corresponding to a voltage I_cR

$$i_{DC} = \sin\varphi + \dot{\varphi} + \beta_c\ddot{\varphi}. \tag{96}$$

Here $\dot{f}$ refers to the derivative of f with respect to τ_c and $\beta_c = \omega_c RC$ is the Stewart-McCumber parameter that can be expressed as the ratio $\beta_c = |Z_R|/|Z_C|$, where $Z_R = R$ and $Z_C = -i/\omega_c C$ are the impedances of the resistive and capacitive channels at the frequency ω_c, respectively. In the finite voltage state the oscillatory supercurrent must be compensated by either the resistive or capacitive channels in order for the total current I_{DC} to be constant. In the regime $\beta_c \ll 1$ the supercurrent is mostly compensated by the resistive channel, while in the regime $\beta_c \gg 1$ it is mostly compensated by the capacitive channel. The voltage drop across the junction is now conveniently expressed in units of the characteristic voltage I_cR by $\dot{\varphi} = V/I_cR$.

3.3.1 Washboard Analogy

Before proceeding we consider an illuminating mechanical analogy. Our equation of motion Eq. (95) is identical in form to the one governing a particle of mass $(\hbar/2e)^2C$ moving along the φ axis in the 'tilted washboard' potential

$$U(\varphi) = -E_J\left(\cos\varphi + \frac{I_{DC}}{I_c}\varphi\right), \tag{97}$$

under the effect of a drag force $(\hbar/2e)^2(1/R)\mathrm{d}\varphi/\mathrm{d}t$, where $E_J = \hbar I_c/2e$ is the Josephson energy. The washboard potential $U(\varphi)$ is plotted in Fig. 7. In this analogy the bias current I_{DC} is proportional to the tilt of the washboard potential, while the voltage is proportional to the velocity of the particle $\mathrm{d}\varphi/\mathrm{d}t$ by Eq. (93). For bias currents $I_{DC} < I_c$ the washboard particle can be trapped in a local minimum $\varphi = \arcsin(I_{DC}/I_c)$ where it has zero average velocity corresponding to the superconducting (zero voltage) state. However, the particle oscillates in the potential minimum for a while before coming to rest. One can show by expanding $U(\varphi)$ around a minimum that these oscillations have a frequency

$$\omega_{osc} = \omega_p[1 - (I_{DC}/I_c)^2]^{1/4}, \tag{98}$$

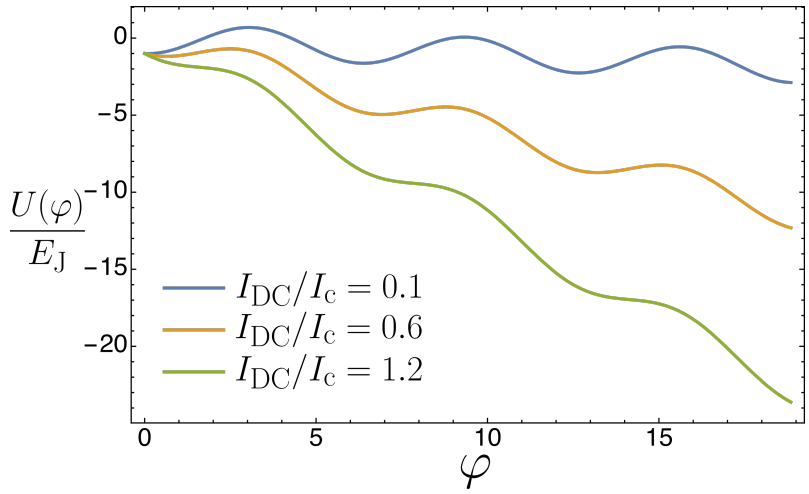

Figure 7: The tilted washboard potential $U(\varphi)$ which serves as a mechanical analog for the RCSJ model Eq. (95). The tilt of the washboard increases with increasing current I_{DC}. When $I_{DC} < I_c$ there are local minima in which a particle may become trapped, corresponding to a zero voltage state of the superconducting system. When $I_{DC} > I_c$ there are no local minima and the particle may freely roll down the washboard, corresponding to a finite voltage state.

where $\omega_p = (2eI_c/\hbar C)^{1/2}$ is the Josephson plasma frequency[6] and unless I_{DC} is very close to I_c we can approximate $\omega_{osc} \approx \omega_p$. This plasma frequency is an important quantity used frequently in the literature, especially in the context of thermal fluctuations where the particle never comes to a complete rest in the local minimum.

In contrast, for bias currents $I_{DC} > I_c$ there are no local minima and the particle rolls down the washboard with a finite velocity corresponding to the dissipative (finite voltage) state. In reference to this mechanical analogy, the zero and finite voltage states will often be referred to as the 'trapped' and 'running' states respectively.

The meaning of β_c becomes evident by considering that damping occurs over a time scale given by the mass of the particle divided by the drag coefficient, which amounts simply to the RC product of the junction. The Stewart-McCumber parameter β_c is then the ratio of this time scale over $1/\omega_c$, the time scale over which the particle progresses by a 'distance' $\Delta\varphi = 2\pi$, corresponding to the separation between two successive local minima of the washboard potential. For this reason the regimes $\beta_c \ll 1$ and $\beta_c \gg 1$ are referred to as the overdamped and underdamped regimes respectively.

[6]Named because these oscillations about the potential minima produce voltage, and thus charge, oscillations. Although this Josephson plasma frequency should not be confused with the usual bulk plasma frequency.

3.3.2 Overdamped Regime, $\beta_c \ll 1$

In the overdamped regime $\beta_c \ll 1$, the impedance of the capacitive channel dominates over the impedance of the resistive channel leading to a negligible displacement current. In this limit Eq. (95) reduces to the first order equation

$$I_{\mathrm{DC}} = I_{\mathrm{c}} \sin\varphi + \frac{\hbar}{2eR}\frac{\mathrm{d}\varphi}{\mathrm{d}t}. \tag{99}$$

In the running state, the AC supercurrent is thus compensated by a resistive current (and therefore voltage) which has an average value I_{DC} but is highly oscillatory, as shown by the numerical solution in Fig. 8(a). In the washboard analogy the highly oscillatory voltage is a result of the particle's velocity being modified considerably during one cycle $\Delta\varphi = 2\pi$ due to the large damping.

Fig. 8(b) shows the DC component of the voltage $\langle V \rangle$ as a function of DC bias current I_{DC} i.e. the junction's I-V characteristic. When $I_{\mathrm{DC}} < I_{\mathrm{c}}$ the trapped state $\langle V \rangle = 0$ is the only solution but when $I_{\mathrm{DC}} > I_{\mathrm{c}}$ the system enters a running state. One can solve for the time average voltage $\langle V \rangle$ in the running state by integrating Eq. (99) to determine the period of time T required for φ to advance by 2π and then using the relation $2e\langle V \rangle/\hbar = 2\pi/T$. The integral may be carried out either through the substitution $u = \tan(\varphi/2)$ or by employing Cauchy's residue theorem, and after a lengthy calculation one obtains

$$\langle V \rangle = R\sqrt{I_{\mathrm{DC}}^2 - I_{\mathrm{c}}^2}. \tag{100}$$

Which shows that $\langle V \rangle$ varies smoothly from $\langle V \rangle = 0$ for $I_{\mathrm{DC}} < I_{\mathrm{c}}$ to Ohmic behaviour $\langle V \rangle = IR$ for $I_{\mathrm{DC}} \gg I_{\mathrm{c}}$.

3.3.3 Underdamped Regime, $\beta_c \gg 1$

In the underdamped regime $\beta_{\mathrm{c}} \gg 1$, the impedance of the resistive channel dominates over the impedance of the capacitive channel so that the AC supercurrent is compensated by the displacement current. This results in a normal current / voltage which is predominantly DC with only a small AC component, as shown by the numerical solution in Fig. 9(a).

The corresponding I-V characteristic is plotted in Fig. 9(b). Similarly to the overdamped case, upon increasing I_{DC} from zero, the system remains in the trapped state until $I_{\mathrm{DC}} > I_{\mathrm{c}}$ at which point the system enters a running state. However, in contrast to the overdamped case, the voltage does not change continuously from zero but jumps to a finite value $\langle V \rangle \approx I_{\mathrm{c}}R$ corresponding to the terminal velocity of

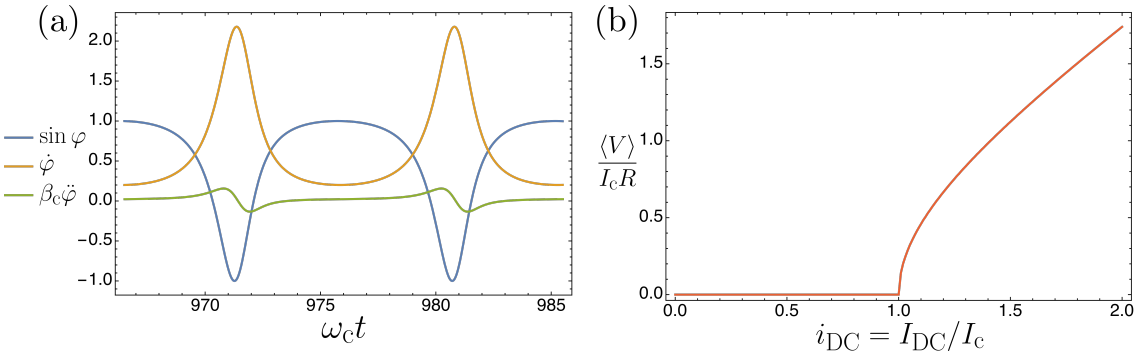

Figure 8: (a) Numerical solution of Eq. (95) with $i_{\mathrm{DC}} = 1.2$, $\beta_c = 0.1$ showing *overdamped* ($\beta_c \ll 1$) behaviour. The impedance of the capacitive channel dominates so that the AC supercurrent $\sin\varphi$ is compensated by a strongly AC normal current $\dot{\varphi}$, with a negligible displacement current $\beta_{\mathrm{c}}\ddot{\varphi}$. All currents are given in units of I_{c}. (b) Corresponding I-V characteristic calculated numerically, again with $\beta_{\mathrm{c}} = 0.1$. The analytical expression for this curve is given by Eq. (100).

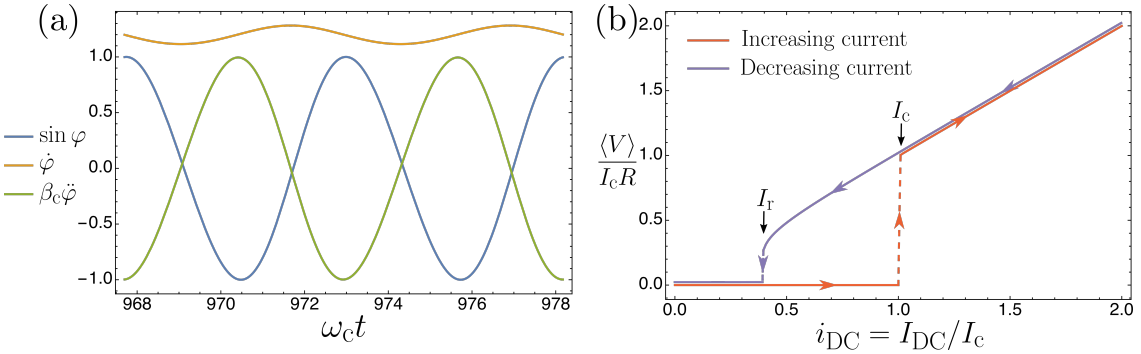

Figure 9: (a) Numerical solution of Eq. (95) with $i_{\mathrm{DC}} = 1.2$, $\beta_{\mathrm{c}} = 10$ showing *underdamped* ($\beta_{\mathrm{c}} \gg 1$) behaviour. The impedance of the resistive channel dominates so that the AC supercurrent $\sin\varphi$ is compensated by a strongly AC displacement current $\beta_{\mathrm{c}}\ddot{\varphi}$, leaving a normal current $\dot{\varphi}$ that is predominantly DC with a small AC component. All currents are given in units of I_{c}. (b) Corresponding I-V characteristic calculated numerically, again with $\beta_{\mathrm{c}} = 10$, showing hysteresis behaviour where the increasing and decreasing current paths access different states.

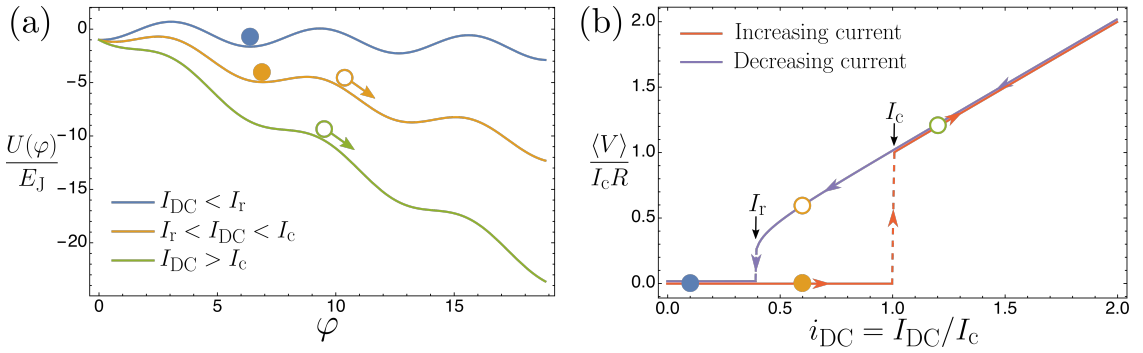

Figure 10: (a) The washboard potential $U(\varphi)$ plotted in three different current regimes, with filled and unfilled circles representing possible trapped and running states respectively. When $I_{DC} < I_r$ there exists only a trapped (zero voltage) state and when $I_{DC} > I_c$ there are no potential minima and there exists only a running (finite voltage) state. However if the junction is underdamped, $I_r \neq I_c$, and there is a regime $I_r < I_{DC} < I_c$ where there exists both a trapped and a running state. (b) The I-V characteristic of an underdamped junction with circles corresponding to the states labeled in (a).

the washboard particle. Even more striking is the presence of a hysteresis whereby if the current is reduced from above I_c the system remains in the running state until a lower 'retrapping current' I_r is reached. This hysteresis is most easily understood by referring again to the washboard analogy. The washboard potential $U(\varphi)$ is plotted again in Fig. 10(a) alongside the hysteretic I-V curve in Fig. 10(b). Similarly to the overdamped case we see that there are the usual trapped and running states for $I_{DC} < I_c$ and $I_{DC} > I_c$ respectively. However due to the low damping there is the new regime $I_r < I_{DC} < I_c$ in which there is both a trapped solution and a finite voltage running solution in which the particle has enough inertia to make it over the potential barriers without becoming trapped. The initial conditions decide which of these two solutions is chosen, leading to the observed hysteresis loop. To calculate the important current value I_r we must first discuss the energy stored in the system.

3.3.4 Energy

The total energy supplied by the external current I_{DC} over some time period is given by the integral $\int I_{DC} V \mathrm{d}t$. Using the RCSJ model Eq. (94) we can find how this energy is stored in the system. We obtain

$$\int I_{DC} V \mathrm{d}t = \int (I_c \sin\varphi) V \mathrm{d}t + \int \frac{V^2}{R} \mathrm{d}t + \int C \frac{\mathrm{d}V}{\mathrm{d}t} V \mathrm{d}t, \tag{101}$$

where the first and third terms on the right hand side give the energy that is stored by the supercurrent and displacement current, while the second term gives the energy

dissipated by the normal current. Carrying out the integrals using the Josephson relation Eq. (93) we obtain the total energy stored as

$$E = \frac{\hbar I_{\mathrm{DC}}}{2e}\varphi - \int \frac{V^2}{R}\mathrm{d}t = \frac{1}{2}CV^2 - E_{\mathrm{J}}\cos\varphi. \tag{102}$$

When the system reaches a steady state, the total energy supplied by the bias current over one cycle must be dissipated over this same period, leaving a stored energy that has a constant average value but that is generally time dependent. In the washboard model, the capacitive and supercurrent energies are interpreted as kinetic and potential energies respectively. Note that the term $-\hbar I_{\mathrm{DC}}\varphi/2e$ appearing in the washboard potential Eq. (97) should be interpreted as the energy supplied by a constant external force.

3.3.5 Retrapping Current

We can derive an expression for the retrapping current I_{r} in the underdamped case by using a simple energy argument. In terms of the washboard analogy, at the retrapping current, a particle infinitesimally close to rest $\dot{\varphi} = 0$ at a potential maximum $\varphi = -\pi$ will just reach the next potential maximum $\varphi = +\pi$ where it will again have zero velocity. Reducing the current any further will raise the potential barrier, forcing the particle to become trapped. At the potential maximum then $V = 0, \varphi = \pi$ and the energy from Eq. (102) is $E = E_{\mathrm{J}}$. If we now make the approximation that E does not vary much during one cycle, which is true in the underdamped limit, we can assume the total energy is constant at E_{J} and thus give the voltage in terms of φ from Eq. (102) as

$$V^2 = \frac{2E_{\mathrm{J}}}{C}(1 + \cos\varphi). \tag{103}$$

The retrapping energy is then calculated by ensuring that the total energy supplied as the particle goes from $\varphi = -\pi$ to $\varphi = +\pi$ is completely dissipated

$$\begin{aligned}
\int_0^T I_{\mathrm{r}} V \mathrm{d}t &= \int_0^T \frac{V^2}{R}\mathrm{d}t, \\
\frac{\hbar I_{\mathrm{r}}}{2e}\int_{-\pi}^{+\pi} \dot{\varphi}\frac{\mathrm{d}t}{\mathrm{d}\varphi}\mathrm{d}\varphi &= \int_{-\pi}^{+\pi} \frac{\hbar}{2eR} V \dot{\varphi}\frac{\mathrm{d}t}{\mathrm{d}\varphi}\mathrm{d}\varphi, \\
\frac{\pi\hbar I_{\mathrm{r}}}{e} &= \frac{\hbar}{2eR}\sqrt{\frac{2E_{\mathrm{J}}}{C}}\int_{-\pi}^{+\pi}\sqrt{1+\cos\varphi}\,\mathrm{d}\varphi, \\
I_{\mathrm{r}} &= \frac{4}{\pi R}\sqrt{\frac{E_{\mathrm{J}}}{C}},
\end{aligned}$$

where the integral has been evaluated using the double angle formula. Using the definition of E_J one may then show that the fraction $I_\mathrm{r}/I_\mathrm{c}$ depends only on β_c through the simple relation

$$I_\mathrm{r} = \frac{4}{\pi\sqrt{\beta_\mathrm{c}}} I_\mathrm{c}. \tag{104}$$

3.4 Finite Temperature Effects

So far we have not included any effects of thermal currents in our RCSJ model, but they can be included straightforwardly by adding a Johnson-Nyquist noise current term $\tilde{I}(t)$ to Eq. (95) as follows

$$I_\mathrm{DC} + \tilde{I}(t) = I_\mathrm{c} \sin\varphi + \frac{\hbar}{2eR}\frac{\mathrm{d}\varphi}{\mathrm{d}t} + \frac{\hbar C}{2e}\frac{\mathrm{d}^2\varphi}{\mathrm{d}t^2}. \tag{105}$$

This noise current should satisfy the usual correlation function

$$\langle \tilde{I}(t)\tilde{I}(t')\rangle = \frac{2k_\mathrm{B}T}{R}\delta(t-t'), \tag{106}$$

where $\delta(t-t')$ is the Dirac delta function. This equation assumes that the noise is a Gaussian uncorrelated process, meaning that at each point in time $\tilde{I}(t)$ takes on a random value given by a Gaussian distribution with zero mean and a finite variance σ^2_noise given by

$$\sigma^2_\mathrm{noise} = \frac{2k_\mathrm{B}T}{R\Delta t}, \tag{107}$$

where Δt is the time step over which the noise is sampled. We can write the correlation function in terms of dimensionless quantities by defining $\tilde{i}(t) = \tilde{I}(t)/I_\mathrm{c}$ and measuring time again in units $\tau_\mathrm{c} = \omega_\mathrm{c} t$. After using the transformation properties of the Dirac delta function we obtain

$$\langle \tilde{i}(\tau_\mathrm{c})\tilde{i}(\tau_\mathrm{c}')\rangle = 2\frac{T}{T_\mathrm{J}}\delta(\tau_\mathrm{c}-\tau_\mathrm{c}'), \tag{108}$$

where T_J is the temperature scale associated with the Josephson energy $E_\mathrm{J} = k_\mathrm{B}T_\mathrm{J} = \hbar I_\mathrm{c}/2e$. The corresponding variance is

$$\sigma^2_\mathrm{noise} = \frac{2}{\Delta\tau_\mathrm{c}}\frac{T}{T_\mathrm{J}}. \tag{109}$$

These equations imply that temperature fluctuation effects become important only when the thermal energy $k_\mathrm{B}T$ is comparable or greater than the Josephson energy E_J i.e. the height of the potential barriers in the washboard model. In insulating tunnel junctions temperature effects are usually only significant near T_c whereas in

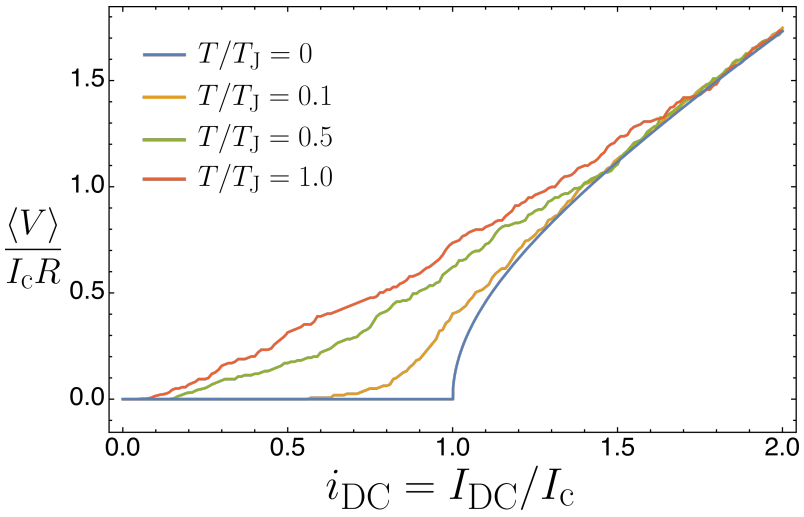

Figure 11: I-V curves of an *overdamped* junction ($\beta_c = 0.1$) at four different temperatures by numerically solving Eq. (105). At $T = 0$ (blue line) we have the usual analytical form Eq. (100), while at finite temperatures $T/T_J = 0.1, 0.5, 1.0$ (orange, green and red lines) a finite voltage develops even at $I_{DC} < I_c$ due to phase slip processes. At higher temperatures these processes are more common leading to higher voltages, and in the limit $T \gg T_J$ we recover an Ohmic curve $\langle V \rangle = I_{DC} R$.

metallic weak links temperature effects can be important at lower temperatures due to the much lower critical currents involved. A typical critical current of $I_c = 100\text{nA}$ corresponds to a Josephson temperature of $T_J = 2.38\text{K}$.

3.4.1 Thermal Effects in Overdamped Junctions

In overdamped junctions $\beta_c \ll 1$, the ideal I-V curve Eq. (100) is fundamentally modified by the presence of thermal fluctuations. These fluctuations allow a finite voltage even when $I < I_c$ due to so-called 'phase-slip' processes where the washboard particle can be kicked out of one potential into a lower one by the thermal current, causing a phase shift of $\Delta\varphi = 2\pi$. This same process can then occur many times, leading to a finite velocity of the washboard particle, and thus a finite voltage which is less than if the particle was continuously rolling down as happens when $I_{DC} > I_c$. Numerically produced I-V curves for an overdamped junction ($\beta_c = 0.1$) at finite temperatures are shown in Fig. 11 which show this finite voltage due to phase slip processes developing as the temperature T becomes comparable to the Josephson temperature T_J.

3.4.2 Thermal Effects in Underdamped Junctions

In underdamped junctions $\beta_c \gg 1$, the particle can also randomly receive a kick big enough to allow it to transition over a potential barrier. However in this case

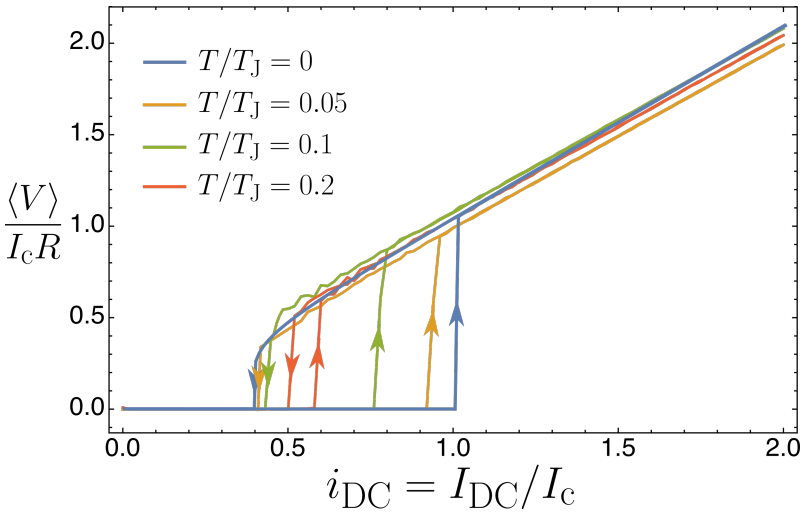

Figure 12: I-V curves of an *underdamped* junction ($\beta_c = 10$) at four different temperatures by numerically solving Eq. (105), showing both the increasing and decreasing current paths, distinguished by the arrow directions. At $T = 0$ (blue line) the switching and retrapping currents are I_c and I_r, while at finite temperatures $T/T_J = 0.05, 0.1, 0.2$ (orange, green and red lines) the switching current decreases while the retrapping current increases, leading to the eventual elimination of hysteresis in the limit $T \gg T_J$.

due to the low damping it becomes harder for the particle to become trapped again and carries on running in the finite voltage state. This leads to the effective critical current at which a finite voltage develops, sometimes called the switching current I_{sw}, being reduced below the ideal value I_c. This is a stochastic process, so that different values of the switching current are measured with each current sweep, but the mean value has been calculated by Fulton and Dunkleberger [61] to be

$$\langle I_{sw} \rangle = I_c\{1 - [(T/2T_J)\ln(\omega_p \delta t/2\pi)]^{2/3}\}, \tag{110}$$

where δt is the time taken to experimentally sweep the bias current. Assuming $\delta t \approx 1$sec, this can be up to 10 orders of magnitude larger than the time scale $1/\omega_p$ so that $\ln(\omega_p \delta t/2\pi) \sim 10$ and the reduction in I_c can become significant even when $T/T_J \approx 0.1$.

While a fluctuation can cause the particle to transition from a trapped state to a running state, the reverse process is also possible where a particle rolling down the washboard receives a random kick strong enough to lower its velocity causing it to retrap. This retrapping can occur above the ideal value I_r so that while the effective critical current is reduced by thermal fluctuations, the effective retrapping current is increased. The combined effect of both these processes leads to the suppression and eventual elimination of hysteresis in the I-V curve as the critical and retrapping

currents approach each other. Numerically produced I-V curve for an underdamped junction ($\beta_c = 10$) are shown in Fig. 12 showing this elimination of hysteresis as T increases.

3.5 AC Bias and Shapiro Steps

In 1963, a few months after the first experimental detection of the Josephson effect by Anderson and Rowell [49], Shapiro confirmed these findings and made an important discovery of his own [4]. He found that when a Josephson junction is irradiated with radiation of a frequency ω_1, a series of constant voltage steps arise in the I-V characteristic at voltages $\langle V \rangle = n\hbar\omega_1/2e$. On these 'Shapiro steps', the frequency of the Josephson supercurrent $2e\langle V \rangle/\hbar$ is thus locked to multiples of ω_1, and this historically provided the first indirect evidence of the AC Josephson effect.

A theoretical understanding of Shapiro steps can be obtained by treating the radiation as an ideal AC voltage source

$$V = V_{\mathrm{DC}} + V_{\mathrm{AC}} \cos(\omega_1 t). \tag{111}$$

Similar to the DC bias case, an AC *current* bias is a much more realistic assumption since the current of a small impedance device is fixed by the resistance of the external circuit [60]. However using the ideal voltage bias Eq. (111) gives some useful qualitative results. Integrating the AC Josephson relation Eq. (93) thus tells us how the phase φ evolves in time

$$\varphi(t) = \varphi_0 + \frac{2eV_{\mathrm{DC}}}{\hbar} t + \frac{2eV_{\mathrm{AC}}}{\hbar\omega_1} \sin(\omega_1 t), \tag{112}$$

and we can find the supercurrent I_s by

$$\begin{aligned} \frac{I_s}{I_c} &= \sin\varphi && (113)\\ &= \mathrm{Im}\left\{\exp(i\varphi)\right\} && (114)\\ &= \mathrm{Im}\left\{\exp\left(i\left(\varphi_0 + \frac{2eV_{\mathrm{DC}}}{\hbar}t\right)\right)\exp\left(i\frac{2eV_{\mathrm{AC}}}{\hbar\omega_1}\sin(\omega_1 t)\right)\right\}, && (115) \end{aligned}$$

where Im{} indicates the imaginary component of the enclosed expression. To proceed we must use the Jacobi-Anger expansion

$$\exp(iz\sin\theta) = \sum_{n=-\infty}^{+\infty} \mathcal{J}_n(z)\exp(in\theta), \tag{116}$$

where $\mathcal{J}_{\mathrm{n}}(z)$ are Bessel functions of the first kind, yielding

$$\frac{I_{\mathrm{s}}}{I_{\mathrm{c}}} = \mathrm{Im}\left\{\exp\left(i\left(\varphi_0 + \frac{2eV_{\mathrm{DC}}}{\hbar}t\right)\right)\sum_{n=-\infty}^{+\infty}\mathcal{J}_n\left(\frac{2eV_{\mathrm{AC}}}{\hbar\omega_1}\right)\exp(in\omega_1 t)\right\}, \tag{117}$$

$$= \mathrm{Im}\left\{\sum_{n=-\infty}^{+\infty}\mathcal{J}_n\left(\frac{2eV_{\mathrm{AC}}}{\hbar\omega_1}\right)\exp\left(i\left(\varphi_0 + \frac{2eV_{\mathrm{DC}}}{\hbar}t + n\omega_1 t\right)\right)\right\}, \tag{118}$$

$$= \sum_{n=-\infty}^{+\infty}\mathcal{J}_n\left(\frac{2eV_{\mathrm{AC}}}{\hbar\omega_1}\right)\sin\left(\varphi_0 + \frac{2eV_{\mathrm{DC}}}{\hbar}t + n\omega_1 t\right). \tag{119}$$

It is also convenient to make the transformation $n \to -n$ using the identity $\mathcal{J}_{-n}(z) = (-1)^n\mathcal{J}_n(z)$

$$\frac{I_{\mathrm{s}}}{I_{\mathrm{c}}} = \sum_{n=-\infty}^{+\infty}(-1)^n\mathcal{J}_n\left(\frac{2eV_{\mathrm{AC}}}{\hbar\omega_1}\right)\sin\left(\varphi_0 + \frac{2e}{\hbar}\left(V_{\mathrm{DC}} - \frac{n\hbar\omega_1}{2e}\right)t\right), \tag{120}$$

from which it is obvious that there is a DC component of the supercurrent at precisely the voltages $V_{\mathrm{DC}} = n\hbar\omega_1/2e$ observed by Shapiro.

In the experimentally relevant AC current bias case, this DC component of the supercurrent leads to the formation of the Shapiro plateaus in current appearing at these voltage steps. We can see this numerically by adding an additional AC current source $I_{\mathrm{AC}}\sin(\omega_1 t)$ to our RCSJ model Eq. (95)

$$I_{\mathrm{DC}} + I_{\mathrm{AC}}\sin(\omega_1 t) = I_{\mathrm{c}}\sin\varphi + \frac{\hbar}{2eR}\frac{\mathrm{d}\varphi}{\mathrm{d}t} + \frac{\hbar C}{2e}\frac{\mathrm{d}^2\varphi}{\mathrm{d}t^2}, \tag{121}$$

which upon non-dimensionalizing in the same way as Eq. (96) becomes

$$i_{\mathrm{DC}} + i_{\mathrm{AC}}\sin(\bar{\omega}_1\tau_{\mathrm{c}}) = \sin\varphi + \dot{\varphi} + \beta_c\ddot{\varphi}, \tag{122}$$

with $i_{\mathrm{AC}} = I_{\mathrm{AC}}/I_{\mathrm{c}}$ and $\bar{\omega}_1 = \omega_1/\omega_{\mathrm{c}}$. Solving this equation for various values of the DC component of the bias i_{DC} leads to the I-V characteristic plotted in Fig. (13). Multiple Shapiro plateaus are visible, with higher plateaus having generally smaller widths, providing an adequate theory to describe Shapiro's experimental observations.

A numerical analysis of the dependence of the Shapiro plateau widths on the AC bias strength was carried out by P. Russer [62]. The maximum supercurrent before entering the finite voltage state differs from I_{c} due to the influence of the AC current and may be conveniently considered as the width of an $n = 0$ Shapiro step. The dependence of this maximum current, as well as the widths of the $n = 1$ and $n = 2$

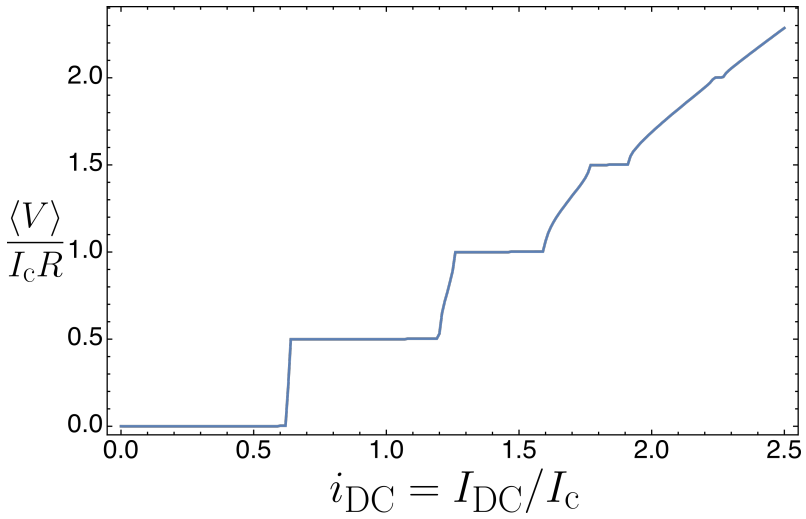

Figure 13: I-V curve of an AC current biased Josephson junction, produced by numerically solving Eq. (122) with $\bar{\omega}_1 = 0.5$, $i_{AC} = 0.8$ and $\beta_c = 0.1$. Shapiro plateaus are visible at voltages $\langle V \rangle / I_c R = n\bar{\omega}_1$. i.e. $\langle V \rangle = n\hbar\omega_1/2e$, with decreasing step sizes on higher plateaus.

steps, on the AC bias strength i_{AC} is shown in P. Russer's results in Fig. 14. The step widths oscillate as a function of i_{AC} in a qualitatively similar way to the Bessel function form Eq. (120) found in the voltage bias treatment, with higher steps and lower frequencies $\bar{\omega}_1$ having generally lower amplitudes.

In the next chapter we will discuss new effects that arise when the Josephson weak link is suspended and allowed to oscillate mechanically. In particular, we will see the emergence of Shapiro-like constant voltage plateaus in the junctions I-V characteristic where the supercurrent frequency becomes locked to the weak link's mechanical resonance frequency.

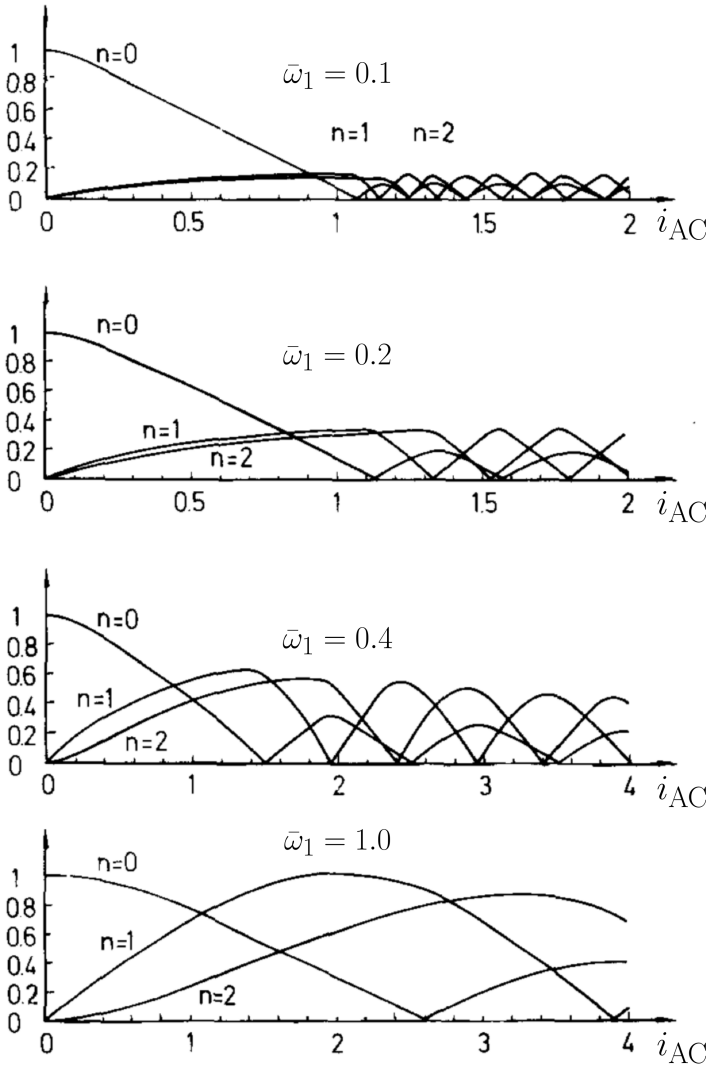

Figure 14: Dependence of the maximum supercurrent before entering the finite voltage state ($n = 0$) and the width of the first two Shapiro steps ($n = 1$) and ($n = 2$) (in units I_c) as a function of the AC bias current amplitude i_{AC}, adapted from the work of P. Russer [62]. Four different values of the driving frequency $\bar{\omega}_1$ were used and each show that the width of the steps oscillate in a qualitatively similar way to the Bessel function form Eq. (120) found in the voltage bias treatment.

4 Josephson-Mechanical Coupling

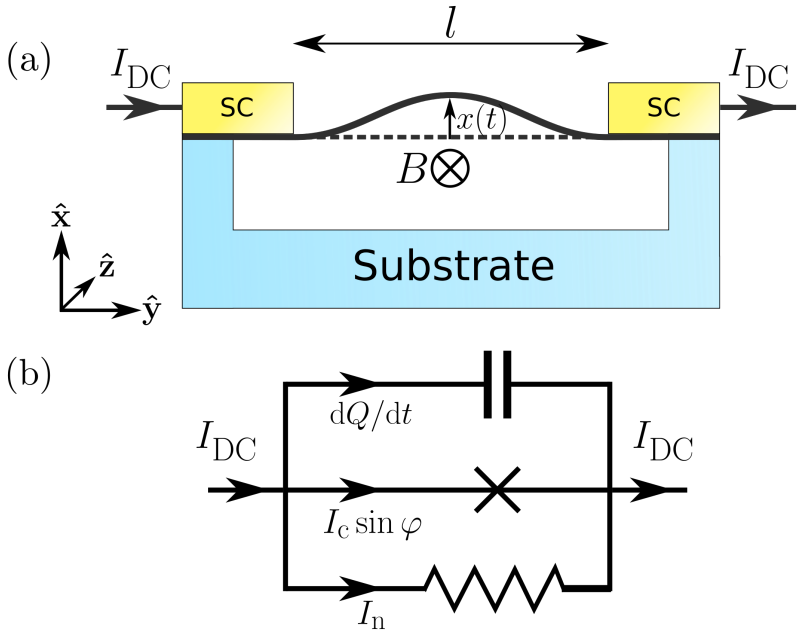

Figure 15: (a) Electromechanical resonator suspended between two superconducting contacts above a substrate. The system is biased with a constant current I_{DC} and vibrates in the presence of an in-plane magnetic field B. A constant back-gate voltage applied to the substrate can be used to tune the mechanical resonant frequency. (b) Equivalent circuit of the RCSJ model. Current may flow through either resistive, capacitive or supercurrent channels. Mechanical oscillations produce an extra electromotive force that redistributes the current through the channels.

In the previous chapter we studied the Josephson effect in detail. We saw how a Josephson supercurrent $I_c \sin\varphi$ can flow through a weak link between two superconducting electrodes, and saw that when a voltage drop V is present between the two electrodes this supercurrent becomes AC with a frequency $d\varphi/dt = 2eV/\hbar$. In this chapter we will investigate new effects that arise when the weak link is suspended and allowed to oscillate due to electromechanical coupling between the Josephson supercurrent and its mechanical motion.

By means of numerical as well as analytical investigations, we show how existing experimental setups can be used to induce and detect high-frequency mechanical oscillations in suspended weak links using purely DC current bias conditions. Exploiting a setup that allows one to tune the coupling strength between electronic and mechanical degrees of freedom, we explore the Josephson effect in regimes that have not been studied before, revealing several features in the DC I-V characteristic. Among them we analyze Shapiro step features that appear for weak electromechanical coupling as well as new mechanically induced hysteresis loops. We unveil that

for strong coupling these new Shapiro steps collapse to a zero voltage state with a sudden mechanical-induced retrapping due to energy being subtracted from the electronic system by the oscillations. Accessing the strong coupling regime thus results in a dramatic shift in the retrapping current of up to 50%. We reveal how the crossover between the weak and strong coupling regimes is intimately related to the quality factor of the resonator. Remarkably, our predictions suffice to unveil all the fundamental properties of the resonator, i.e. not just its proper frequency but also the quality factor, allowing their direct experimental measurements by simply recording the DC I-V curve without any additional measurement setup.

4.1 Model

We analyze theoretically a nanomechanical resonator of length l suspended between two superconducting contacts and biased by a DC current I_{DC} [see Fig. 15(a)]. The suspended resonator is subject to an in-plane magnetic field B that allows one to tune the coupling between the electronic current and the fundamental flexural deformation mode via the Lorentz force. The proposed device behaves as a Josephson weak link and thus allows us to explore how the Josephson junction dynamics of the previous section are modified when coupled to mechanical vibrations. This rather standard setup can be realised experimentally in various ways using different suspended resonators, e.g. nanowires [20], one dimensional carbon nanotubes (CNTs) [63–67] or ultra-thin two-dimensional materials like graphene [68, 69] and transition metal dichalcogenides [70].

The essential idea is to enter the running state so that there is an AC supercurrent $I_{\mathrm{c}} \sin\varphi$ whose frequency can be matched to the resonance frequency ω_0 of the resonator's fundamental flexural mode by the Josephson relation $\mathrm{d}\varphi/\mathrm{d}t = 2eV/\hbar = \omega_0$. The applied in-plane magnetic field can then exert a Lorentz force on the supercurrent which will activate out of plane mechanical vibrations. This idea has been explored previously in the simple voltage bias case [12, 13], but as mentioned in section 3.3, the vast majority of Josephson junction experiments are done with a current bias since the current of a low resistance device is fixed by the resistance of the external circuit [25, 60]. Here we consider the more realistic current bias case. Obviously in this case we cannot match the voltage to the resonance frequency directly, but we can choose the bias current so that the system develops a time averaged voltage $\langle V \rangle$ such that we reach the resonance condition

$$\langle V \rangle = V_0 = \frac{\hbar\omega_0}{2e}, \tag{123}$$

leading to forced amplification of oscillations.

4.2 Achieving Resonance

There are two main problems that must be overcome in order to activate mechanical oscillations in the current bias case.

- How can we obtain an AC electronic current through the device if the total bias current is DC?
- In most devices the mechanical resonance frequency is much lower than the characteristic frequency of the Josephson junctions i.e. $\omega_0 < \omega_c$ ($\omega_0/\omega_c \approx 10^{-3}$ for graphene and nanowire devices [68, 69, 71, 72] and $\omega_0/\omega_c \approx 0.1$ for carbon nanotubes [27, 63–67, 73]). How can we reach low enough voltages to reach the resonance condition Eq. (123)?

Pleasingly, both difficulties may be overcome by ensuring our device is in the underdamped ($\beta_c \gg 1$) regime.

The first problem may be overcome by realising that the displacement current is not carried by charge carriers through the device but is a result of charge accumulation at the superconducting interfaces, this is the effective capacitor in the RCSJ model. The total *electronic* current which will experience the Lorentz force is thus given only by the supercurrent and normal current contributions. As discussed in section 3.3.3, in the underdamped limit the AC supercurrent is compensated mostly by the displacement current, leaving a normal current / voltage which is strongly DC. This results in a strongly AC electronic current which can be exploited to activate mechanical vibrations, despite using a DC current bias.

The second problem may be overcome if we recall that in the underdamped case there is a hysteresis in the junction's I-V characteristic which allows us to decrease the current from above I_c and remain in the running state until a retrapping current at $I_r = 4I_c/\pi\sqrt{\beta_c}$. In this way much lower voltages may be achieved, with the lowest possible being of the order

$$I_r R \sim \frac{\hbar\omega_p}{2e}, \tag{124}$$

where $\omega_p = \sqrt{2eI_c/\hbar C}$ is the plasma frequency of the junction. Thus, as long as we satisfy the important condition

$$\omega_0 \gtrsim \omega_p, \tag{125}$$

then the junction is underdamped enough to reach the resonant condition on the decreasing current path. This is illustrated by Fig. 16.

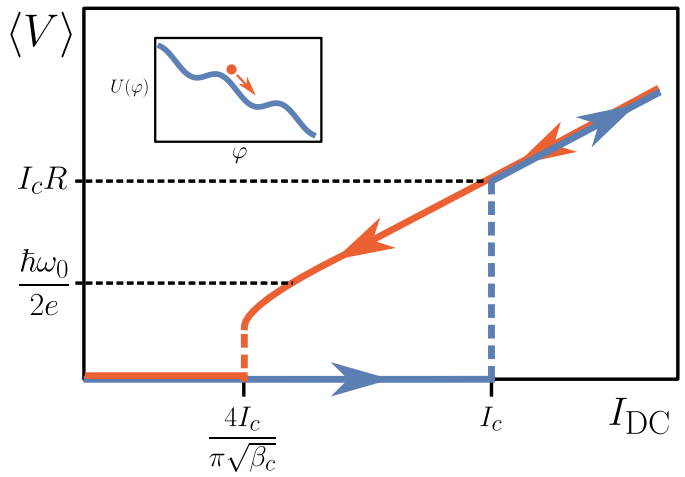

Figure 16: Sketch of an I-V curve for an underdamped junction. The voltage $V_0 = \hbar\omega_0/2e$ needed to activate mechanical vibrations in our setup is typically less than the characteristic voltage I_cR and thus cannot be reached on the increasing current path (blue line). However if the junction is underdamped enough, we can exploit the hysteresis and reach lower voltages, and thus the resonant condition, on the decreasing current path (red line).

In terms of β_c the above condition can be written as

$$\beta_c \gtrsim \left(\frac{\omega_c}{\omega_0}\right)^2, \tag{126}$$

but from an experimental point of view, one should increase the capacitance above some threshold value

$$C \gtrsim \frac{2eI_c}{\hbar\omega_0^2}. \tag{127}$$

Fortunately, typical graphene and CNT based suspended Josephson weak links operate in this underdamped regime with $\beta_c \sim 10 - 100$ [71–73]. In any case, the capacitance can always be increased by connecting the junction in parallel with an external capacitor [74].

4.3 Equations of Motion

We will write down the equations of motion of our system by using a modification of the familiar RCSJ model discussed in Section 3.2. The presence of an in-plane magnetic field has two major effects. First, it generates a Lorentz force on the electronic currents which induces mechanical oscillations. These in turn produce an additional electromotive force across the weak link that redistributes the current through the channels.

Referring to our model Fig. 15(a), the electric field between the superconductors

may be expressed as $\mathbf{E} = Q/Cl\,\hat{\mathbf{y}}$ with $\hat{\mathbf{y}}$ the direction of positive current flow and Q the charge accumulation at the superconducting interface, while the in-plane magnetic field is $\mathbf{B} = B\,\hat{\mathbf{z}}$. Due to the oscillations of the weak link the charge carriers acquire a transverse velocity $\mathbf{v} = \mathrm{d}x/\mathrm{d}t\,\hat{\mathbf{x}}$ that couples to the magnetic field to produce an electromotive force. Here we use the approximation that the weak link is displaced uniformly, including the spatial profile simply modifies the coupling strength by a factor of order unity. The normal current density is then

$$\mathbf{J}_\mathrm{n} = \sigma_\mathrm{n}(\mathbf{E} + \mathbf{v} \times \mathbf{B}) = \frac{\sigma_\mathrm{n}}{l}\left(\frac{Q}{C} - Bl\frac{\mathrm{d}x}{\mathrm{d}t}\right)\hat{\mathbf{y}}, \tag{128}$$

with σ_n the conductivity of the normal metal. In terms of the resistance, the normal current is given by

$$I_\mathrm{n} = \frac{1}{R}\left(V - Bl\frac{\mathrm{d}x}{\mathrm{d}t}\right), \tag{129}$$

where V is the voltage drop measured across the device given by

$$V = \int \mathbf{E} \cdot \mathbf{dl} = \frac{Q}{C}. \tag{130}$$

The supercurrent may still be expressed as

$$I_\mathrm{s} = I_\mathrm{c} \sin\varphi, \tag{131}$$

However referring to the derivation given in Section 3.2, the gauge-invariant phase φ is no longer given simply by ϕ, the phase difference between the macroscopic wave functions of the two superconductors, but instead the two are related by

$$\varphi = \phi - \frac{2e}{\hbar}\int \mathbf{A} \cdot \mathbf{dl}, \tag{132}$$

where $\mathbf{A}$ is the vector potential and the line integral is taken along the weak link. We also showed that ϕ evolves in time according to $\mathrm{d}\phi/\mathrm{d}t = 2eV/\hbar$ so that φ evolves in time as

$$\frac{\mathrm{d}\varphi}{\mathrm{d}t} = \frac{2e}{\hbar}\left(V - \frac{\mathrm{d}}{\mathrm{d}t}\int \mathbf{A} \cdot \mathbf{dl}\right). \tag{133}$$

In our case we can choose the gauge $\mathbf{A} = Bx'\hat{\mathbf{y}}$. Here x' is a spatial position, whereas x is the displacement of the weak link, of course when we perform the integral we integrate over the line $x' = x$. Since $\mathbf{dl} = dy\hat{\mathbf{y}}$ and we integrate over the length l of

the weak link, we obtain

$$\frac{\mathrm{d}\varphi}{\mathrm{d}t} = \frac{2e}{\hbar}\left(V - Bl\frac{\mathrm{d}x}{\mathrm{d}t}\right). \tag{134}$$

Note that in our case **A** itself is not time dependent, but the path over which we integrate is since the weak link is oscillating.

The displacement current is still given by

$$I_\mathrm{d} = \frac{\mathrm{d}Q}{\mathrm{d}t} = C\frac{\mathrm{d}V}{\mathrm{d}t}, \tag{135}$$

so that we can finally write the current conservation equation as

$$I_\mathrm{DC} = I_\mathrm{c}\sin\varphi + \frac{1}{R}\left(V - Bl\frac{\mathrm{d}x}{\mathrm{d}t}\right) + C\frac{\mathrm{d}V}{\mathrm{d}t}, \tag{136}$$

which upon substitution of Eq. (134) can be written as a differential equation in φ and x

$$I_\mathrm{DC} = I_\mathrm{c}\sin\varphi + \frac{\hbar}{2eR}\frac{\mathrm{d}\varphi}{\mathrm{d}t} + \frac{\hbar C}{2e}\frac{\mathrm{d}^2\varphi}{\mathrm{d}t^2} + CBl\frac{\mathrm{d}^2x}{\mathrm{d}t^2}. \tag{137}$$

In comparison with the uncoupled case, an extra current emerges resulting directly from the electromechanical coupling. It is through this extra term that the oscillator affects the I-V characteristic of the weak link and allows the oscillations to be detected. In particular, during resonance this extra current oscillates with a frequency ω_0. As this scenario is analogous to the case of a Josephson weak link biased by an AC current, we may expect a Shapiro plateau to develop at a voltage $V_0 = \hbar\omega_0/2e$ when vibrations are induced.

The flexural mode of the suspended weak link is modelled mechanically as a simple harmonic oscillator[7] with mass M, resonance frequency ω_0, damping coefficient Γ_0 and quality factor $Q_\Gamma = \omega_0/\Gamma_0$. As to be seen later, anharmonic effects are irrelevant in this work as only small amplitude mechanical oscillations will be activated. Taking into account the Lorentz force exerted on the electronic currents by the magnetic field, the equation of motion of the oscillator can be written as

$$\frac{\mathrm{d}^2x}{\mathrm{d}t^2} + 2\Gamma_0\frac{\mathrm{d}x}{\mathrm{d}t} + \omega_0^2 x = \frac{Bl}{M}\left(I_\mathrm{c}\sin\varphi + I_\mathrm{n}\right). \tag{138}$$

[7]The displacements we predict are significantly larger than the zero point motion of the resonator, justifying this classical treatment.

Substituting Eq. (137) into Eq. (138), we obtain

$$\left(1+\frac{B^2}{B_0^2}\right)\frac{\mathrm{d}^2x}{\mathrm{d}t^2}+2\Gamma_0\frac{\mathrm{d}x}{\mathrm{d}t}+\omega_0^2x=\frac{Bl}{M}\left(I_{\mathrm{DC}}-\frac{\hbar C}{2e}\frac{\mathrm{d}^2\varphi}{\mathrm{d}t^2}\right). \tag{139}$$

The electromechanical coupling produces a correction to the effective oscillator mass of the form $M(B/B_0)^2$, where we introduced the magnetic field scale $B_0 = (1/l)\sqrt{M/C}$. The strength of the electromechanical coupling can then be expressed in terms of the dimensionless parameter $\mu = B/B_0$. Similarly, we introduce dimensionless quantities for the current $i_{\mathrm{DC}} = I_{\mathrm{DC}}/I_{\mathrm{c}}$, time $\tau = \omega_0 t$ and oscillator displacement $a = x/x_0 - i_{\mathrm{DC}}\mu$. Here $x_0 = B_0 I_{\mathrm{c}} l/M\omega_0^2$ is the displacement at which the restoring force equals the magnetic force scale $B_0 I_{\mathrm{c}} l$ and we have subtracted the small constant displacement arising from the force $BI_{\mathrm{DC}}l$.

In terms of these dimensionless quantities, Eqs. (137) and (139) can be rewritten as

$$i_{\mathrm{DC}} = \sin\varphi + \beta_1\dot{\varphi} + \beta_2\ddot{\varphi} + \mu\ddot{a}, \tag{140}$$

$$(1+\mu^2)\ddot{a} + \frac{2}{Q_\Gamma}\dot{a} + a = -\mu\beta_2\ddot{\varphi}. \tag{141}$$

Here $\beta_1 = \omega_0/\omega_{\mathrm{c}}$, $\beta_2 = \beta_1^2\beta_{\mathrm{c}}$ and a dot over a quantity refers to a derivative with respect to τ (recall that in our discussion of the uncoupled case we instead measured time in units of $\tau_{\mathrm{c}} = \omega_c t$). The coupled AC Josephson relation Eq. (134) can now also be written in the simple form

$$\dot{\varphi} = \frac{V}{V_0} - \frac{\mu}{\beta_2}\dot{a}. \tag{142}$$

The key experimental measurement is the DC time averaged voltage $\langle V\rangle$. Since $\langle\dot{a}\rangle$ and thus the second term of Eq. (142) have zero average, we can calculate the DC voltage in units of V_0 very simply as

$$\langle\dot{\varphi}\rangle = \frac{\langle V\rangle}{V_0}. \tag{143}$$

Eqs. (140) and (141) capture the essential aspects of the coupled Josephson-mechanical system. Their solutions and corresponding I-V characteristics obtained both numerically and analytically will be the main topic of this chapter. However first we will briefly discuss the Lagrangian and Hamiltonian that give rise to these equations, in anticipation for their use in subsequent sections.

4.4 Lagrangian Formulation

The equations of motion (137) and (138) may be derived from the Euler-Lagrange equations

$$\frac{\mathrm{d}}{\mathrm{d}t}\frac{\partial \mathcal{L}}{\partial(\mathrm{d}q_i/\mathrm{d}t)} - \frac{\partial \mathcal{L}}{\partial q_i} = -\frac{\partial P}{\partial(\mathrm{d}q_i/\mathrm{d}t)}, \tag{144}$$

with generalized coordinates $q_i = \{\varphi, x\}$ [75]. The Lagrangian $\mathcal{L}$ and dissipation function P are given by

$$\mathcal{L} = \int I_{\mathrm{DC}} V \mathrm{d}t + \frac{1}{2}CV^2 + E_{\mathrm{J}}\cos\varphi + \frac{1}{2}M\left(\frac{\mathrm{d}x}{\mathrm{d}t}\right)^2 - \frac{1}{2}M\omega_0^2 x^2, \tag{145}$$

$$P = \frac{(V - Bl\mathrm{d}x/\mathrm{d}t)^2}{2R} + M\Gamma_0\left(\frac{\mathrm{d}x}{\mathrm{d}t}\right)^2, \tag{146}$$

which upon using the Josephson relation Eq. (134) become

$$\begin{aligned}\mathcal{L} =& \frac{\hbar I_{\mathrm{DC}}}{2e}\varphi + \frac{1}{2}C\left(\frac{\hbar}{2e}\frac{\mathrm{d}\varphi}{\mathrm{d}t}\right)^2 + E_{\mathrm{J}}\cos\varphi + \frac{1}{2}(M + CB^2l^2)\left(\frac{\mathrm{d}x}{\mathrm{d}t}\right)^2 \\ & - \frac{1}{2}M\omega_0^2 x^2 + BI_{\mathrm{DC}}lx + \frac{\hbar}{2e}CBl\frac{\mathrm{d}\varphi}{\mathrm{d}t}\frac{\mathrm{d}x}{\mathrm{d}t},\end{aligned} \tag{147}$$

$$P = \frac{1}{2R}\left(\frac{\hbar}{2e}\frac{\mathrm{d}\varphi}{\mathrm{d}t}\right)^2 + M\Gamma_0\left(\frac{\mathrm{d}x}{\mathrm{d}t}\right)^2. \tag{148}$$

A dimensionless Lagrangian and dissipation function may also be defined by $\bar{\mathcal{L}} = \mathcal{L}/E_{\mathrm{J}}$ and $\bar{P} = P/E_{\mathrm{J}}\omega_0$ respectively. Using our dimensionless scales of the previous section these may be written as

$$\bar{\mathcal{L}} = \frac{1}{2}\beta_2\left(\dot{\varphi} + \frac{\mu}{\beta_2}\dot{a}\right)^2 + \cos\varphi + i_{\mathrm{DC}}\varphi + \frac{1}{2\beta_2}\left(\dot{a}^2 - a^2\right), \tag{149}$$

$$\bar{P} = \frac{1}{2}\beta_1\dot{\varphi}^2 + \frac{1}{Q_\Gamma\beta_2}\dot{a}^2, \tag{150}$$

and one may easily show that upon insertion to the Euler-Lagrange equations

$$\frac{\mathrm{d}}{\mathrm{d}\tau}\frac{\partial \bar{\mathcal{L}}}{\partial \dot{q}_i} - \frac{\partial \bar{\mathcal{L}}}{\partial q_i} = -\frac{\partial \bar{P}}{\partial \dot{q}_i}, \tag{151}$$

with $q_i = \{\varphi, a\}$, that the dimensionless equations (140) and (141) are recovered.

4.5 Hamiltonian and Energy

We may also derive the Hamiltonian of the system in the usual way

$$H = \sum_i \frac{\mathrm{d}q_i}{\mathrm{d}t} \frac{\partial \mathcal{L}}{\partial(\mathrm{d}q_i/\mathrm{d}t)} - \mathcal{L}. \tag{152}$$

where the canonical momenta $\partial\mathcal{L}/\partial(\mathrm{d}q_i/\mathrm{d}t)$ are given by

$$\frac{\partial \mathcal{L}}{\partial(\mathrm{d}\varphi/\mathrm{d}t)} = \frac{\hbar C}{2e}\left(\frac{\hbar}{2e}\frac{\mathrm{d}\varphi}{\mathrm{d}t} + Bl\frac{\mathrm{d}x}{\mathrm{d}t}\right) = \frac{\hbar}{2e}CV, \tag{153}$$

$$\frac{\partial \mathcal{L}}{\partial(\mathrm{d}x/\mathrm{d}t)} = (M + CB^2l^2)\frac{\mathrm{d}x}{\mathrm{d}t} + \frac{\hbar}{2e}CBl\frac{\mathrm{d}\varphi}{\mathrm{d}t} = M\frac{\mathrm{d}x}{\mathrm{d}t} + BlCV, \tag{154}$$

and we obtain

$$H = -\int I_{\mathrm{DC}} V \mathrm{d}t + \frac{1}{2}CV^2 - E_{\mathrm{J}}\cos\varphi + \frac{1}{2}M\left(\frac{\mathrm{d}x}{\mathrm{d}t}\right)^2 + \frac{1}{2}M\omega_0^2 x^2, \tag{155}$$

$$H = -\frac{\hbar I_{\mathrm{DC}}}{2e}\varphi + \frac{1}{2}C\left(\frac{\hbar}{2e}\frac{\mathrm{d}\varphi}{\mathrm{d}t}\right)^2 - E_{\mathrm{J}}\cos\varphi + \frac{1}{2}(M + CB^2l^2)\left(\frac{\mathrm{d}x}{\mathrm{d}t}\right)^2 + \frac{1}{2}M\omega_0^2 x^2 - BI_{\mathrm{DC}}lx + \frac{\hbar}{2e}CBl\frac{\mathrm{d}\varphi}{\mathrm{d}t}\frac{\mathrm{d}x}{\mathrm{d}t}, . \tag{156}$$

Comparing the Hamiltonian with the Lagrangian it is clear that they can also be written in the traditional forms $H = \text{k.e.} + \text{p.e.}$ and $\mathcal{L} = \text{k.e.} - \text{p.e.}$ with an effective kinetic energy

$$\text{k.e.} = \frac{1}{2}CV^2 + \frac{1}{2}M\left(\frac{\mathrm{d}x}{\mathrm{d}t}\right)^2, \tag{157}$$

and effective potential energy

$$\text{p.e.} = -\int I_{\mathrm{DC}} V \mathrm{d}t - E_{\mathrm{J}}\cos\varphi + \frac{1}{2}M\omega_0^2 x^2. \tag{158}$$

The first term in the Hamiltonian Eq. (155) is the energy of the external source, which continuously decreases in the running state as energy is supplied to the Josephson-mechanical system. Removing this term, we are left with the total energy of the system, being the energy stored by the displacement current and supercurrent,

plus the kinetic and potential energy of the oscillator.

$$E = \frac{1}{2}CV^2 - E_\mathrm{J}\cos\varphi + \frac{1}{2}M\left(\frac{\mathrm{d}x}{\mathrm{d}t}\right)^2 + \frac{1}{2}M\omega_0^2 x^2, \tag{159}$$

$$E = \frac{1}{2}C\left(\frac{\hbar}{2e}\frac{\mathrm{d}\varphi}{\mathrm{d}t}\right)^2 - E_\mathrm{J}\cos\varphi + \frac{1}{2}(M + CB^2l^2)\left(\frac{\mathrm{d}x}{\mathrm{d}t}\right)^2 + \frac{1}{2}M\omega_0^2 x^2 + \frac{\hbar}{2e}CBl\frac{\mathrm{d}\varphi}{\mathrm{d}t}\frac{\mathrm{d}x}{\mathrm{d}t}. \tag{160}$$

The Hamiltonian and energy may both be put in dimensionless forms $\bar{H} = H/E_\mathrm{J}$ and $\bar{E} = E/E_\mathrm{J}$ as follows

$$\bar{H} = \frac{1}{2}\beta_2\left(\dot{\varphi} + \frac{\mu}{\beta_2}\dot{a}\right)^2 - \cos\varphi - i_\mathrm{DC}\varphi + \frac{1}{2\beta_2}\left(\dot{a}^2 + a^2\right), \tag{161}$$

$$\bar{E} = \frac{1}{2}\beta_2\left(\dot{\varphi} + \frac{\mu}{\beta_2}\dot{a}\right)^2 - \cos\varphi + \frac{1}{2\beta_2}\left(\dot{a}^2 + (a + i_\mathrm{DC}\mu)^2\right). \tag{162}$$

It should be noted that in our definition $a = x/x_0 - i_\mathrm{DC}\mu$ we removed the slack due to the constant force $BI_\mathrm{DC}l$. This results in extra constant terms in the dimensionless forms of the Lagrangian and Hamiltonian which may be discarded since the same equations of motion are obtained. Finally we note that the energy may be split up into three contributions $\bar{E} = \bar{E}_\varphi + \bar{E}_\mathrm{m} + \bar{E}_\mathrm{c}$, being the terms that depend on φ (the 'electronic energy')

$$\bar{E}_\varphi = \frac{1}{2}\beta_2\dot{\varphi}^2 - \cos\varphi, \tag{163}$$

the terms that depend on a (the 'mechanical energy')

$$\bar{E}_\mathrm{m} = \frac{1}{2\beta_2}\left((1+\mu^2)\dot{a}^2 + (a + i_\mathrm{DC}\mu)^2\right), \tag{164}$$

and the terms that couple them (the 'coupling energy')

$$\bar{E}_\mathrm{c} = \mu\dot{a}\dot{\varphi}. \tag{165}$$

The rate of energy change is given by

$$\frac{\mathrm{d}\bar{E}}{\mathrm{d}\tau} = i_\mathrm{DC}\dot{\varphi} - \beta_1\dot{\varphi}^2 - \frac{2}{Q_\Gamma\beta_2}\dot{a}^2 \tag{166}$$

where the first term on the right-hand side is the power supplied by the external current while the second and third terms describe energy losses due to Joule heating and the intrinsic damping of the resonator. When the system reaches a steady state,

the supplied energy must be completely dissipated on average, i.e.,

$$i_{\rm DC}\langle\dot{\varphi}\rangle = \beta_1\langle\dot{\varphi}^2\rangle + \frac{2}{Q_\Gamma\beta_2}\langle\dot{a}^2\rangle. \tag{167}$$

This important energy balance equation is obeyed by any steady state solution, and will be an important test for any analytical treatment. In the uncoupled case at large currents, it simply leads to the Ohmic solution $\langle\dot{\varphi}\rangle \approx i_{\rm DC}/\beta_1$. Upon coupling to mechanical oscillations, the intrinsic damping of the oscillator must also be considered. Energy is transferred from the electronic subsystem to mechanical oscillations leading to measurable effects on the total voltage across the device.

4.6 Weak-Coupling Limit

Due to the highly nonlinear nature of Eqs. (140) and (141), their solutions are expected to display strong dependence on initial conditions. A general exact analytical solution cannot be achieved. In what follows, we first numerically solve the equations to establish the characteristic I-V curve. The properties of the numerical solutions will then suggest an ansatz for a semianalytical treatment of the problem leading to a good agreement with the numerically established I-V curve.

We numerically solve Eqs. (140) and (141) using a fourth order Runge-Kutta method. The experimentally tunable parameters are the input current $i_{\rm DC}$ and the coupling parameter μ, while the directly measurable quantity is the average voltage, $\langle V\rangle/V_0 = \langle\dot{\varphi}\rangle$. All parameters other than $i_{\rm DC}$ and μ are sample specific, as such we use the following parameters which are consistent with previously studied CNT devices [27, 63–67, 73]: $I_c = 10$nA, $R = 330\Omega$, $\beta_c = 200$, $\omega_0 = 1$GHz, $Q_\Gamma = 10^3$, $M = 10^{-20}$kg, $l = 1\mu$m. All other parameters may be derived from these, including the important dimensionless quantities, $\beta_1 = 0.1$, $\beta_2 = 2$ and the dimensional scales $V_0 = 0.3\mu$V, $B_0 = 10$T, $x_0 = 10$pm.

Unless otherwise stated, the numerical simulations shown here will be carried out with the above choice of parameters. While these are typical parameters, state of the art devices may have larger quality factors $Q_\Gamma = 10^6$ and resonance frequencies $\omega_0 = 10$GHz which allow measurements to be made at higher temperatures and lower magnetic fields, as will be discussed in later sections. We have verified that the general features of our analysis are present for a wide range of parameters as long as the resonance region can be reached, i.e. if the junction is underdamped enough. All simulations were performed at zero temperature with no noise currents, the limits of validity of this approximation and the possible effects of temperature are discussed in a later section.

For now we will look at cases where μ is not too large, the weak coupling regime, where the predominant feature is a Shapiro-like plateau. If μ exceeds some critical value, we enter a strong coupling regime that is characterized by sudden retrapping into the trapped state. The numerical value of μ where this strong coupling regime is reached will be discussed in detail later when we look at the semianalytical treatment.

4.6.1 Mechanically Induced Shapiro Steps

As Eqs. (140) and (141) are highly non-linear, different states can be accessed depending on how the free parameters i_{DC} and μ are varied. This was already seen in the uncoupled case $\mu = 0$ in underdamped junctions where the decreasing and increasing current paths yielded different I-V curves. Now we are free to take any path in the space (i_{DC}, μ) when performing an experiment and each choice can yield wildly different results. The simplest choice is a decreasing current path with a fixed coupling μ, and that is what we shall use in this section, moving on to some more complicated procedures later.

We employ continuous initial conditions whereby we start with $i_{\mathrm{DC}} > 1$, where the only solution is the running state $\langle\dot{\varphi}\rangle \approx i_{\mathrm{DC}}/\beta_1$, and gradually decrease i_{DC} in small increments, at each point using as initial conditions the results for $a, \varphi, \dot{a}$ and $\dot{\varphi}$ from the simulation for the previous value of i_{DC} after transients have decayed. This adequately models the quasi-static process in which the characteristic time scales of the system are much shorter than the time over which the impressed current i_{DC} is experimentally varied. This process is then repeated to obtain the I-V curves for different values of μ.

The I-V curves for four different values of μ are plotted in Fig. 17(a), along with corresponding plots of the root mean square displacement $x_{\mathrm{rms}} = \sqrt{\langle x^2\rangle}$ in Fig. 17(b). The dashed part of the curves are unphysical, showing transitions where $\langle V\rangle$ and x_{rms} abruptly jump from one value to another. For $\mu = 0$ (blue line) we recover the usual uncoupled decreasing current path discussed extensively in the previous chapter. However as μ increases we see that a plateau develops at $\langle V\rangle = V_0 = \hbar\omega_0/2e$, where the supercurrent frequency is locked to the mechanical resonance frequency. In fact we see from the corresponding values of x_{rms} that this plateau is associated with a strong mechanical resonance of the oscillator, with higher currents deeper in the plateau corresponding to stronger oscillations. The drop on to the plateau is not continuous but an abrupt transition, and similarly the oscillator amplitude jumps up from close to zero to a finite value in a very small current range. Increasing the coupling μ leads to an increase in the width of the

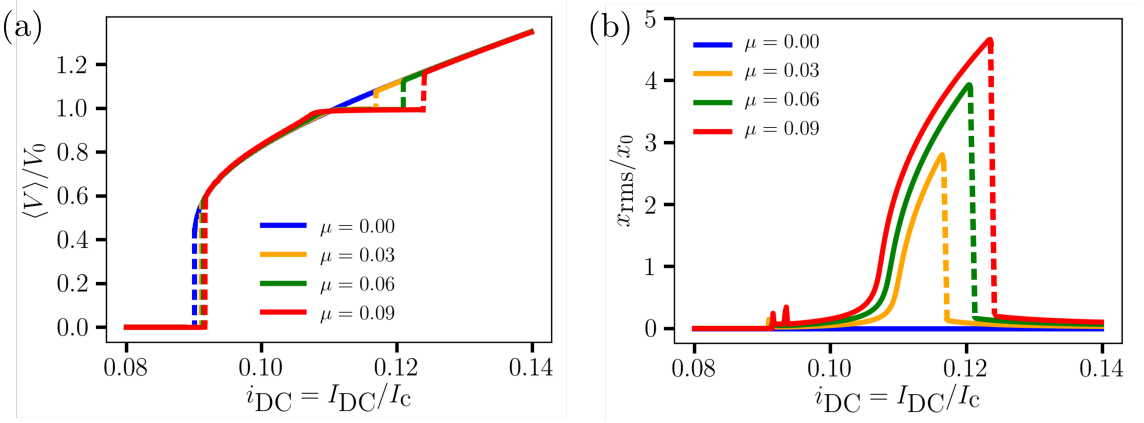

Figure 17: (a) DC voltage $\langle V\rangle$ and (b) root mean square mechanical oscillation $x_{\rm rms} = \sqrt{\langle x^2\rangle}$ as functions of the applied current $i_{\rm DC} = I_{\rm DC}/I_{\rm c}$ for a simple decreasing current experiment, obtained by numerically solving Eqs. (140) and (141) with $\beta_1 = 0.1$, $\beta_2 = 2$, $Q_\Gamma = 10^3$. Results are shown for four different magnetic field coupling values $\mu = B/B_0$. For $\mu = 0$ (blue line) we recover the usual uncoupled decreasing current path, but for finite μ a Shapiro-like plateau develops at $\langle V\rangle = V_0$ where the supercurrent and mechanical resonance frequencies are locked. The plateau widens with increasing coupling and coincides with a resonant peak in $x_{\rm rms}$, with the oscillations being stronger with higher currents deeper into the plateau and with stronger coupling. Two additional small resonant peaks are visible at low currents, these correspond to sub-harmonic Shapiro plateaus at 1/2 and 2/3 of ω_0 and will be discussed further in section 4.10.

plateau and a corresponding increase in the strength of the oscillations $x_{\rm rms}$. This behaviour is expected from the form of Eqs. (140) and (141), with the term $-\mu\beta_2\ddot{\varphi}$ in Eq. (141) acting as a forcing term that stimulates the oscillator into resonance when the resonance condition is met. During resonance the term $\mu\ddot{a}$ in Eq. (140) then acts as an effective AC current term producing the Shapiro-like plateau.

This locking of frequencies on the Shapiro plateau may be seen in more detail by looking at the time evolution $a(\tau)$ and $\dot{\varphi}(\tau)$ of a particular solution. Fig. 18 shows the solution for $\mu = 0.1$ at the current value $i_{\rm DC} = 0.125$ where the current has just been decreased on to the plateau solution. After a long transient period, the system enters a resonant state and mechanical oscillations increase in amplitude. The oscillations continue to increase but eventually saturate, while the average supercurrent frequency (and thus voltage) $\langle\dot{\varphi}\rangle = \langle V\rangle/V_0$ lowers from an approximately Ohmic value $\langle\dot{\varphi}\rangle \approx i_{\rm DC}/\beta_1$ to being locked at the mechanical resonant frequency $\langle\dot{\varphi}\rangle = 1$, giving rise to the Shapiro plateau.

Thus we see that it is possible to activate mechanical oscillations in a suspended Josephson weak link using only a DC current bias. By measuring the I-V characteristic of such a junction it is then possible to detect these oscillations, and measure

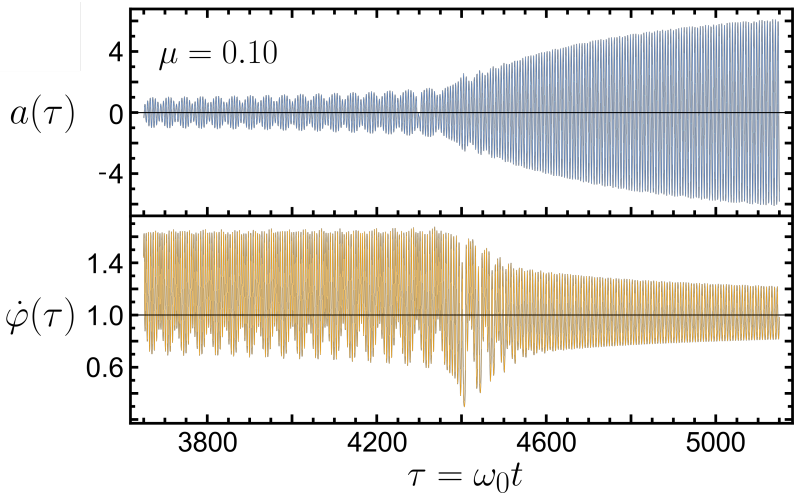

Figure 18: Time evolution $a(\tau)$ and $\dot{\varphi}(\tau)$ for the solution to Eqs. (140) and (141) when $\mu = 0.1$ and at the current value $i_{\rm DC} = 0.125$ where the current has just been decreased on to the plateau solution. After a long transient the oscillations $a(\tau)$ increase and the supercurrent frequency $\langle\dot{\varphi}\rangle$ becomes locked to the resonant frequency, giving rise to the Shapiro plateau.

the mechanical frequency of the junction ω_0 by measuring the voltage $V_0 = \hbar\omega_0/2e$ at which the mechanically induced Shapiro plateau develops.

The Shapiro plateau found for our realistic parameters in Fig. 17 has a width in current of the order $\sim 0.01 I_{\rm c} = 0.1$nA for magnetic fields $B \sim 1$T. This plateau is measurable with state of the art devices, but we will now see that it is possible to obtain much larger plateaus at the same coupling strengths by exploiting new hysteresis loops that develop in our highly non-linear system.

4.6.2 Mechanically Induced Hysteresis

In the previous section we looked at a simple decreasing current experiment at fixed coupling. We now explore what happens when we first decrease the current to reach the Shapiro plateau, but then increase the current again. One finds that instead of retracing the same path there is a mechanically induced hysteresis whereby the system remains in the plateau state until much larger current values are reached. We shall refer to this procedure as the increasing current path, although this should be understood as increasing from an already finite voltage state, if one increased the current from a zero voltage state we would of course stay at zero voltage until reaching $I_{\rm c}$.

The I-V curves obtained on this increasing current path are plotted in Fig. 19(a), with corresponding plots of the root mean square displacement $x_{\rm rms} = \sqrt{\langle x^2\rangle}$ in Fig. 19(b). The dashed lines again show abrupt transitions. For $\mu = 0$ (blue line) we

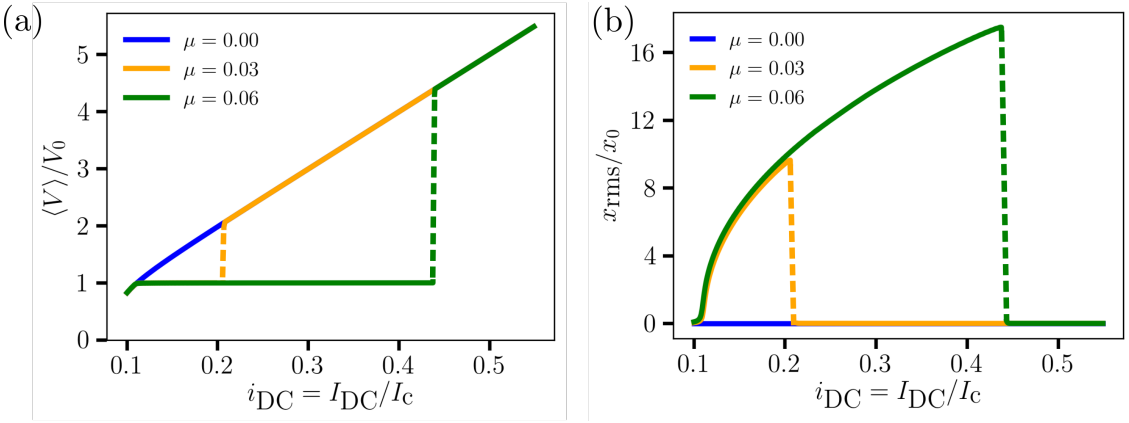

Figure 19: (a) DC voltage $\langle V \rangle$ and (b) root mean square mechanical oscillation $x_{\mathrm{rms}} = \sqrt{\langle x^2 \rangle}$ as functions of the applied current $i_{\mathrm{DC}} = I_{\mathrm{DC}}/I_{\mathrm{c}}$ for the increasing current path described in the main text, obtained by numerically solving Eqs. (140) and (141) with $\beta_1 = 0.1$, $\beta_2 = 2$, $Q_\Gamma = 10^3$. Results are shown for three different magnetic field coupling values $\mu = B/B_0$. For $\mu = 0$ (blue line) we retrace the same path as the decreasing current path, but for finite μ we explore much larger plateaus with larger oscillation amplitudes.

retrace the same path as the decreasing current path, but for finite μ we explore much larger plateaus. For example considering the case $\mu = 0.06$ (green line), a plateau of width $0.3I_{\mathrm{c}}$ is obtained by exploiting the hysteresis in the increasing current path, compared to a plateau width $0.01I_{\mathrm{c}}$ in the simple decreasing current path. This represents a huge improvement in terms of the experimental feasibility of measuring the plateau. The mechanical oscillation amplitude continues to increase as we go deeper into the plateau, with the increasing current path producing oscillations with roughly four times larger amplitude than the decreasing current path.

4.7 Analytical Ansatz

Having explored these mechanically induced Shapiro steps and hysteresis loops by numerically solving Eqs. (140) and (141), we now give an analytical solution and show in detail how these interesting new phenomena emerge. We choose a simple ansatz for a steady state solution. For $\varphi(\tau)$ we choose

$$\varphi = \varphi_0 + \omega\tau - \frac{g}{\omega}\cos(\omega\tau), \tag{168}$$

which is simply a statement that the voltage $\dot{\varphi}$ has a constant average ω with a sinusoidal correction of amplitude g

$$\dot{\varphi} = \omega + g\sin(\omega\tau). \tag{169}$$

For the mechanical oscillator $a(\tau)$ we again choose a simple sinusoidal ansatz, with amplitude A and a phase lag γ compared to the voltage

$$a = A\sin(\omega\tau + \gamma). \tag{170}$$

Our task is then to substitute these into Eqs. (140) and (141) and solve for the five unknowns $\omega, \varphi_0, g, A, \gamma$. We will find the latter four as functions of ω and then be left with an equation involving only ω which we can solve.

Starting with the mechanical equation Eq. (141), after substitution we obtain

$$[1-(1+\mu^2)\omega^2]\sin(\omega\tau+\gamma) + \frac{2\omega}{Q_\Gamma}\cos(\omega\tau+\gamma) = -\frac{\mu\beta_2 g\omega}{A}\cos(\omega\tau). \tag{171}$$

We can then use the trigonometric addition formulae and match the terms proportional to $\sin(\omega\tau)$ and $\cos(\omega\tau)$ from which we obtain

$$[1-(1+\mu^2)\omega^2]\cos\gamma - \frac{2\omega}{Q_\Gamma}\sin\gamma = 0, \tag{172}$$

and

$$[1-(1+\mu^2)\omega^2]\sin\gamma + \frac{2\omega}{Q_\Gamma}\cos\gamma = -\frac{\mu\beta_2 g\omega}{A}, \tag{173}$$

respectively. Using $\sin^2\gamma + \cos^2\gamma = 1$, Eq. (172) then gives γ in terms of ω

$$\sin\gamma = \frac{1-(1+\mu^2)\omega^2}{\sqrt{\kappa}}, \tag{174}$$

$$\cos\gamma = \frac{2\omega/Q_\Gamma}{\sqrt{\kappa}}, \tag{175}$$

where κ is defined by

$$\kappa = [1-(1+\mu^2)\omega^2]^2 + (2\omega/Q_\Gamma)^2. \tag{176}$$

Eq. (173) then gives A in terms of g and ω,

$$A = -\frac{\mu\beta_2 g\omega}{\sqrt{\kappa}}. \tag{177}$$

Notice that if we had instead chosen the negative square root for κ, we would change $A \to -A$ and $\gamma \to \gamma + \pi$ which yields the same solution $a(\tau)$.

Turning now to the electronic equation Eq. (140), substituting our ansatz we

obtain

$$i_{\mathrm{DC}} = \sin\varphi + \beta_1[\omega + g\sin(\omega\tau)] + \beta_2 g\omega\cos(\omega\tau) - \mu A\omega^2\sin(\omega\tau+\gamma). \tag{178}$$

To expand out the $\sin\varphi$ term we can write

$$\sin\varphi = \sin[\varphi_0 + \omega\tau - (g/\omega)\cos(\omega\tau)] \tag{179}$$
$$= \mathrm{Im}\left\{e^{i(\varphi_0+\omega\tau)}e^{-i(g/\omega)\cos(\omega\tau)}\right\} \tag{180}$$

and then use the Jacobi-Anger identity

$$e^{iz\cos\theta} = \sum_{n=-\infty}^{+\infty} i^n \mathcal{J}_n(z)e^{in\theta}, \tag{181}$$

as we already did when looking at the regular Shapiro steps in section 3.5. We then have

$$\sin\varphi = \mathrm{Im}\left\{e^{i(\varphi_0+\omega\tau)}\sum_{n=-\infty}^{+\infty}\mathcal{J}_n\left(-\frac{g}{\omega}\right)e^{in(\omega\tau+\pi/2)}\right\}, \tag{182}$$

which after transforming $n \to -n$ and using the identity $\mathcal{J}_{-n}(-z) = \mathcal{J}_n(z)$ finally becomes

$$\sin\varphi = \sum_{n=-\infty}^{+\infty}\mathcal{J}_n\left(\frac{g}{\omega}\right)\sin[\varphi_0 + \omega\tau - n(\omega\tau+\pi/2)]. \tag{183}$$

To proceed further we must make some approximations. We have already included only terms oscillating at the single frequency ω in our ansatz, keeping only these terms here we obtain

$$\begin{aligned}\sin\varphi \approx -\mathcal{J}_1\left(\frac{g}{\omega}\right)\cos\varphi_0 &+ \left[\mathcal{J}_0\left(\frac{g}{\omega}\right) + \mathcal{J}_2\left(\frac{g}{\omega}\right)\right]\cos\varphi_0\sin(\omega\tau) \\ &+ \left[\mathcal{J}_0\left(\frac{g}{\omega}\right) - \mathcal{J}_2\left(\frac{g}{\omega}\right)\right]\sin\varphi_0\cos(\omega\tau).\end{aligned} \tag{184}$$

Returning to Eq. (178) we can now match the terms proportional to $\sin(\omega\tau)$ and $\cos(\omega\tau)$ as well as the constant terms to obtain the following three relations.

$$\beta_1\omega - i_{\mathrm{DC}} - \mathcal{J}_1\left(\frac{g}{\omega}\right)\cos\varphi_0 = 0, \tag{185}$$
$$\beta_1 g - \mu A\omega^2\cos\gamma + \left[\mathcal{J}_0\left(\frac{g}{\omega}\right) + \mathcal{J}_2\left(\frac{g}{\omega}\right)\right]\cos\varphi_0 = 0, \tag{186}$$
$$\beta_2 g\omega - \mu A\omega^2\sin\gamma + \left[\mathcal{J}_0\left(\frac{g}{\omega}\right) - \mathcal{J}_2\left(\frac{g}{\omega}\right)\right]\sin\varphi_0 = 0. \tag{187}$$

In principle these three equations along with Eqs. (174), (175) and (177) suffice to determine our five unknowns but to carry on with our analytical treatment we will

have to make a further approximation to treat the Bessel functions. However there is one important relation we can obtain that is worth showing is true without any need of approximation. We proceed by combining Eqs. (185) and (186) to eliminate $\cos\varphi_0$.

$$\beta_1 g - \mu A\omega^2 \cos\gamma + (\beta_1\omega - i_{\mathrm{DC}}) \left(\frac{\mathcal{J}_0\left(\frac{g}{\omega}\right) + \mathcal{J}_2\left(\frac{g}{\omega}\right)}{\mathcal{J}_1\left(\frac{g}{\omega}\right)} \right), \tag{188}$$

then inserting A from Eq. (177), $\cos\gamma$ from Eq. (175), and using the Bessel function recurrence relation

$$\frac{\mathcal{J}_{n-1}(z) + \mathcal{J}_{n+1}(z)}{\mathcal{J}_n(z)} = \frac{2n}{z}, \tag{189}$$

we obtain g as a function of ω

$$g^2 = \frac{2\omega(i_{\mathrm{DC}} - \beta_1\omega)}{\beta_1 + \mu^2\beta_2\omega^3(2\omega/Q_\Gamma)/\kappa}. \tag{190}$$

This is an important relation because we can now show that it is equivalent to the energy conservation relation Eq. (167) as follows

$$\begin{aligned} i_{\mathrm{DC}}\langle\dot{\varphi}\rangle &= \beta_1\langle\dot{\varphi}^2\rangle + \frac{2}{Q_\Gamma\beta_2}\langle\dot{a}^2\rangle, \\ i_{\mathrm{DC}}\omega &= \beta_1\left(\omega^2 + \frac{g^2}{2}\right) + \frac{A^2\omega^2}{Q_\Gamma\beta_2}, \\ i_{\mathrm{DC}}\omega &= \beta_1\left(\omega^2 + \frac{g^2}{2}\right) + \frac{\mu^2\beta_2 g^2\omega^4}{Q_\Gamma\kappa}, \\ 2\omega(i_{\mathrm{DC}} - \beta_1\omega) &= g^2\left(\beta_1 + \mu^2\beta_2\omega^3(2\omega/Q_\Gamma)/\kappa\right), \end{aligned} \tag{191}$$

from which we recover Eq. (190).

As promised we will make one final approximation to treat the Bessel functions and continue our progress. We already saw that in underdamped junctions the voltage is almost constant at its average value $\omega = \langle V\rangle/V_0$ with small fluctuations of amplitude g. A reasonable assumption is then $g/\omega \ll 1$, allowing us to expand the Bessel functions in the small argument limit, i.e.,

$$\mathcal{J}_n(z) \approx \frac{1}{n!}\left(\frac{z}{2}\right)^n. \tag{192}$$

Keeping only terms up to first order in g/ω our six equations (174), (175), (177),

(185), (186) and (187) are then

$$\sin\gamma = \frac{1-(1+\mu^2)\omega^2}{\sqrt{\kappa}}, \tag{193}$$

$$\cos\gamma = \frac{2\omega/Q_\Gamma}{\sqrt{\kappa}}, \tag{194}$$

$$A = -\frac{\mu\beta_2 g\omega}{\sqrt{\kappa}}, \tag{195}$$

$$\beta_1\omega - i_{\mathrm{DC}} - \frac{g}{2\omega}\cos\varphi_0 = 0, \tag{196}$$

$$\beta_1 g - \mu A\omega^2\cos\gamma + \cos\varphi_0 = 0, \tag{197}$$

$$\beta_2 g\omega - \mu A\omega^2\sin\gamma + \sin\varphi_0 = 0, \tag{198}$$

with κ a function of ω given by Eq. (176). Combining Eqs. (196) and (197) again gives Eq. (190) so that γ, A and g are all determined as functions of ω. All that is left is to eliminate φ_0 by rearranging Eqs. (197) and (198) for $\cos\varphi_0$ and $\sin\varphi_0$ respectively and writing $\sin^2\varphi_0 + \cos^2\varphi_0 = 1$ as

$$(\mu A\omega^2\cos\gamma - \beta_1 g)^2 + (\mu A\omega^2\sin\gamma - \beta_2 g\omega)^2 = 1. \tag{199}$$

After inserting the relevant expressions for the other unknowns, we obtain the following eighth order polynomial for the DC voltage $\omega = \langle V\rangle/V_0$

$$2\omega(\beta_1\omega - i_{\mathrm{DC}})D_2 + \beta_1\kappa + \mu^2\beta_2\omega^3 2\omega/Q_\Gamma = 0, \tag{200}$$

where we have introduced a new quantity D_2 (the reason for this name will become apparent)

$$D_2 = 2\mu^2\beta_2\omega^3\left(\beta_1\frac{2\omega}{Q_\Gamma} + \beta_2\omega[1-\omega^2(1+\mu^2)]\right) + (\beta_1^2 + \beta_2^2\omega^2)\kappa + (\mu^2\beta_2\omega^3)^2. \tag{201}$$

In principle the polynomial Eq. (200) can be solved for ω as a function of i_{DC} and thus produce the I-V curve, but the polynomial is eighth order and thus does not have a general analytical solution. A smarter approach is to notice that the current i_{DC} appears only once in this equation and thus we can rearrange for the bias current as a function of voltage, $i_{\mathrm{DC}}(\omega)$, providing an analytical form for the I-V characteristic.

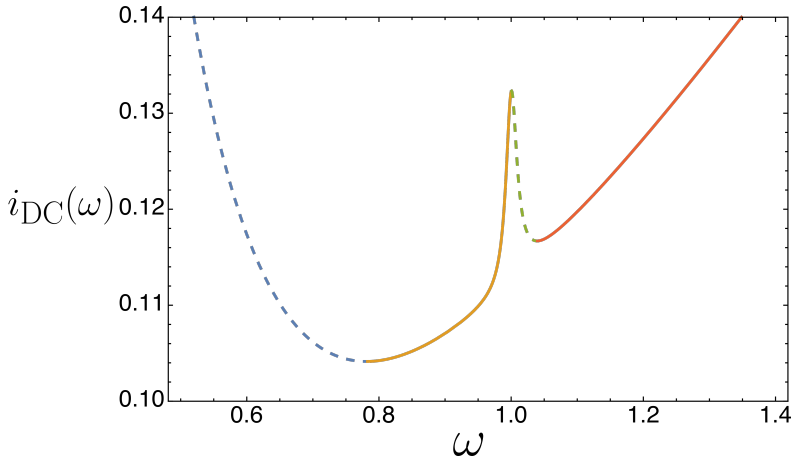

Figure 20: The current function $i_{DC}(\omega)$ [Eq. (202)] plotted for $\beta_1 = 0.1$, $\beta_2 = 2$, $Q_\Gamma = 100$ and $\mu = 0.04$. This shows the allowed values of ω for a given current i_{DC} and when the axes are flipped gives the I-V characteristic in its traditional form. Dashed lines are unphysical solutions with $\partial i_{DC}/\partial\omega < 0$. The resonant peak at $\omega = 1$ splits the I-V characteristic into two branches, an upper Ohmic branch $i_{DC} \approx \beta_1\omega$ (red line) and a lower branch that includes half of the resonant peak giving rise to the Shapiro plateau (orange line).

4.7.1 Current Function

The current function $i_{DC}(\omega)$ is thus found from rearranging Eq. (200) to be

$$i_{DC}(\omega) = \beta_1\omega + \frac{\beta_1\kappa + \mu^2\beta_2\omega^3(2\omega/Q_\Gamma)}{2\omega D_2}. \tag{202}$$

This function is plotted in Fig. 20 with the same electronic parameters as used in our numerical results, $\beta_1 = 0.1$, $\beta_2 = 2$, but with a lower quality factor $Q_\Gamma = 100$ to make it easier to see the qualitative features. As $\omega \to 0$, $i_{DC} \to \infty$ and as $\omega \to \infty$ the system becomes Ohmic $i_{DC} \to \beta_1\omega$ as is obvious from the form of Eq. (202). The main feature however is a sharp peak close to the resonance frequency, this produces a wide range of current values where the voltage is pinned very close to $\omega = 1$ i.e. $\langle V\rangle = V_0 = \hbar\omega_0/2e$, which will give rise to our Shapiro plateau.

We see that there are multiple possible values of ω for a given bias current i_{DC}. Some of these solutions may be disregarded since they give a voltage that decreases with increasing current, $\partial i_{DC}/\partial\omega < 0$, these solutions are marked with dashed lines in Fig. 20. The resonant peak at $\omega = 1$ splits the I-V characteristic into two regions, an upper branch with $\omega > 1$ which is essentially Ohmic, $i_{DC} \approx \beta_1\omega$, and a lower branch with $\omega < 1$ which contains half of the resonant peak that forms the Shapiro-like plateau. The presence of the peak thus admits multiple physical solutions for ω at a fixed current and induces a hysteresis loop.

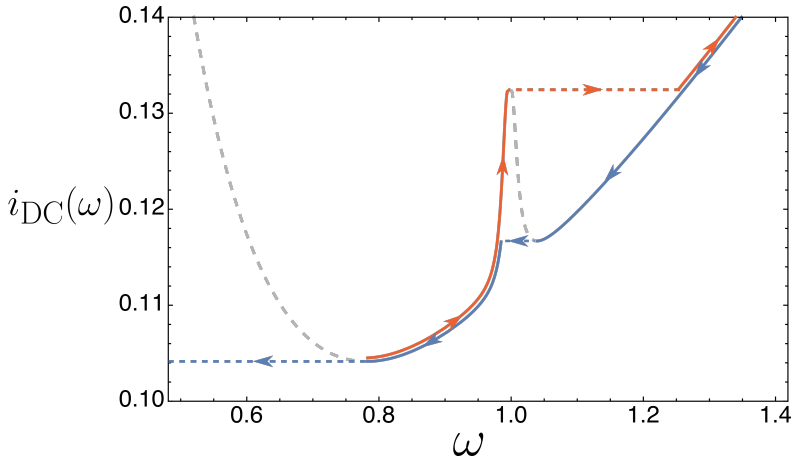

Figure 21: The electromechanical coupling when $\mu \neq 0$ induces a hysteresis loop in the I-V characteristic as a result of the resonant peak in $i_{DC}(\omega)$. On the decreasing current path (blue line) only a fraction of the resonant peak is explored producing a small Shapiro plateau. On the increasing current path (red line) however, one can reach the top of the peak producing a much larger plateau.

This hysteresis loop is shown in Fig. 21 from which we can see the origin of the difference between the decreasing and increasing current paths in our numerical treatment. On the decreasing current path (blue line) only a fraction of the resonant peak is explored producing a small Shapiro plateau. On the increasing current path (red line) however, one can reach the top of the peak producing a much larger plateau.

Fig. 22 shows $i_{DC}(\omega)$ for various coupling values μ from which we see that it consists of a μ independent profile plus the μ dependent correction that is peaked very close to $\omega = 1$. Using this fact we can write the function in the form

$$i_{DC}(\omega) = i_{DC}^{(0)}(\omega) + \delta i_{DC}(\omega), \tag{203}$$

where the μ independent profile $i_{DC}^{(0)}(\omega)$ is found simply by setting $\mu = 0$ in Eq. (202)

$$i_{DC}^{(0)}(\omega) = \beta_1 \left(\omega + \frac{1}{2\omega(\beta_1^2 + \beta_2^2\omega^2)} \right). \tag{204}$$

This function is the blue curve plotted in Fig. 22. The μ dependent correction $\delta i_{DC}(\omega)$ can be put into the form

$$\delta i_{DC}(\omega) = \frac{N_1 N_2}{D_1 D_2}, \tag{205}$$

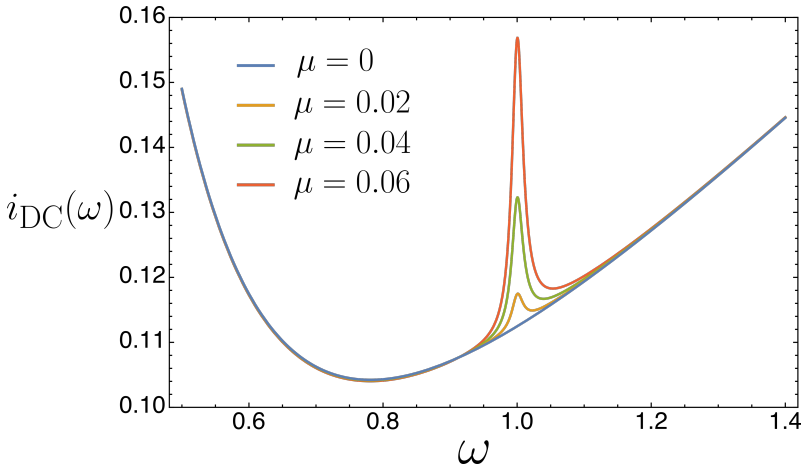

Figure 22: The function $i_{\rm DC}(\omega)$ [Eq. (202)] plotted for $\beta_1 = 0.1$, $\beta_2 = 2$, $Q_\Gamma = 100$ and $\mu = 0, 0.02, 0.04, 0.06$. The coupling μ modifies the $\mu = 0$ curve $i^{(0)}_{\rm DC}(\omega)$ (blue line) simply by the addition of a resonant peak at $\omega \approx 1$ whose height and width increase with increasing coupling. The mechanically induced Shapiro step is thus predicted to grow in size with increased coupling.

where the numerator terms N_1, N_2 and denominator terms D_1, D_2 are given by

$$N_1 = \mu^2 \beta_2 \omega^3, \tag{206}$$

$$N_2 = \beta_1 \beta_2 (\omega^2 - 1) + \omega^2 \beta_2 \left(\frac{\beta_2}{Q_\Gamma} + \frac{\beta_1 \mu^2}{2} \right) - \frac{\beta_1^2}{Q_\Gamma}, \tag{207}$$

$$D_1 = \beta_1^2 + \beta_2^2 \omega^2, \tag{208}$$

$$D_2 = (\omega^2 - 1) \left[(\beta_1^2 + \beta_2^2 \omega^2)(\omega^2 - 1) + 2\omega^2 \mu^2 \beta_1^2 \right] + \omega^4 \left(\beta_1 \mu^2 + \frac{2\beta_2}{Q_\Gamma} \right)^2 + \beta_1^2 \left(\frac{2\omega}{Q_\Gamma} \right)^2. \tag{209}$$

The function $\delta i_{\rm DC}(\omega)$ is plotted in Fig. 23, where we notice the important fact that the resonant peak is not centered at the frequency $1/\sqrt{1+\mu^2}$ as might be expected from the form of the equation of motion Eq. (141) but instead a frequency $\omega_{\rm max}$ which is much closer to the bare resonance frequency $\omega = 1$.

So far our form of $\delta i_{\rm DC}(\omega)$ is very complicated but a massive simplification occurs by performing an expansion around $\omega^2 = 1$ under the assumptions $\mu^2, 1/Q_\Gamma \ll 1$. To be more exact, we make the following perturbation

$$\omega^2 \to 1 + \epsilon \delta\omega^2, \quad \frac{1}{Q_\Gamma} \to \frac{\epsilon}{Q_\Gamma}, \quad \mu^2 \to \epsilon \mu^2, \tag{210}$$

keeping terms up to lowest order in ϵ in both the numerator and denominator. This

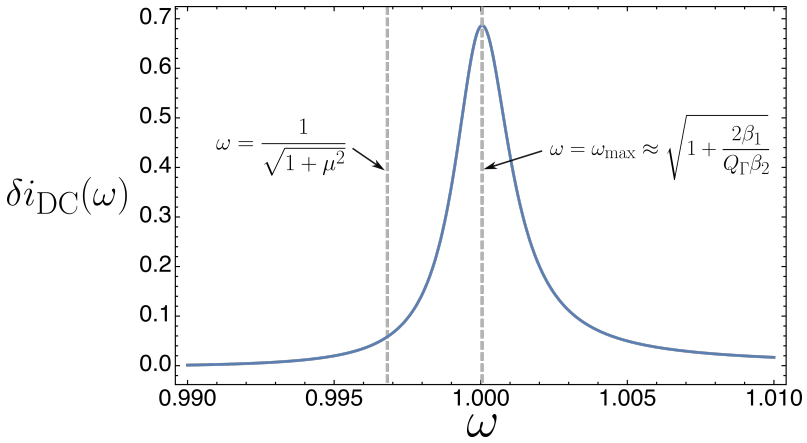

Figure 23: The function $\delta i_{\mathrm{DC}}(\omega)$ plotted with the experimentally relevant parameters $\beta_1 = 0.1$, $\beta_2 = 2$, $Q_\Gamma = 10^3$ and $\mu = 0.08$. The 'renormalized' frequency $1/\sqrt{1+\mu^2}$ plays no special role, with the peak occurring at $\omega_{\max}$ which for these parameters is very close to the bare resonance frequency $\omega = 1$.

procedure yields

$$N_1 \approx \mu^2 \beta_2, \tag{211}$$

$$N_2 \approx \beta_1\beta_2(\omega^2-1) + \frac{\beta_2^2-\beta_1^2}{Q_\Gamma} + \frac{\beta_1\beta_2\mu^2}{2}, \tag{212}$$

$$D_1 \approx \beta_1^2 + \beta_2^2, \tag{213}$$

$$D_2 \approx (\omega^2-1)\left[(\beta_1^2+\beta_2^2)(\omega^2-1) + 2\mu^2\beta_1^2\right] + \left(\beta_1\mu^2 + \frac{2\beta_2}{Q_\Gamma}\right)^2 + \beta_1^2\left(\frac{2}{Q_\Gamma}\right)^2. \tag{214}$$

We note that this approximation is equivalent to keeping only the singular terms (ω^2-1) in the exact expressions, while setting $\omega = 1$ elsewhere. Inserting these expressions into Eq. (205), $\delta i_{\mathrm{DC}}(\omega)$ can be put into the Fano form

$$\delta i_{\mathrm{DC}}(\omega) \approx \frac{\mu^2\beta_1\beta_2^2}{(\beta_1^2+\beta_2^2)^2}\left[\frac{(\omega^2-\omega_{\mathrm{Fano}}^2) + \frac{\zeta^2-1}{\zeta\Gamma}\left(\frac{\Gamma}{2}\right)^2}{(\omega^2-\omega_{\mathrm{Fano}}^2)^2 + \left(\frac{\Gamma}{2}\right)^2}\right] \tag{215}$$

where

$$\omega_{\mathrm{Fano}} = \sqrt{1 - \frac{\mu^2\beta_1^2}{\beta_1^2+\beta_2^2}}, \tag{216}$$

$$\Gamma = \frac{2\beta_1\beta_2\mu^2}{\beta_1^2+\beta_2^2} + \frac{4}{Q_\Gamma}, \tag{217}$$

and

$$\zeta = \frac{\beta_2}{\beta_1}. \tag{218}$$

The Fano line shape of $\delta i_{\mathrm{DC}}(\omega)$ is difficult to see with the realistic parameters

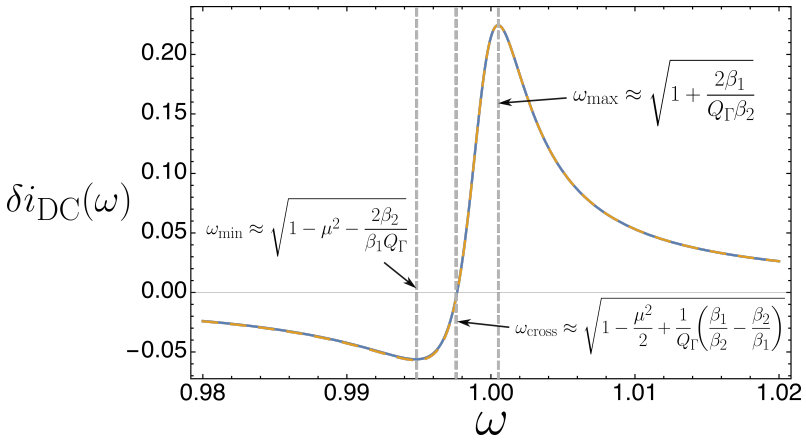

Figure 24: The function $\delta i_{\mathrm{DC}}(\omega)$ plotted with the parameters $\beta_1 = 1$, $\beta_2 = 2$, $Q_\Gamma = 10^3$ and $\mu = 0.08$. The blue line is the approximate Fano form Eq. (215) and the orange dashed line is the exact function Eq. (205). When β_1 and β_2 are comparable this Fano form is obvious, but when $\beta_2 \gg \beta_1$ the Fano form reduces to an ordinary Lorentzian as seen in Fig. 23.

chosen in Fig. 23 but if we increase β_1 to be comparable to β_2 the Fano shape is obvious, as seen in Fig. 24. The frequency ω_{Fano} plays no direct role, but helps to define three important frequencies, those of the minimum, maximum and crossing points of the Fano function, which are given by

$$\omega_{\mathrm{min}} = \sqrt{\omega_{\mathrm{Fano}}^2 - \frac{\Gamma\zeta}{2}} = \sqrt{1 - \mu^2 - \frac{2\beta_2}{\beta_1 Q_\Gamma}}, \tag{219}$$

$$\omega_{\mathrm{max}} = \sqrt{\omega_{\mathrm{Fano}}^2 + \frac{\Gamma}{2\zeta}} = \sqrt{1 + \frac{2\beta_1}{\beta_2 Q_\Gamma}}, \tag{220}$$

and

$$\omega_{\mathrm{cross}} = \sqrt{\omega_{\mathrm{Fano}}^2 + \frac{\Gamma}{4}\left(\frac{1}{\zeta} - \zeta\right)} = \sqrt{1 - \frac{\mu^2}{2} + \frac{1}{Q_\Gamma}\left(\frac{\beta_1}{\beta_2} - \frac{\beta_2}{\beta_1}\right)}, \tag{221}$$

respectively. The parameter Γ is a measure of the width of the resonance, and contains a term inversely proportional to the mechanical quality factor as is expected. However it also contains a term proportional to μ^2 showing that the resonance peak gets wider with increased coupling. The parameter $\zeta = \beta_2/\beta_1$ is a measure of the asymmetry of the resonance and in the limit $\zeta \to \infty$ i.e. $\beta_2 \gg \beta_1$, the Fano form reduces to the simple Breit-Wigner (Lorentzian) expression

$$\delta i_{\mathrm{DC}}(\omega) \approx \frac{\mu^2}{\beta_2 \Gamma}\left[\frac{1}{(\omega^2 - 1)^2\left(\frac{2}{\Gamma}\right)^2 + 1}\right]. \tag{222}$$

This is a good approximation for our experimentally relevant parameters as can be seen from the Lorentzian shape of Fig. 23.

We thus see that the exact peak frequency is $\omega_{\max}$ which is not dependent on μ at all and is extremely close to the bare resonance frequency 1 for experimentally relevant parameters. We now realise that the plateau found numerically is actually not a true plateau but the slope of a resonant peak, which becomes flatter with increasing Q_Γ. The frequency increases as we get deeper into the plateau at higher currents, reaching $\omega_{\max}$ at its deepest point.

We can also now give an expression for the plateau width, given by

$$\delta i_{\mathrm{DC}}(\omega_{\max}) = \frac{\mu^2\beta_2^3}{(\beta_1^2+\beta_2^2)^2\Gamma} = \frac{\beta_2^3}{(\beta_1^2+\beta_2^2)^2}\left[\frac{\mu^2}{\frac{2\beta_1\beta_2\mu^2}{\beta_1^2+\beta_2^2}+\frac{4}{Q_\Gamma}}\right]. \tag{223}$$

For low μ the plateau width increases as μ^2 as

$$\delta i_{\mathrm{DC}}(\omega_{\max}) \approx \frac{\mu^2 Q_\Gamma \beta_2^3}{4(\beta_1^2+\beta_2^2)^2}, \tag{224}$$

while for large μ the width saturates at a value $\beta_2^2/2\beta_1(\beta_1^2+\beta_2^2)$. In reality μ generally cannot become too large before other effects begin to dominate, as we will see in a subsequent chapter when discussing the strong-coupling limit, so that Eq. (224) is a good approximation. We note that this plateau width is the full width of the plateau explored on the increasing current path rather than the much smaller section of the plateau found on the decreasing current path.

The area of the mechanically induced hysteresis loop can also be estimated. Looking at Fig. 21, it is clear that the area is dominated by a right-angled triangular region with height given by the max plateau width $\delta i_{\mathrm{DC}}(\omega_{\max})$ and a width given by the Ohmic voltage associated with this current jump $\delta i_{\mathrm{DC}}(\omega_{\max})/\beta_1$. This approximation is better with decreasing width of the resonance i.e. higher quality factor Q_Γ and low coupling. The area is thus approximated as

$$\text{Area} \approx \frac{\delta i_{\mathrm{DC}}(\omega_{\max})^2}{2\beta_1} = \frac{1}{2\beta_1}\left[\frac{\mu^2\beta_2^3}{(\beta_1^2+\beta_2^2)^2\Gamma}\right]^2, \tag{225}$$

and scales as μ^4 for low coupling. This area is expressed in units of $I_{\mathrm{c}}V_0 = \beta_1 I_{\mathrm{c}}^2 R$.

Now that we have the current as a function of ω we can find similar expressions for other important quantities. The parameter g appearing in our ansatz Eq. (168) was expressed in terms of ω and i_{DC} in Eq. (190). Inserting the exact expression

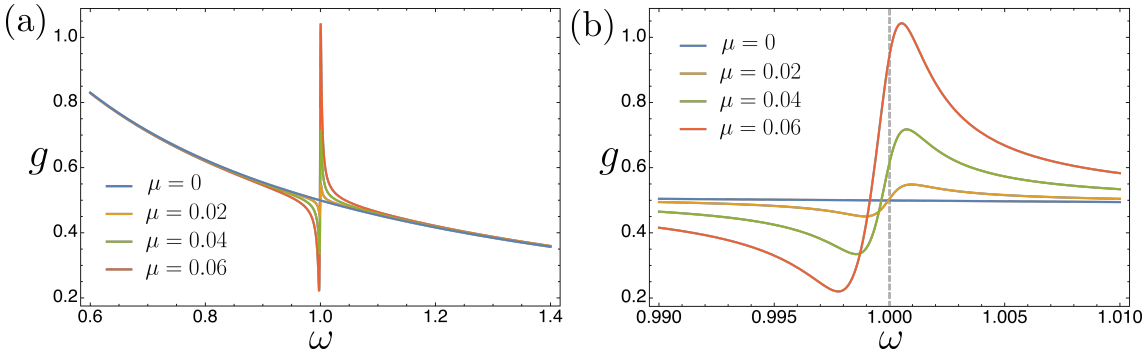

Figure 25: (a) The parameter g plotted as a function of voltage ω with various coupling values μ. (b) Zoom of the function close to the mechanical resonance frequency $\omega = 1$ showing a Fano-like resonance. g becomes fairly large for high coupling deep into the plateau at $\omega \approx 1$ indicating that our approximation $g/\omega \ll 1$ starts to break down.

for $i_{\mathrm{DC}}(\omega)$ in Eq. (202) we can express g in the form

$$g^2 = \frac{\kappa}{D_2} \approx \frac{1}{\beta_1^2 + \beta_2^2}\left[\frac{[1-(1+\mu^2)\omega^2]^2 + (2\omega/Q_\Gamma)^2}{(\omega^2 - \omega_{\mathrm{Fano}}^2)^2 + \left(\frac{\Gamma}{2}\right)^2}\right], \tag{226}$$

where κ and D_2 are functions of ω defined in Eqs. (176) and (209). The right hand expression is derived using the same approximation that led to the Fano form of $\delta i_{\mathrm{DC}}(\omega)$. g is plotted as a function of ω in Fig. 25 for various coupling values showing that once again a Fano-like resonance appears near $\omega = 1$. The peak of this resonance in g occurs at a higher frequency than ω_{max} but because the largest physical plateau solution occurs at ω_{max} the largest physical value of g is $g(\omega_{\mathrm{max}})$. In the limit $\beta_2 \gg \beta_1$ where $\omega_{\mathrm{max}} \approx 1$ this value is

$$g(1) \approx \frac{1}{\beta_2}\sqrt{1 + \left(\frac{\mu^2 Q_\Gamma}{2}\right)^2}. \tag{227}$$

We note that g can become comparable to 1 when $\mu^2 \approx 2(\beta_2^2 - 1)/Q_\Gamma$ which for our experimental parameters is $\mu \approx 0.06$. Since $\omega \approx 1$ in the region of interest, our approximation $g/\omega \ll 1$ breaks down and our analytics become quantitatively incorrect above this point. However we will see that we can still make qualitative predictions that are in good agreement with the numerical results.

The amplitude of the mechanical oscillations themselves can also now be calculated from Eq. (177). Inserting $g^2 = \kappa/D_2$ we obtain

$$A = -\frac{\mu\beta_2\omega}{\sqrt{D_2}}. \tag{228}$$

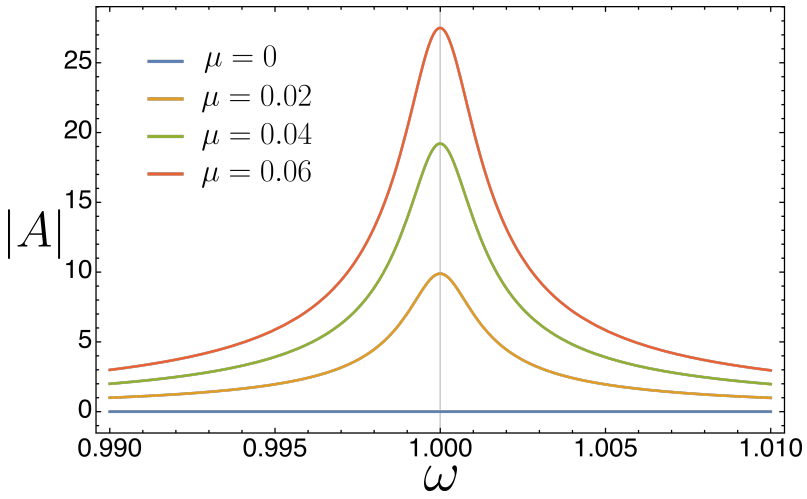

Figure 26: Mechanical oscillation amplitude $|A|$ plotted as a function of ω for various coupling values μ. The true resonance frequency of the coupled system is ω_{Fano} which differs only slightly from 1 for low coupling. The width of the resonance is given by Γ which depends on Q_Γ and increases with μ.

Using the same approximations that led to the Fano form of $\delta i_{\text{DC}}(\omega)$ i.e. expanding around $\omega^2 = 1$ with $\mu^2, 1/Q_\Gamma \ll 1$, we obtain the Lorentzian form

$$A \approx -\frac{\mu\beta_2}{\sqrt{\beta_1^2+\beta_2^2}} \frac{1}{\sqrt{(\omega^2-\omega_{\text{Fano}}^2)^2 + \left(\frac{\Gamma}{2}\right)^2}}. \tag{229}$$

The mechanical oscillation amplitude $|A|$ is plotted in Fig. 26[8]. We thus see that ω_{Fano}, which depends on μ according to Eq. (216), has a physical interpretation as the true mechanical resonance frequency of the coupled system.

The phase delay γ between the voltage and mechanical oscillation is calculated from the two equations

$$\sin\gamma = \frac{1-(1+\mu^2)\omega^2}{\sqrt{\kappa}}, \tag{230}$$

$$\cos\gamma = \frac{2\omega/Q_\Gamma}{\sqrt{\kappa}}, \tag{231}$$

derived previously, and is plotted as a function of ω in Fig. 27. For $\omega \ll 1$, $\gamma = \pi/2$, and for $\omega \gg 1$, $\gamma = -\pi/2$ with the crossover occurring in a region of width $1/Q_\Gamma$ around the central frequency $\omega = 1/\sqrt{1+\mu^2}$.

[8]We have plotted $|A|$ since A is negative because of the phase convention chosen for γ.

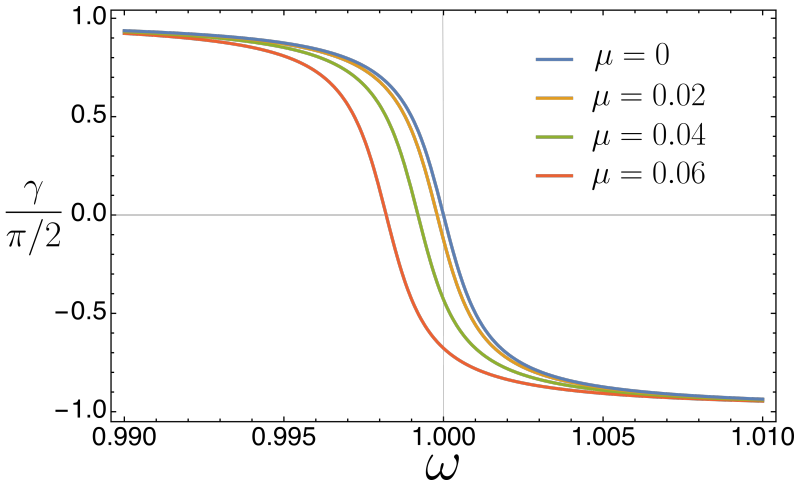

Figure 27: The phase delay γ between the voltage and mechanical oscillations plotted as a function of ω for various coupling values μ, calculated from Eqs. (174) and (175). For $\omega \ll 1$, $\gamma = \pi/2$, and for $\omega \gg 1$, $\gamma = -\pi/2$ with the crossover occurring in a region of width $1/Q_\Gamma$ around the central frequency $\omega = 1/\sqrt{1+\mu^2}$.

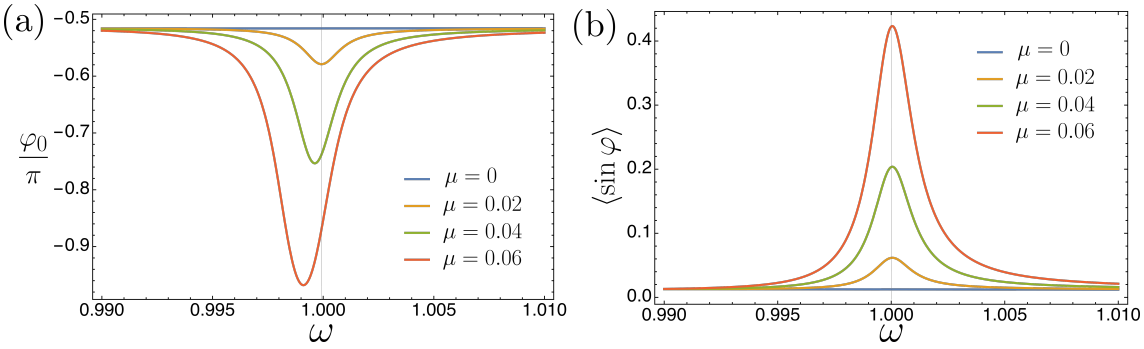

Figure 28: (a) The phase φ_0 plotted as a function of ω for various coupling values μ, calculated from Eqs. (232) and (233). Away from the resonance $\varphi_0 \approx -\pi/2$, but on resonance it is shifted from this value. A physical interpretation of φ_0 comes from the fact that the average supercurrent is given by $\langle \sin\varphi \rangle = -(g/2\omega)\cos\varphi_0$. This is plotted in (b) showing that the shift of φ_0 at resonance causes the supercurrent to acquire a finite DC component.

Finally the phase φ_0 is calculated from Eqs. (197) and (198) i.e.

$$\sin\varphi_0 = \mu A\omega^2 \sin\gamma - \beta_2 g\omega, \tag{232}$$

$$\cos\varphi_0 = \mu A\omega^2 \cos\gamma - \beta_1 g, \tag{233}$$

after the insertion of the expressions for A, γ and g given above. The phase φ_0 is plotted as a function of ω in Fig. 28(a). A physical interpretation of φ_0 comes from the fact that the average supercurrent is given by $\langle\sin\varphi\rangle = -(g/2\omega)\cos\varphi_0$, which is plotted in Fig. 28(b). We see that off resonance we have $\varphi_0 \approx -\pi/2$ and thus the average supercurrent is zero, but on resonance φ_0 is shifted so that the supercurrent acquires a finite DC component. A more useful expression for this supercurrent average is obtained by taking the time average of our equation of motion Eq. (140), yielding

$$\langle\sin\varphi\rangle = -(g/2\omega)\cos\varphi_0 = i_{\rm DC} - \beta_1\omega, \tag{234}$$

which was found earlier in Eq. (196). This has a simple interpretation, the more the voltage ω differs from the ideal Ohmic value $i_{\rm DC}/\beta_1$, the greater the supercurrent's DC average. This DC average thus becomes very large on the Shapiro plateau.

From all these parameters we see that there are a number of important frequencies in this complicated coupled problem. As we increase ω towards the mechanical resonance, first the phase delay γ becomes zero at $1/\sqrt{1+\mu^2}$, then the oscillation amplitude $|A|$ has a maximum at $\omega_{\rm Fano}$ then finally the plateau $\delta i_{\rm DC}(\omega)$ reaches its maximum at $\omega_{\rm max}$. These are all distinct frequencies, different from the bare resonance frequency $\omega = 1$, with $1/\sqrt{1+\mu^2} < \omega_{\rm Fano} < 1$ and $\omega_{\rm max} > 1$.

We thus have a good analytical theory that can explain the Shapiro-like steps that were seen in the numerical analysis, as well as the mechanically induced hysteresis that results in different I-V curves being obtained on the decreasing and increasing current paths. We now move on to explore new phenomena that occur as μ continues to increase.

4.8 Strong-Coupling Limit

In the previous section we numerically calculated the I-V curves of the coupled system for both decreasing and increasing current paths, shown in Figs. 17 and 19 respectively. The width of the resulting mechanically induced Shapiro plateau is predicted to increase with μ according to our analytically derived expression Eq. (223). This agrees well with the numerical analysis when μ is not too large but fails when μ exceeds some critical value, as we will now see.

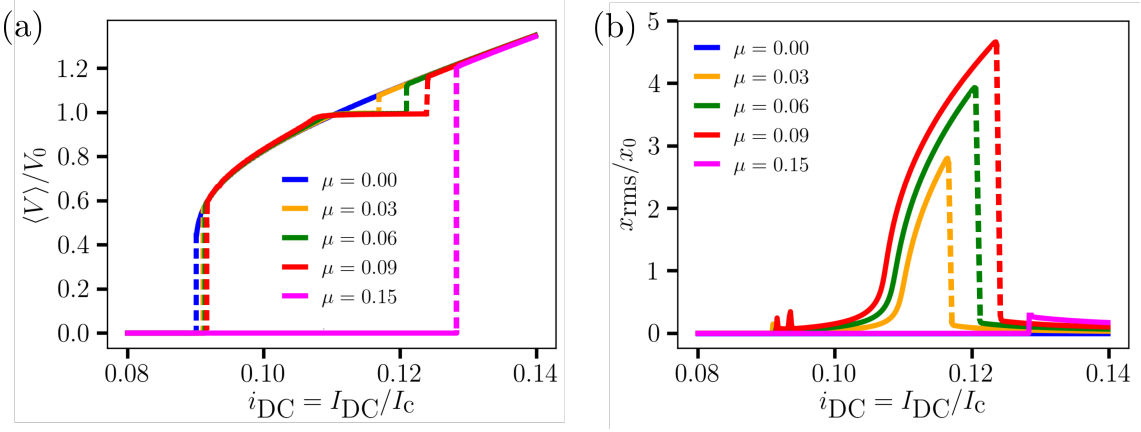

Figure 29: (a) DC voltage $\langle V\rangle$ and (b) root mean square mechanical oscillation $x_{\text{rms}} = \sqrt{\langle x^2\rangle}$ as functions of the applied current $i_{\text{DC}} = I_{\text{DC}}/I_{\text{c}}$ for a simple decreasing current experiment, obtained by numerically solving Eqs. (140) and (141) with $\beta_1 = 0.1$, $\beta_2 = 2$, $Q_\Gamma = 10^3$. Results are shown for five different magnetic field coupling values $\mu = B/B_0$. The results for $\mu = 0.15$ show that instead of forming the Shapiro plateau, the system instead abruptly retraps to the zero voltage state prematurely. This retrapping occurs for all coupling values μ above a critical value, and will be shown in the next section to be a result of energy being transferred from the electronic subsystem to the mechanical one.

4.8.1 Mechanically Induced Retrapping

Starting again with the simple decreasing current path, the numerically calculated I-V characteristics displayed in Fig. 29 show that for $\mu = 0.15$ the system abruptly retraps to the zero voltage state instead of forming the Shapiro plateau. This occurs at the current value at which we would expect the Shapiro plateau to start. The time evolution of the system at this point is plotted in Fig. 30. After a long transient the oscillations $a(\tau)$ increase and it seems that the system is going to enter the phase locked Shapiro state, but instead the oscillations increase too rapidly and cannot be maintained; the system is abruptly retrapped into the zero voltage state. The supercurrent frequency rapidly goes to zero and oscillations decay. Soon we will see that the analytics allow us to interpret this as due to the mechanical oscillations subtracting too much energy away from the electronic system.

Having looked at I-V characteristics for some specific values of μ we can now look at a colour plot showing how the Shapiro plateau develops as a continuous function of μ. Such a colour plot is given in Fig. 31(a), displaying the average voltage $\langle V\rangle$ as a function of both i_{DC} and μ when traversing the decreasing current path. The coloured lines correspond to the specific values of μ shown in Fig. 29. The white region in this plot corresponds to the Shapiro plateau which widens as μ increases, until we reach a critical value that we call μ_{c2}. For coupling μ above this value, the

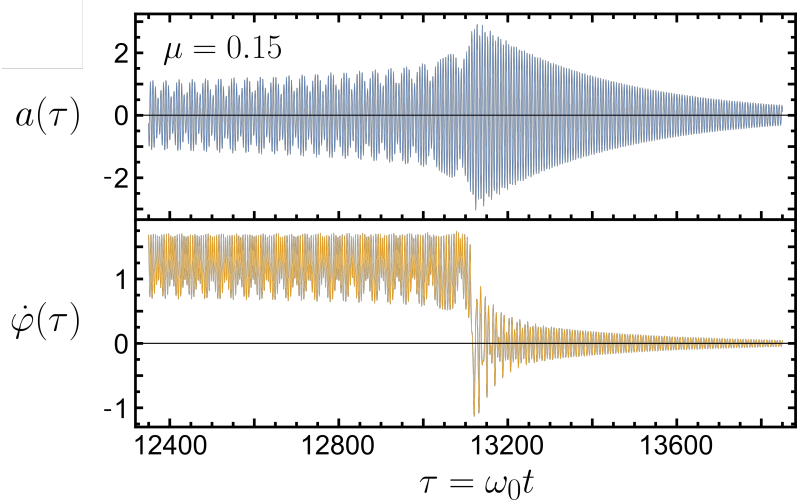

Figure 30: Time evolution $a(\tau)$ and $\dot{\varphi}(\tau)$ for the solution to Eqs. (140) and (141) when $\mu = 0.15$ and at the current value $i_{\rm DC} = 0.128$. After a long transient the oscillations $a(\tau)$ increase and it seems that the system is going to enter the phase locked Shapiro state, but instead the oscillations increase too rapidly and cannot be maintained; the system is abruptly retrapped into the zero voltage state. The supercurrent frequency rapidly goes to zero and oscillations decay.

system instead retraps to zero voltage instead of forming the plateau, as has already been seen in the specific case $\mu = 0.15$ in Fig. 29. This amounts to an increase in the retrapping current by up to 50% and should be easily detectable in state of the art experiments. An accompanying plot of the root mean square displacement $x_{\rm rms}$ is seen in Fig. 31(b) which shows that the plateau region is characterized by strong mechanical oscillations which grow with increasing current and magnetic field.

A natural question is whether this retrapping phenomenon occurs also on the more complicated increasing current path. We recall that this path involves decreasing the current to reach the plateau, and then increasing the current again exploiting the mechanically induced hysteresis. Obviously we must have $\mu < \mu_{\rm c2}$ or we would not be able to reach the plateau initially. The I-V characteristics for this increasing path are shown in Fig. 32(a). The plot for $\mu = 0.09$ shows that the system is locked to the Shapiro plateau for a small range of currents before becoming unstable and retrapping in a similar way to the decreasing current case. There must be a lower critical value $\mu_{\rm c1} < \mu_{\rm c2}$ at which this phenomenon first occurs.

Once again a colour plot is displayed in Fig. 33(a) showing $\langle V \rangle$ as a function of $i_{\rm DC}$ and μ, this time on the increasing current path. The full extent of the Shapiro plateau is visible as the white region whose width grows approximately quadratically with μ as expected from the analytical expression Eq. (223). Below a critical coupling value $\mu_{\rm c1}$, as we increase the current we explore the entire width

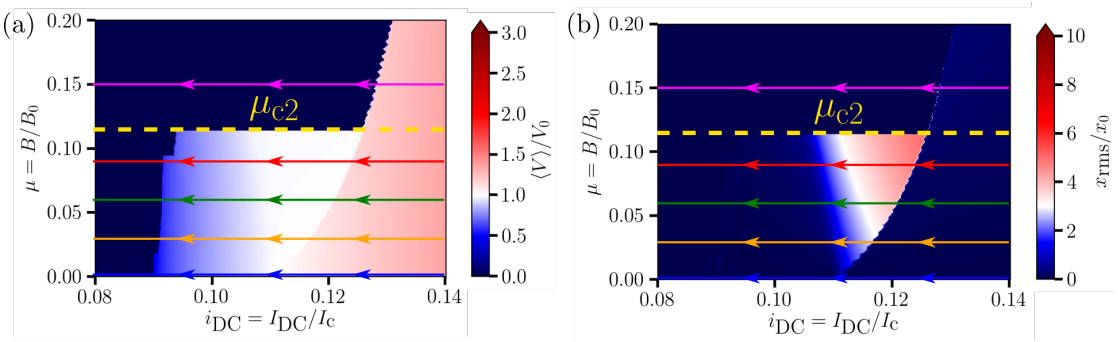

Figure 31: (a) DC voltage $\langle V \rangle$ and (b) root mean square mechanical oscillation $x_{\text{rms}} = \sqrt{\langle x^2 \rangle}$ as functions of the applied current I_{DC} and magnetic field B, obtained by numerically solving Eqs. (140) and (141) with experimentally relevant parameters $\beta_1 = 0.1, \beta_2 = 2, Q_\Gamma = 10^3$, for the decreasing current path. The white region in panel (a) shows the Shapiro plateau $\langle V \rangle \approx V_0$ which widens as μ increases, until a critical value μ_{c2} above which the plateau becomes unstable and instead the system retraps to zero voltage prematurely. The coloured lines refer to the specific values of μ plotted in Fig. 29.

of the plateau at which point the voltage increases to the Ohmic solution. However above this critical value we only explore a small section of the plateau before the system is retrapped. Again a plot of the root mean square displacement x_{rms} is seen in Fig. 33(b). One should compare these two colour plots to the ones for the decreasing current path in Fig. 31. We notice that by exploiting the hysteresis we can obtain a plateau width of approximately $0.4I_c$ compared to just $0.01I_c$ with the decreasing current. Similarly, we can obtain mechanical oscillations that are up to three times stronger. Clearly this increasing current path obtained by exploiting the mechanically induced hysteresis represents a significant experimental advantage.

A comparison between the numerically calculated plateau width and the analytical one Eq. (223) is shown in Fig. 34, showing good agreement for low μ as they both grow as μ^2 but beginning to differ as we approach μ_{c1}. We believe this slight discrepancy to be due to our approximation $g/\omega \ll 1$ failing as we get deeper into the plateau where the mechanical oscillations are very strong.

4.8.2 Fixed Current, Varying Magnetic Field

We have so far considered two simple possible experiments that both involve keeping the magnetic field fixed while varying the current. However due to the non-linearity of our system, and thus its strong dependence on initial conditions, there are an infinite number of possible paths that can be taken in the space i_{DC}, μ that will yield different results. Most of these are of course far too complex to be experimentally practical, but there is one additional simple one that we have not yet considered.

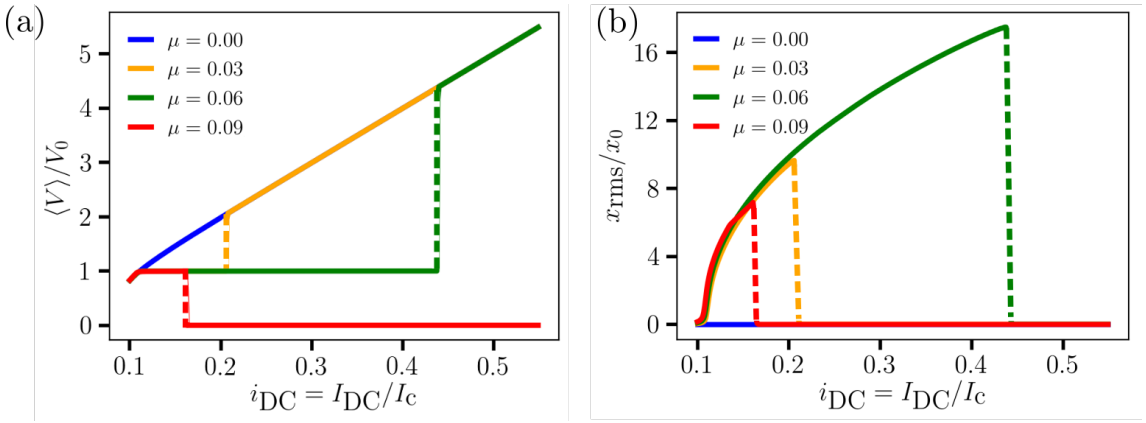

Figure 32: (a) DC voltage $\langle V \rangle$ and (b) root mean square mechanical oscillation $x_{\mathrm{rms}} = \sqrt{\langle x^2 \rangle}$ as functions of the applied current $i_{\mathrm{DC}} = I_{\mathrm{DC}}/I_{\mathrm{c}}$ for the increasing current path described in the main text, obtained by numerically solving Eqs. (140) and (141) with $\beta_1 = 0.1$, $\beta_2 = 2$, $Q_\Gamma = 10^3$. Results are shown for four different magnetic field coupling values $\mu = B/B_0$. Similarly to the decreasing current case, a portion of the Shapiro plateau becomes unstable when the coupling μ becomes too large. In this case, the line at $\mu = 0.09$ shows that the system abruptly retraps to zero after exploring only a fraction of the whole plateau.

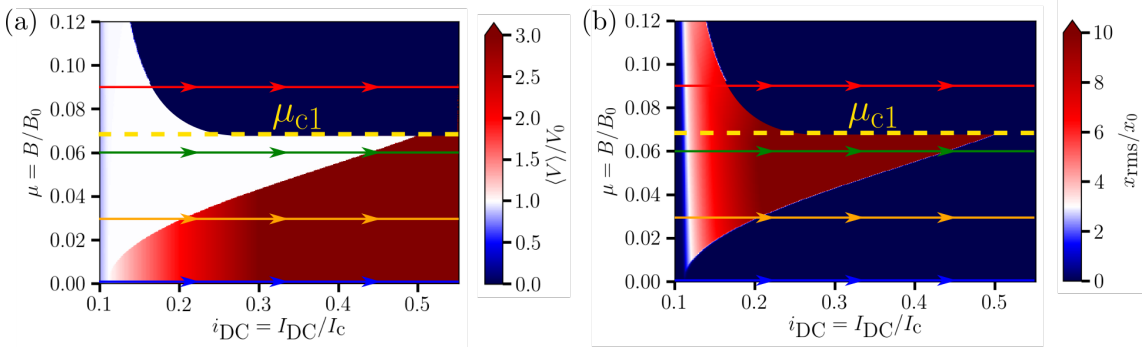

Figure 33: (a) DC voltage $\langle V \rangle$ and (b) root mean square mechanical oscillation $x_{\mathrm{rms}} = \sqrt{\langle x^2 \rangle}$ as functions of the applied current I_{DC} and magnetic field B, obtained by numerically solving Eqs. (140) and (141) with experimentally relevant parameters $\beta_1 = 0.1, \beta_2 = 2, Q_\Gamma = 10^3$, for the increasing current path. The white region in panel (a) shows the Shapiro plateau $\langle V \rangle \approx V_0$ which widens as μ increases, until a critical value μ_{c1} above which a large portion of the plateau becomes unstable and the system instead retraps to zero in a similar way to the decreasing current path. The coloured lines refer to the specific values of μ plotted in Fig. 32.

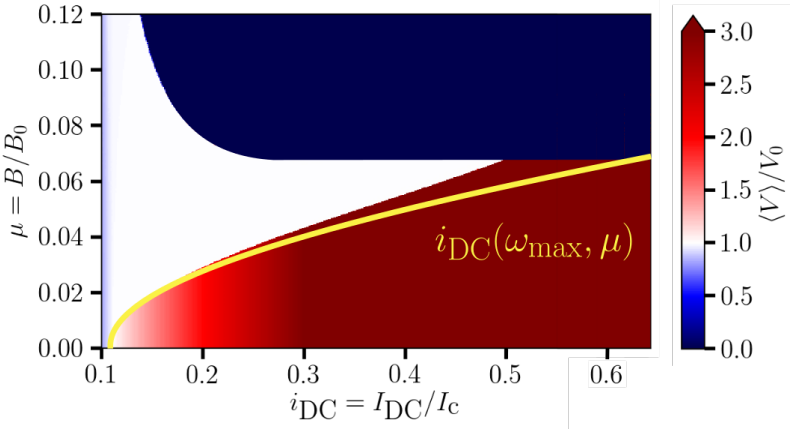

Figure 34: Shape of the Shapiro plateau region calculated numerically compared to the shape predicted by the analytics (yellow line). The edge of the plateau is given by the current at the local maximum point $\omega_{\rm max}$. The plateau edge is thus predicted analytically to be $i_{\rm DC}(\omega_{\rm max}, \mu) = i^{(0)}_{\rm DC}(\omega_{\rm max}) + \delta i_{\rm DC}(\omega_{\rm max}, \mu)$, where the μ dependent part is given by Eq. (223), growing as μ^2 for low μ.

Instead of fixing the magnetic field and varying the current we do the opposite and fix the current while varying the magnetic field. To obtain non-trivial results we of course must be in a finite voltage regime to start with or else the system will just remain in the trapped zero voltage state with a DC supercurrent and no mechanical oscillations. The process then involves decreasing the current from above $I_{\rm c}$ down to a current near the resonant region $\langle V \rangle \sim V_0$ and then keeping the current fixed while increasing μ from zero.

We have simulated this experiment numerically over a wide range of starting currents, with the results being shown in Fig. 35. Panel (a) shows the DC voltage as a function of $i_{\rm DC}$ and μ. We see that as μ increases the voltage becomes pinned to the plateau value V_0 over a wide range of currents. This constant current procedure thus maps all the plateau states explored by the decreasing current path at constant μ (cf. Fig. 31) but also accesses additional states, as the sharp boundary at $\mu_{\rm c2}$ extends into a funnel-like feature. The system eventually retraps as the coupling is increased too much, occurring at a different μ for each current value. At a third critical coupling value $\mu_{\rm c3} > \mu_{\rm c2}$, the plateau becomes unstable for all current values. Fig. 35(b) shows the corresponding colour plot of the root mean square displacement, while panels (c) and (d) show the result for specific current values corresponding to the coloured lines in panels (a) and (b) respectively.

We thus have seen three different possible experiments that can be carried out on this coupled system, each associated with its own critical coupling value. For the decreasing current experiment, the plateau becomes unstable at $\mu_{\rm c2}$. For the increasing current experiment, the plateau becomes unstable at $\mu_{\rm c1}$. Finally for the

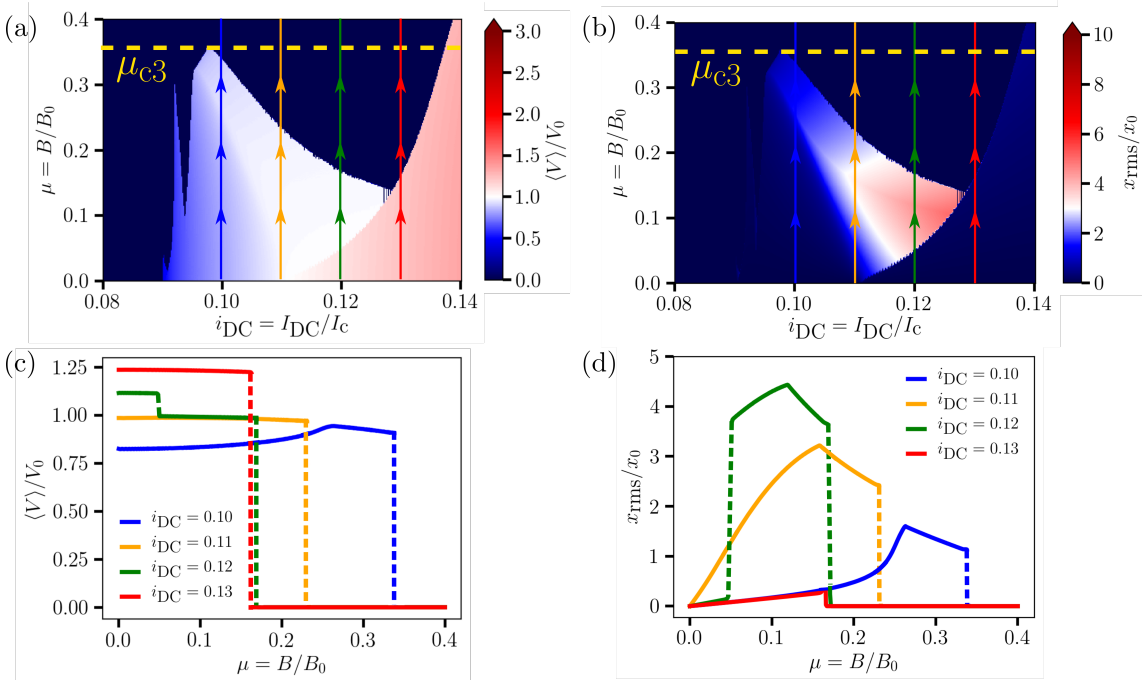

Figure 35: (a) DC voltage $\langle V\rangle$ and (b) root mean square mechanical oscillation $x_{\rm rms} = \sqrt{\langle x^2\rangle}$ as functions of the applied current $I_{\rm DC}$ and magnetic field B, obtained by numerically solving Eqs. (140) and (141) with experimentally relevant parameters $\beta_1 = 0.1, \beta_2 = 2, Q_\Gamma = 10^3$, for the fixed current, increasing magnetic field path. This constant current procedure thus maps all the plateau states explored by the decreasing current path at constant μ (see Fig. 31) but also accesses additional states, as the sharp boundary at μ_{c2} extends into a funnel-like feature. At μ_{c3}, the plateau becomes unstable for all current values. (c) DC voltage $\langle V\rangle$ and (d) root mean square mechanical oscillation $x_{\rm rms} = \sqrt{\langle x^2\rangle}$ for specific current values corresponding to the coloured lines in panels (a) and (b).

increasing magnetic field experiment, the plateau becomes fully unstable at μ_{c3}. The results for all three of these experiments are collected for convenience together in Fig. 36. We now carry out an analytical treatment based on an energy argument to understand why the plateau becomes unstable leading to these sudden retrappings. This will lead to analytical expressions for the dependence of μ_{c1}, μ_{c2} and μ_{c3} on the system parameters.

4.9 Analytical Explanation of Retrapping

In section 4.7 we derived a number of important parameters as functions of voltage ω, but we have not yet considered the various energy contributions in the system. Recall that the total energy of the system is given by

$$\bar{E} = \frac{1}{2}\beta_2 \left(\dot{\varphi} + \frac{\mu}{\beta_2}\dot{a}\right)^2 - \cos\varphi + \frac{1}{2\beta_2}\left(\dot{a}^2 + (a + i_{\mathrm{DC}}\mu)^2\right), \tag{235}$$

which is given in units of the Josephson energy $E_{\mathrm{J}} = \hbar I_{\mathrm{c}}/2e$ and may be split up into three contributions $\bar{E} = \bar{E}_{\varphi} + \bar{E}_{\mathrm{m}} + \bar{E}_{\mathrm{c}}$, where the electronic energy is

$$\bar{E}_{\varphi} = \frac{1}{2}\beta_2\dot{\varphi}^2 - \cos\varphi, \tag{236}$$

the mechanical energy is

$$\bar{E}_{\mathrm{m}} = \frac{1}{2\beta_2}\left((1+\mu^2)\dot{a}^2 + (a + i_{\mathrm{DC}}\mu)^2\right), \tag{237}$$

and the coupling energy is

$$\bar{E}_{\mathrm{c}} = \mu\dot{a}\dot{\varphi}. \tag{238}$$

These are in general time dependent quantities, but inserting our ansatz Eqs. (168) and (170) we can obtain expressions for their time averages as functions of ω

$$\langle\bar{E}_{\varphi}\rangle = \frac{1}{2}\beta_2(\omega^2 + \frac{g^2}{2}) - \frac{g}{2\omega}\sin\varphi_0, \tag{239}$$

$$\langle\bar{E}_{\mathrm{m}}\rangle = \frac{i_{\mathrm{DC}}(\omega)^2\mu^2}{2\beta_2} + \frac{A^2}{4\beta_2}(\omega^2+1), \tag{240}$$

$$\langle\bar{E}_{\mathrm{c}}\rangle = -\frac{\mu A\omega g}{2}\sin\gamma. \tag{241}$$

The mechanical energy is positive definite and strongly peaked at the resonance, as we would expect. While the mechanical energy can be extremely large, the coupling energy is a rather small contribution and not particularly significant. The electronic

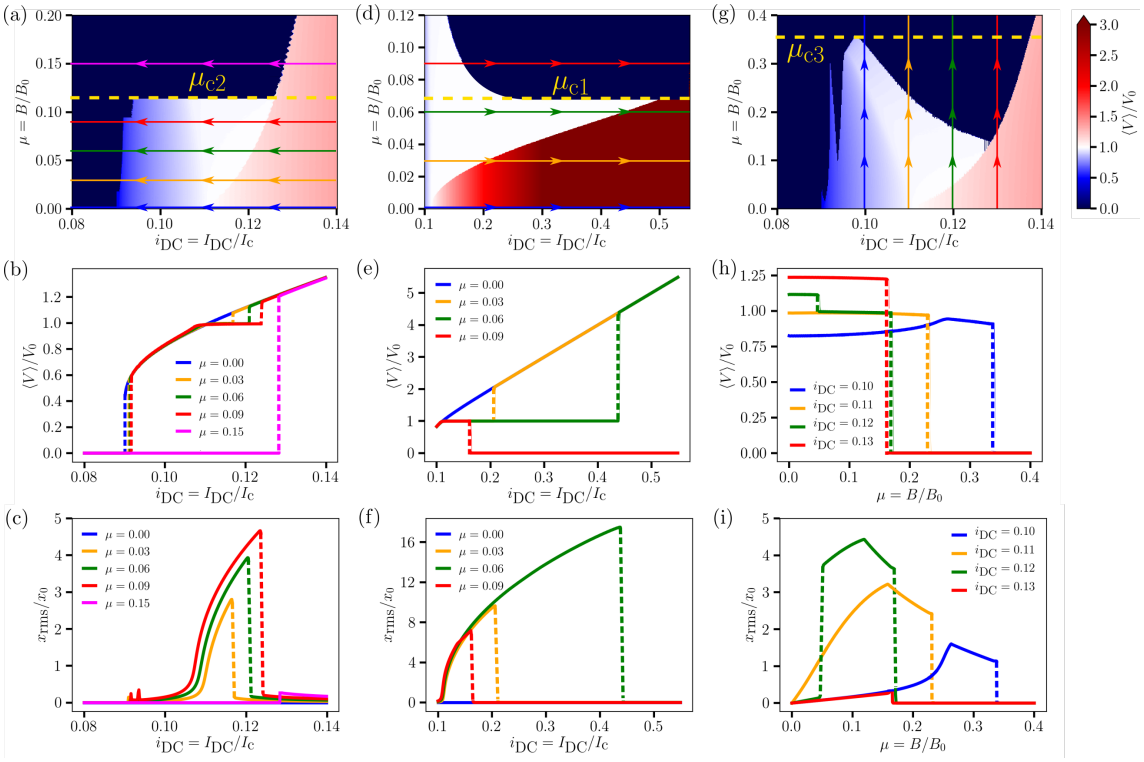

Figure 36: DC voltage $\langle V \rangle$ and root mean square mechanical oscillation $x_{\mathrm{rms}} = \sqrt{\langle x^2 \rangle}$ as functions of the applied current I_{DC} and magnetic field B, obtained by numerically solving Eqs. (140) and (141) with experimentally relevant parameters $\beta_1 = 0.1, \beta_2 = 2, Q_\Gamma = 10^3$. Typical parameter scales are $I_c = 10\mathrm{nA}$, $B_0 = 10\mathrm{T}$ and $V_0 = 0.3\mu\mathrm{V}$ (a) DC voltage measured along the decreasing current path for a range of coupling values. (b) I-V characteristics for specific values of coupling ($\mu = 0, 0.03, 0.06, 0.09, 0.15$) corresponding to the cuts in (a). A plateau at $\langle V \rangle = V_0$ develops for low coupling $\mu < \mu_{c2}$ which becomes unstable when $\mu > \mu_{c2}$. (c) Plot of x_{rms} for the same cuts as (b) showing that mechanical oscillations are amplified on the voltage plateau, growing stronger at higher currents. (d) DC voltage measured when increasing the current from the plateau, for a range of coupling values. (e) I-V characteristics for specific values of coupling ($\mu = 0, 0.03, 0.06, 0.09$) corresponding to the cuts in (d). The plateau here starts to become unstable above a critical value μ_{c1}. (f) Plot of x_{rms} for the same cuts as (e). On this increasing path we can reach higher currents deeper into the plateau, leading to stronger mechanical oscillations. (g) DC voltage measured when increasing magnetic field at fixed bias current. (h) DC voltage against coupling μ for specific bias current values ($i_{\mathrm{DC}} = 0.1, 0.11, 0.12, 0.13$) corresponding to the cuts in (g). As the coupling is increased, voltage values begin to lock to the resonant value V_0 as the Shapiro-like plateau widens, but eventually retrap to the zero voltage state as the plateau becomes unstable. Above μ_{c3}, the plateau becomes unstable for all current values. (i) Plot of x_{rms} for the same cuts as (h).

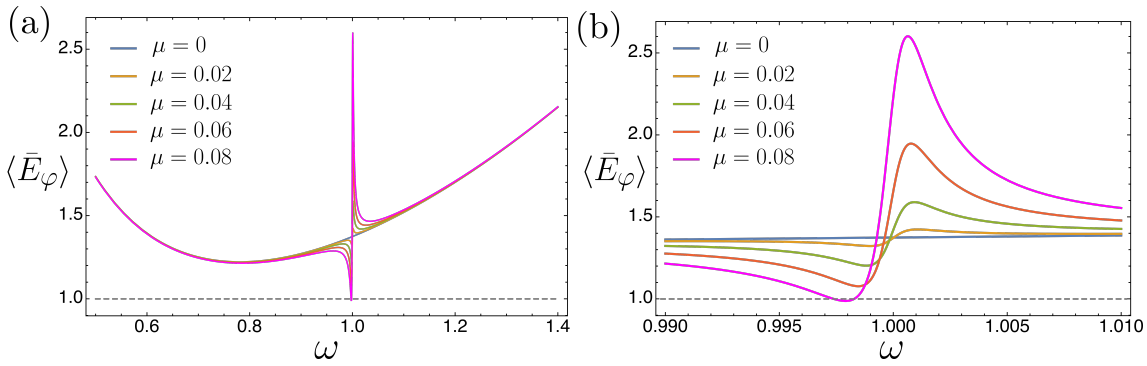

Figure 37: (a) Average electronic energy $\langle \bar{E}_\varphi \rangle$ plotted over a wide range of voltage values ω. (b) Zoom around the resonance value $\omega = 1$ showing that on the physical portion of the curve with $\omega < 1$, the electronic energy is on average reduced by the mechanical oscillations. The plot for $\mu = 0.08$ shows that when μ becomes too large $\langle \bar{E}_\varphi \rangle$ can drop below 1 in a range of ω values.

energy displays a much more interesting dependence on ω. Inserting g and $\sin\varphi_0$ from Eq. (226) and (232) we can write $\langle \bar{E}_\varphi \rangle$ explicitly in terms of ω as

$$\langle \bar{E}_\varphi \rangle = \frac{\beta_2}{2}\left[\omega^2 + \frac{3\kappa}{2D_2} + \frac{\mu^2\omega^2}{D_2}\left(1 - (1+\mu^2)\omega^2\right)\right]. \tag{242}$$

This is plotted as a function of ω in Fig. 37, which shows that the coupling again induces a Fano-like resonance in $\langle \bar{E}_\varphi \rangle$ close to the resonance frequency. It is important to notice that on the physical portion of this resonance with $\omega < 1$, the electronic energy is substantially reduced by the mechanical oscillations (recall that the right side of the resonance region with $\omega > 1$ is regarded as unphysical as $\partial i_{\mathrm{DC}}/\partial\omega < 0$). This reduction becomes more significant the stronger the coupling is. The lower average energy the electronic system has, the harder it is to remain in the running state with a finite voltage. In terms of the washboard analogy, the particle's kinetic energy is reduced so that it only just makes it over the maxima of the potential $-\cos\varphi$. In fact, when μ becomes too large the average electronic energy can drop below the potential maximum i.e. $\langle \bar{E}_\varphi \rangle < 1$, as shown by the curve $\mu = 0.08$ in Fig. 37. We find this to be a very good condition for predicting when the system becomes unstable, providing an analytical understanding for the various sudden retrappings observed in the numerical analysis. The coupling value at which $\langle \bar{E}_\varphi \rangle$ first goes below 1 is thus identified with the first critical value μ_{c1}.

4.9.1 First Critical Coupling, μ_{c1}

In Fig. 38 we explain the transition that happens as μ exceeds μ_{c1}. In panel (a) we see a sketch of the function $i_{\mathrm{DC}}(\omega)$ when $\mu < \mu_{\mathrm{c1}}$, with the blue and green

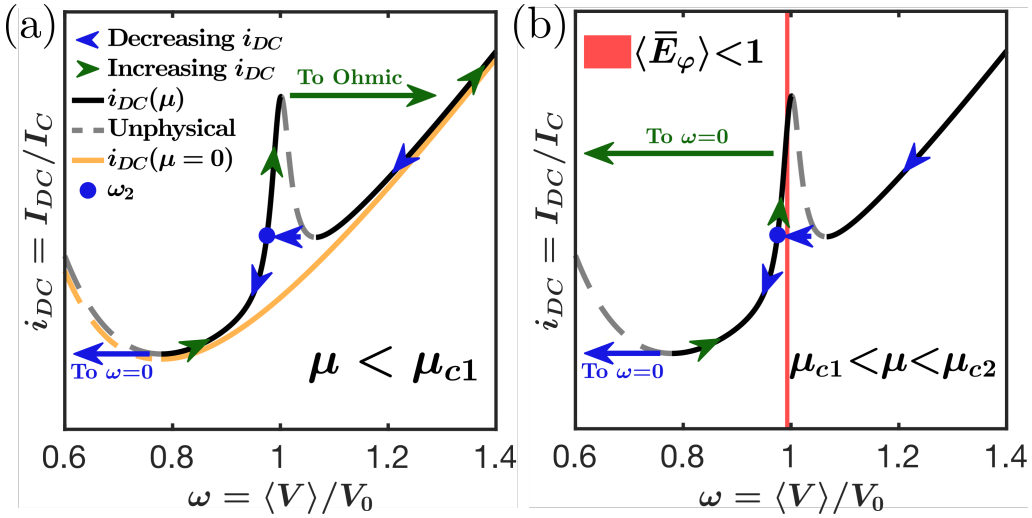

Figure 38: Sketch of $i_{\rm DC}(\omega)$ for (a) $\mu < \mu_{\rm c1}$ showing the usual decreasing and increasing current paths, and (b) for $\mu > \mu_{\rm c1}$ showing the emergence of the 'forbidden region' $\langle \bar{E}_\varphi \rangle < 1$. When this region is entered on the increasing current path the system retraps to $\omega = 0$ explaining the sudden retrapping observed numerically in Fig. 36(d).

arrows showing the states explored by the decreasing and increasing current paths respectively. The decreasing path reaches the end of the Ohmic branch and then the voltage falls to a value ω_2 near the bottom of the resonant peak. The increasing path reaches the top of the resonant peak and then there is a jump to the Ohmic solution. In contrast, panel (b) shows the case $\mu > \mu_{\rm c1}$ where over a region of ω values we have the so-called 'forbidden region' $\langle \bar{E}_\varphi \rangle < 1$, highlighted as a thin red strip. On the increasing current path, the system enters this region and subsequently retraps to $\omega = 0$, explaining the transition seen numerically in Fig. 36(d). Notice that this transition to $\omega = 0$ occurs somewhere in the middle of the peak rather than at its maximum point, explaining the instantaneous reduction of the observed plateau width when μ crosses $\mu_{\rm c1}$. As μ continues to increase, the observed plateau width continues to decrease as more and more states become unstable.

The region $\langle \bar{E}_\varphi \rangle < 1$ is plotted as a function of ω and μ in Fig. 39. Our expression Eq. (242) allows us to solve for the contour $\langle \bar{E}_\varphi \rangle = 1$ and thus the minimum point $\mu_{\rm c1}$. Multiplying $\langle \bar{E}_\varphi \rangle = 1$ by $2D_2/\beta_2$ we obtain an equation for the contour as

$$\left(\omega^2 - \frac{2}{\beta_2}\right) D_2 + \frac{3}{2}\kappa + \mu^2\omega^2 \left(1 - (1+\mu^2)\omega^2\right) = 0. \tag{243}$$

Inserting the expressions for κ and D_2 from Eqs. (176) and (209), we notice that μ appears in Eq. (243) only as μ^2 or μ^4 and thus we can express it as a quadratic

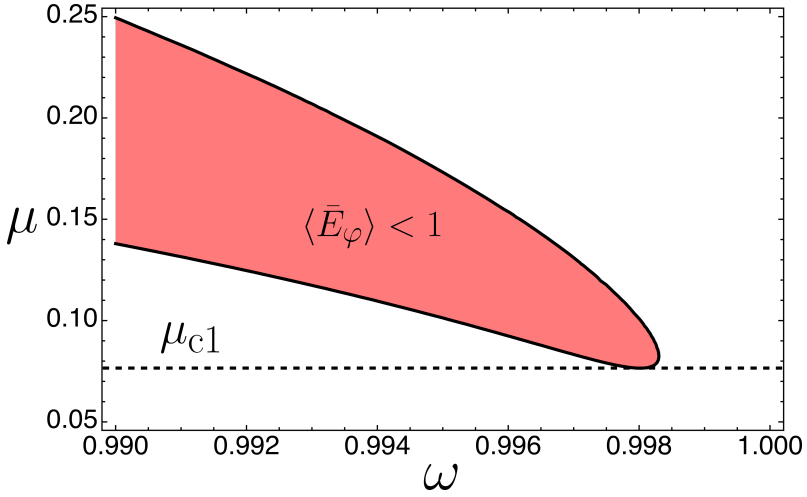

Figure 39: The region $\langle \bar{E}_\varphi \rangle < 1$ plotted as a function of ω and μ. The contour $\langle \bar{E}_\varphi \rangle = 1$ is found from the two real solutions to Eq. (244). When the system crosses into this region, it retraps to $\omega = 0$, the lowest value of μ at which this can occur is μ_{c1}.

polynomial equation in μ^2.

$$\mathbb{A}\mu^4 + \mathbb{B}\mu^2 + \mathbb{C} = 0, \tag{244}$$

where

$$\frac{\mathbb{A}}{\omega^4} = \beta_1^2 \left(\omega^2 - \frac{2}{\beta_2} \right) + \frac{1}{2}, \tag{245}$$

$$\frac{\mathbb{B}}{2\omega^2} = \left(\omega^2 - \frac{2}{\beta_2} \right) \left[\beta_1^2 (\omega^2 - 1) + \frac{2\beta_1\beta_2}{Q_\Gamma} \omega^2 \right] + \omega^2 - 1, \tag{246}$$

$$\mathbb{C} = \left[\left(\omega^2 - \frac{2}{\beta_2} \right) (\beta_1^2 + \beta_2^2 \omega^2) + \frac{3}{2} \right] \left[(\omega^2 - 1)^2 + \left(\frac{2\omega}{Q_\Gamma} \right)^2 \right]. \tag{247}$$

The two positive solutions to this biquadratic equation thus give an analytic form for the upper and lower bounds of the region $\langle \bar{E}_\varphi \rangle < 1$ shown in Fig. 39.

Unfortunately it is not easy to find μ_{c1} the minimum value of μ with respect to ω since Eq. (244) contains powers of ω up to eighth order. However, since the minimum occurs very close to $\omega = 1$ we can perform our now familiar expansion $\omega^2 \to 1 + \epsilon\delta\omega^2, 1/Q_\Gamma \to \epsilon/Q_\Gamma, \mu^2 \to \epsilon\mu^2$, to approximate the contour. Eq. (244) then reduces to

$$\tilde{\mathbb{A}}\mu^4 + \tilde{\mathbb{B}}\mu^2 + \tilde{\mathbb{C}} = 0, \tag{248}$$

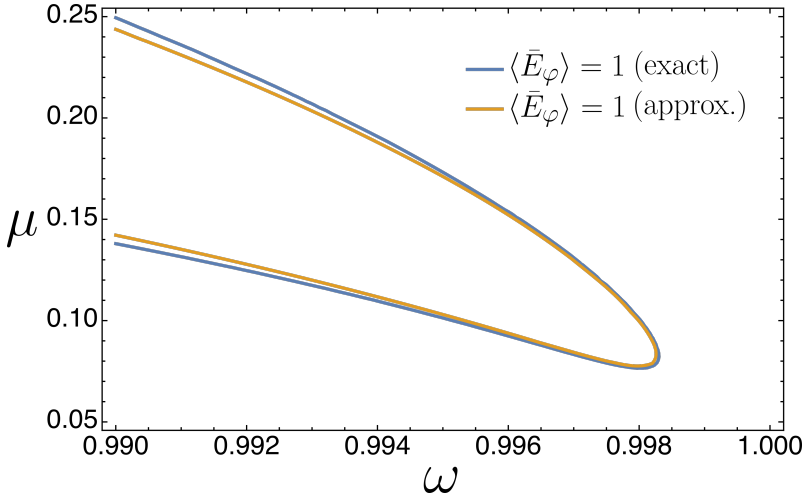

Figure 40: Comparison between the exact contour $\langle \bar{E}_\varphi \rangle = 1$ calculated from Eq. (244) and its approximation, calculated from Eq. (248). These are plotted with our experimentally relevant parameters $\beta_1 = 0.1, \beta_2 = 2, Q_\Gamma = 10^3$ for which we see that the approximation is very good, leaving the minimum point μ_{c1} basically unchanged.

where

$$\tilde{\mathbb{A}} = \beta_1^2 \left(1 - \frac{2}{\beta_2}\right) + \frac{1}{2} = \mathbb{A}_0, \tag{249}$$

$$\tilde{\mathbb{B}} = 2\left(1 - \frac{2}{\beta_2}\right)\left[\beta_1^2(\omega^2 - 1) + \frac{2\beta_1\beta_2}{Q_\Gamma}\right] + 2(\omega^2 - 1) = \mathbb{B}_0 + \mathbb{B}_1(\omega^2 - 1), \tag{250}$$

$$\tilde{\mathbb{C}} = \left[\left(1 - \frac{2}{\beta_2}\right)(\beta_1^2 + \beta_2^2) + \frac{3}{2}\right]\left[(\omega^2 - 1)^2 + \left(\frac{2}{Q_\Gamma}\right)^2\right] = \mathbb{C}_0 + \mathbb{C}_2(\omega^2 - 1)^2. \tag{251}$$

Here we have also defined coefficients $\mathbb{A}_n, \mathbb{B}_n, \mathbb{C}_n$ by grouping up powers of $(\omega^2 - 1)$ for future use. This approximate contour is compared to the exact one in Fig. 40 showing a very good agreement, especially at the minimum point that defines μ_{c1}. In employing this approximation we have removed many powers of ω so that our contour equation (248) can now be written as a quadratic polynomial equation in $(\omega^2 - 1)$ as follows

$$\mathbb{C}_2(\omega^2 - 1)^2 + \mu^2\mathbb{B}_1(\omega^2 - 1) + \mathbb{A}_0\mu^4 + \mathbb{B}_0\mu^2 + \mathbb{C}_0 = 0. \tag{252}$$

The solutions to this equation still give the same contour of course, but the benefit is that now we can set the discriminant of this new quadratic equation to zero[9] and obtain an equation for the minimum point μ_{c1}. This yields the following final

[9] i.e. finding the point where the two real solutions for ω at fixed μ are equal.

equation for μ_{c1} itself

$$\mathbb{D}\mu_{c1}^4 + \mathbb{F}\mu_{c1}^2 + \mathbb{G} = 0, \tag{253}$$

where

$$\mathbb{D} = \mathbb{B}_1^2 - 4\mathbb{A}_0\mathbb{C}_2 = 1 - 2\beta_2^2\left(1 - \frac{2}{\beta_2}\right) - 4\beta_1^2\beta_2^2\left(1 - \frac{2}{\beta_2}\right)^2, \tag{254}$$

$$\mathbb{F} = -4\mathbb{B}_0\mathbb{C}_2 = -\frac{16\beta_1\beta_2}{Q_\Gamma}\left(1 - \frac{2}{\beta_2}\right)\left[\left(1 - \frac{2}{\beta_2}\right)(\beta_1^2 + \beta_2^2) + \frac{3}{2}\right], \tag{255}$$

$$\mathbb{G} = -4\mathbb{C}_0\mathbb{C}_2 = -\frac{16}{Q_\Gamma^2}\left[\left(1 - \frac{2}{\beta_2}\right)(\beta_2^2 + \beta_1^2) + \frac{3}{2}\right]^2. \tag{256}$$

Our first critical coupling μ_{c1} is thus determined in terms of β_1, β_2 and Q_Γ as

$$\mu_{c1}^2 = \frac{-\mathbb{F} \pm \sqrt{\mathbb{F}^2 - 4\mathbb{D}\mathbb{G}}}{2\mathbb{D}}. \tag{257}$$

This can be simplified by noticing that

$$\mathbb{F}^2 - 4\mathbb{D}\mathbb{G} = \left(\frac{8}{Q_\Gamma}\right)^2\left[\left(1 - \frac{2}{\beta_2}\right)(\beta_1^2 + \beta_2^2) + \frac{3}{2}\right]^2\left[1 - 2\beta_2^2\left(1 - \frac{2}{\beta_2}\right)\right]. \tag{258}$$

The resulting expression is then

$$\mu_{c1}^2 = \left(\frac{4}{Q_\Gamma}\right)\frac{2\beta_1\beta_2(1 - \frac{2}{\beta_2}) \pm \sqrt{1 - 2\beta_2^2(1 - \frac{2}{\beta_2})}}{1 - 2\beta_2^2\left(1 - \frac{2}{\beta_2}\right) - 4\beta_1^2\beta_2^2\left(1 - \frac{2}{\beta_2}\right)^2}\left[\left(1 - \frac{2}{\beta_2}\right)(\beta_1^2 + \beta_2^2) + \frac{3}{2}\right], \tag{259}$$

which has the form $(x \pm \sqrt{y})/(y - x^2) = 1/(-x \pm \sqrt{y})$ so that we finally obtain

$$\mu_{c1}^2 = \left(\frac{4}{Q_\Gamma\beta_2}\right)\frac{(\beta_2 - 2)(\beta_1^2 + \beta_2^2) + \frac{3}{2}\beta_2}{-2\beta_1(\beta_2 - 2) \pm \sqrt{1 - 2\beta_2(\beta_2 - 2)}}. \tag{260}$$

We immediately see an important result, the critical coupling μ_{c1} scales with the mechanical quality factor Q_Γ as $\mu_{c1} \propto Q_\Gamma^{-1/2}$.

The dependence on the other two parameters β_1 and β_2 is much more complicated. Firstly it seems that there are multiple solutions, however we can easily show that only one of these is real for a given set of parameters. Writing Eq. (253) as $(\mu_{c1}^2 - u)(\mu_{c1}^2 - v) = 0$ where u and v are the two solutions above, we see that $r = uv$. Since $r < 0$, one solution must be positive and the other negative so that in terms of μ_{c1}, one value is real and the other imaginary. As it turns out, the negative square root solution is only valid in a small range of parameters where $\beta_1 \approx \beta_2$. Since $\beta_2 \gg \beta_1$ for experimentally relevant underdamped junctions, we can simply take

the positive square root solution. In fact in this limit our expression becomes

$$\mu_{c1}^2 \approx \frac{1}{Q_\Gamma} \frac{4\beta_2(\beta_2 - 2) + 6}{\sqrt{1 - 2\beta_2(\beta_2 - 2)}}. \tag{261}$$

The scaling of μ_{c1} with Q_Γ gives an excellent agreement with the numerical results, as we will show in Fig. 43. Numerically μ_{c1} increases with β_2 and decreases slightly with β_1, agreeing with the Eq. (260), but the exact functional form of this equation is not particularly accurate.

There is another important qualitative prediction we can make however, which is that for certain combinations of β_1 and β_2, μ_{c1} diverges so that this mechanically induced retrapping does not occur. The critical value of β_2 is easily shown to be

$$\beta_{2,\text{crit}} = 2 - \frac{1 \pm \sqrt{\beta_1^2 + 3/2}}{1 + 2\beta_1^2}. \tag{262}$$

For low β_1 one root becomes negative and can be ignored, while the other becomes

$$\beta_{2,\text{crit}} = 1 + \sqrt{3/2} \approx 2.225. \tag{263}$$

The numerical results indeed show that such critical value of β_2 does exist, but is higher than predicted analytically with $\beta_{2,\text{crit}} \sim 5$. This disagreement arises due to the assumptions $g \ll \omega$ and $\mu^2 \ll 1$ not holding in this regime. Experimentally, our system must be sufficiently underdamped to achieve resonance as discussed in section 4.2. Furthermore if the system is so underdamped that $\beta_2 > \beta_{2,\text{crit}}$ then the Shapiro plateau is stable with respect to the energy-induced retrapping mechanism discussed here. The value of $\beta_{2,\text{crit}}$ seems fairly low but we should remember that $\beta_2 = \beta_1^2 \beta_c$ where $\beta_1 \ll 1$ so that a small change in β_2 corresponds to a relatively large one in terms of the more physical Stewart-McCumber parameter β_c. In reality we expect it to be fairly difficult to experimentally achieve a junction underdamped enough to reach $\beta_{2,\text{crit}}$.

Now that we have an analytical expression for μ_{c1} we can also find the maximum size of the Shapiro plateau, which is simply $\delta i_{DC}(\omega_{\max}, \mu_{c1})$. Combining Eqs. (224) and (261) we obtain

$$\delta i_{DC}(\omega_{\max}, \mu_{c1}) \approx \frac{1}{4\beta_2} \left[\frac{4(\beta_2 - 2)\beta_2 + 6}{1 - 2\beta_2(\beta_2 - 2)} \right]. \tag{264}$$

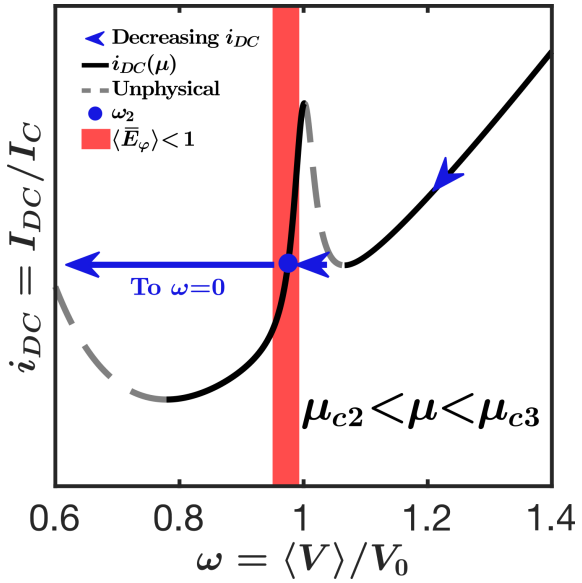

Figure 41: Sketch of $i_{\rm DC}(\omega)$ for $\mu > \mu_{\rm c2}$. As the current is decreased, we reach the bottom of the Ohmic branch and then move horizontally to the point ω_2. When $\mu < \mu_{\rm c2}$, this point is stable and we continue decreasing the current on the plateau until we reach the global minimum before retrapping [see Fig. 38(a)]. However when $\mu > \mu_{\rm c2}$ as shown here, the point ω_2 is in the unstable region $\langle \bar{E}_\varphi \rangle < 1$ so that the system retraps to $\omega = 0$ early rather than forming the plateau. This is the scenario discovered numerically in Fig.36(a).

4.9.2 Second Critical Coupling, μ_{c2}

We see from Fig. 39 that the region $\langle \bar{E}_\varphi \rangle < 1$ widens as μ increases beyond $\mu_{\rm c1}$. At a second critical value $\mu_{\rm c2}$ this region has widened enough that states on the decreasing current path also become unstable. This scenario is sketched in Fig. 41. Ordinarily, i.e. when $\mu < \mu_{\rm c2}$, when decreasing the current we would reach the bottom of the Ohmic branch, move horizontally to the point ω_2 and then continue decreasing the current to reach the global minimum before retrapping [see Fig. 38(a)]. However when $\mu > \mu_{\rm c2}$ the point ω_2 is in the unstable region $\langle \bar{E}_\varphi \rangle < 1$ so that the system retraps to $\omega = 0$ directly rather than forming the plateau. This is precisely what was found in the numerical analysis [see Fig. 36(a)].

To obtain an analytical expression for $\mu_{\rm c2}$ we then must find how the point ω_2 depends on μ, and then find where this intersects with the contour $\langle \bar{E}_\varphi \rangle = 1$. A good approximation for ω_2 when $Q_\Gamma \gg 1$ is the point $\omega_{\rm cross}$ defined in Eq. (221) which we recall is the point where $\delta i_{\rm DC} = 0$. Inserting $\omega = \omega_{\rm cross}$ into our approximate

contour equation Eq. (248) we obtain the following quadratic equation for μ_{c2}

$$\left(\frac{\mathbb{C}_2}{4}-\frac{1}{2}\right)\mu_{c2}^4+\left[\mathbb{B}_0+\left(\frac{\mathbb{C}_2-\mathbb{B}_1}{Q_\Gamma}\right)\left(\frac{\beta_2}{\beta_1}-\frac{\beta_1}{\beta_2}\right)\right]\mu_{c2}^2+\frac{\mathbb{C}_2}{Q_\Gamma^2}\left(4+\left(\frac{\beta_2}{\beta_1}-\frac{\beta_1}{\beta_2}\right)^2\right)=0. \tag{265}$$

Since $\mathbb{B}_0 \propto 1/Q_\Gamma$, we can simply multiply through by Q_Γ^2 and obtain an equation in $\mu_{c2}^2 Q_\Gamma$, showing that $\mu_{c2} \propto Q_\Gamma^{-1/2}$ in the same way as μ_{c1}. The full expression for μ_{c2} is again rather complicated but we can take the limit $\beta_2 \gg \beta_1$ and obtain the following simple expression

$$\mu_{c2}^2 \approx \frac{2\beta_2}{\beta_1 Q_\Gamma}\left(\frac{2}{\sqrt{1-2\beta_2(\beta_2-2)}}-1\right). \tag{266}$$

This predicts that μ_{c2} diverges when $1-2\beta_2(\beta_2-2)\to 0$, which occurs at the same critical β_2 value at which μ_{c1} diverges i.e. $\beta_{2,\mathrm{crit}} \approx 2.225$.

4.9.3 Third Critical Coupling, μ_{c3}

We have seen that when $\mu > \mu_{c2}$ we can no longer decrease the current to reach the plateau without becoming prematurely retrapped. However if we have already decreased the current on to the lower plateau branch before we increase the coupling above μ_{c2}, we can remain on the lower branch. This is precisely what was done numerically in the fixed current, varying magnetic field scenario discussed in section 4.8.2. Our analytics suggest that as μ increases above μ_{c2}, the region $\langle \bar{E}_\varphi \rangle < 1$ continues to expand, causing increasing numbers of solutions to become unstable. This reaches a critical point at some value μ_{c3} where the forbidden region extends all the way down to the global minimum point $\partial i_{\mathrm{DC}}(\omega)/\partial\omega = 0$, rendering all of the plateau states unstable. This scenario is sketched in Fig. 42.

To obtain an analytical expression for our final critical coupling μ_{c3} we first require a value for this global minimum point. Actually, this value does not vary much with the coupling and can be relatively well approximated by its uncoupled value $\partial i_{\mathrm{DC}}^{(0)}(\omega)/\partial\omega = 0$. This is calculated from Eq. (204) to be[10] $\omega \approx (3/2)^{1/4}/\sqrt{\beta_2}$. This value should then be inserted into our contour equation Eq. (244) and solved for μ_{c3}. Note that since ω is not necessarily that close to the resonant region in this case, it does not make sense to use our approximation that (ω^2-1) is small. Similarly μ is not necessarily that small in this regime, leaving the only remaining small quantities as $1/Q_\Gamma$ and β_1. Neglecting terms involving these quantities and

[10]Note that this is just the voltage at the retrapping current I_r and thus scales with β_c in the same way as the exact expression $I_r/I_c = (4/\pi)/\sqrt{\beta_c}$.

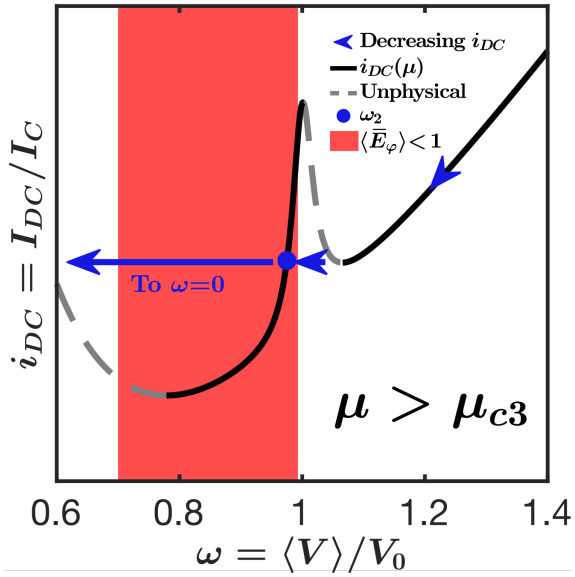

Figure 42: Sketch of $i_{\mathrm{DC}}(\omega)$ for $\mu > \mu_{\mathrm{c3}}$. As we progress towards μ_{c3} fewer and fewer states are stable, reaching a critical point at μ_{c3} where the region $\langle \bar{E}_\varphi \rangle < 1$ extends all the way down to the global minimum point $\partial i_{\mathrm{DC}}(\omega)/\partial\omega = 0$, so that the plateau is unstable for all current values. This is the scenario discovered numerically in Fig. 36(g).

inserting $\omega = (3/2)^{1/4}/\sqrt{\beta_2}$ we obtain

$$\mu_{\mathrm{c3}}^4 + 4\left(1 - \beta_2\sqrt{\frac{2}{3}}\right)\mu_{\mathrm{c3}}^2 + 6\left(1 - \sqrt{\frac{2}{3}}\right)\left(1 - \beta_2\sqrt{\frac{2}{3}}\right)^2 = 0. \tag{267}$$

There are two real solutions to this equation but one is unphysical at a very high μ where our approximations are invalid. We thus require the lower of the two solutions, obtaining

$$\mu_{\mathrm{c3}} \approx \left(\sqrt{2/3}\left(2 - \sqrt{2(\sqrt{6}-1)}\right)\right)^{1/2}\sqrt{\beta_2 - \sqrt{3/2}}. \tag{268}$$

The complicated numerical prefactor amounts to simply $0.493... \approx 1/2$ so that we can make one final approximation

$$\mu_{\mathrm{c3}} \approx \frac{1}{2}\sqrt{\beta_2 - \sqrt{3/2}}. \tag{269}$$

Note that this is independent of Q_Γ which is not surprising since we neglected the small terms involving $1/Q_\Gamma$.

We now have analytical expressions for our three critical coupling values μ_{c1}, μ_{c2} and μ_{c3} in Eqs. (261), (266) and (269) respectively. The analytics suggest that μ_{c1} and μ_{c2} both scale with the mechanical quality factor as $Q_\Gamma^{-1/2}$, while μ_{c3} is

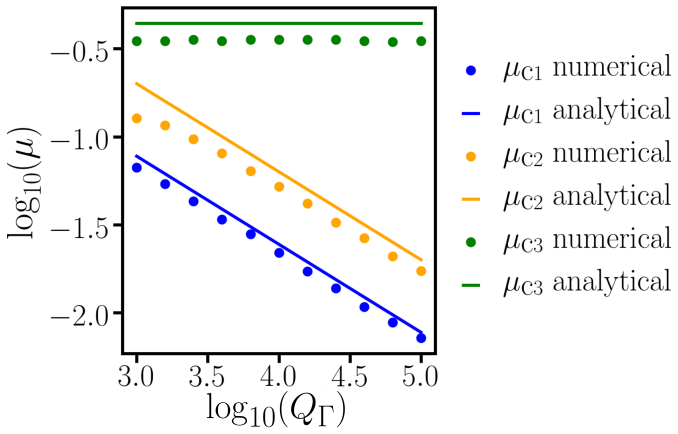

Figure 43: Logarithmic plot of μ_{c1} (blue), μ_{c2} (orange) and μ_{c3} (green) as functions of Q_Γ, with $\beta_1 = 0.1, \beta_2 = 2$. In the high Q_Γ limit, the numerically calculated values (data points) agree well with the analytical values (solid lines) given by Eqs. (261), (266) and (269). Both methods predict that μ_{c1} and μ_{c2} scale as $Q_\Gamma^{-1/2}$ while μ_{c3} is independent of Q_Γ.

independent of Q_Γ. These expressions are compared with numerical results in Fig. 43, showing that the predicted Q_Γ dependence is very accurate for realistic large quality factor devices. For the numerical results shown in Fig. 36 with $\beta_1 = 0.1$, $\beta_2 = 2$ and $Q_\Gamma = 10^3$, we see that $\mu_{c1} = 0.07$, $\mu_{c2} = 0.12$ and $\mu_{c3} = 0.36$, while the analytics predict that $\mu_{c1} = 0.08$, $\mu_{c2} = 0.2$ and $\mu_{c3} = 0.44$. Thus our analytics provide good order of magnitude estimates, as well as predicting the correct Q_Γ dependencies.

A summary of all the different coupling regimes is given in Fig. 44, with panels (a-d) showing the possible transitions. Panel (e) shows the region $\langle \bar{E}_\varphi \rangle < 1$ and how the three critical μ values are defined. The minimum point defines μ_{c1}, the intersection of the region with $\omega_2(\mu)$ defines μ_{c2} and the intersection with the line $\partial i_{DC}/\partial\omega = 0$, visible in the inset, defines μ_{c3}. The grey regions are the unphysical solutions where $\partial i_{DC}/\partial\omega < 0$. This plot shows that our analytics predicts an additional stable region for strong coupling to the right of the region $\langle \bar{E}_\varphi \rangle < 1$ very close to the top of the resonant peak. However it is not clear that this region exists experimentally since our analytics are expected to break down here where the approximation $g/\omega \ll 1$ fails.

4.10 Additional Plateaus

So far we have analyzed only the main Shapiro plateau at $\omega = 1$, but in reality there can exist additional mechanically induced plateaus at any fractional frequency $\omega = n/m$ where n and m are natural numbers. Actually, two steps at $\omega = 2/3$ and

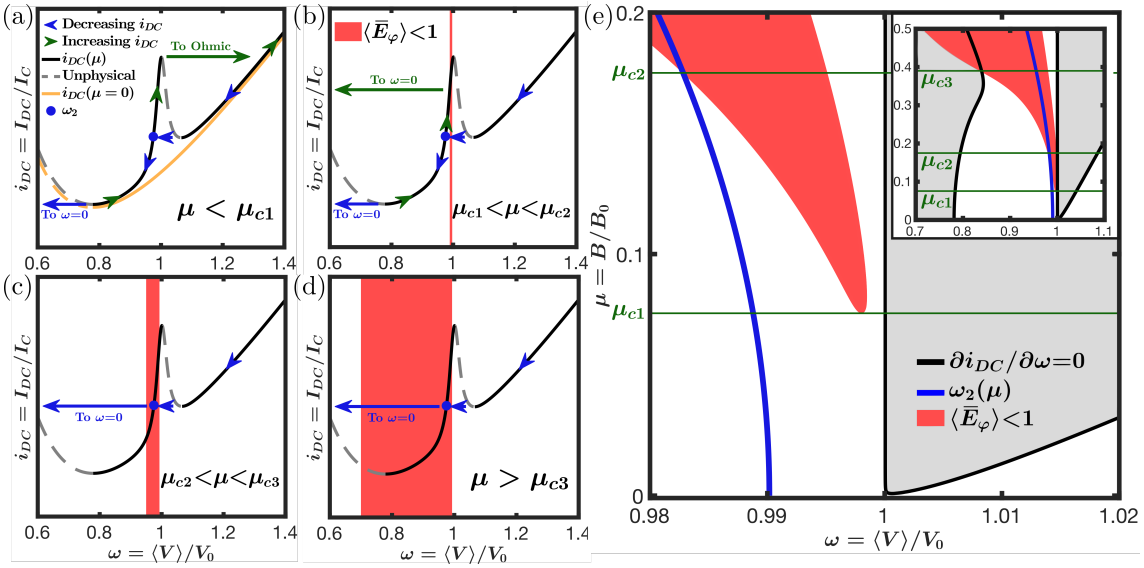

Figure 44: (a-d) Sketches of bias current as a function of voltage, $i_{\rm DC}(\omega)$, for various coupling regimes ($Q_\Gamma = 50$ for illustrative purposes). (a) $\mu < \mu_{\rm c1}$ - a finite coupling introduces a resonance peak on top of the uncoupled ($\mu = 0$) profile, plotted in yellow. This creates a hysteresis loop, with the decreasing and increasing current paths plotted with blue and green arrows respectively, while unphysical solutions are shown as grey dashed lines. Reducing $i_{\rm DC}$ on the Ohmic ($\omega > 1$) branch to the minimum causes a transition to the frequency ω_2 (blue dot) on the plateau. (b) $\mu_{\rm c1} < \mu < \mu_{\rm c2}$ - a range of frequencies (red regions) have a critically low electronic energy ($\langle \bar{E}_\varphi \rangle < 1$) and are thus unstable. The system retraps to $\omega = 0$ as this region is entered on the increasing current path. (c) $\mu_{\rm c2} < \mu < \mu_{\rm c3}$ - the solution at ω_2 is unstable so that the system retraps to $\omega = 0$ on the decreasing current path. (d) $\mu > \mu_{\rm c3}$ - the whole plateau becomes unstable. (e) A contour plot illustrating the various regions in the space (ω, μ). The black lines are $\partial i_{\rm DC}/\partial\omega = 0$ contours, separating the physical/unphysical solutions (white/grey regions). The blue line is the solution $\omega_2(\mu)$, and the red region again represents the energy unstable solutions. The minimum of the unstable region defines $\mu_{\rm c1}$, while the intersection of this region with the lines $\omega_2(\mu)$ and $\partial i_{\rm DC}/\partial\omega = 0$ define $\mu_{\rm c2}$ and $\mu_{\rm c3}$ respectively.

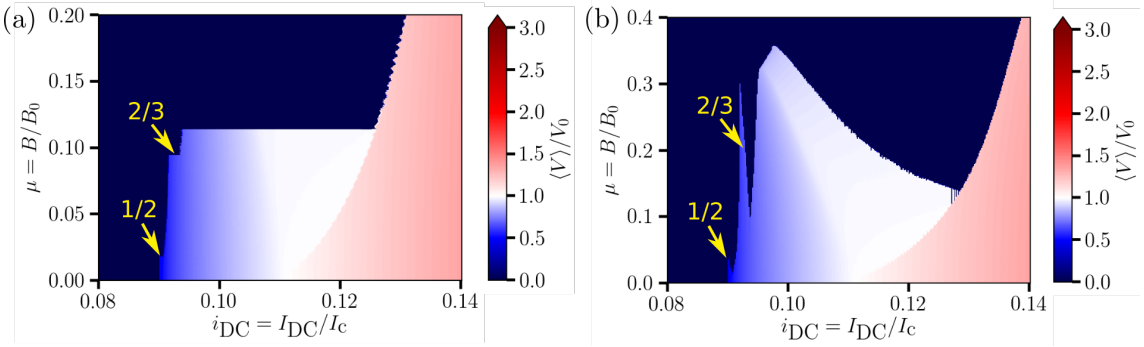

Figure 45: (a) DC voltage $\langle V \rangle$ as a function of i_{DC} and μ for a decreasing current experiment at fixed coupling [reproduction of Fig. 36(a)], highlighting the existence of fractional Shapiro steps at $\omega = 2/3$ and $\omega = 1/2$. (b) DC voltage $\langle V \rangle$ as a function of i_{DC} and μ for an increasing coupling experiment at fixed current [reproduction of Fig. 36(g)], highlighting that these fractional Shapiro steps extend into spike-like features in the same way as the main $\omega = 1$ plateau. These fractional Shapiro steps are associated with their own energy induced retrappings and critical coupling values.

$\omega = 1/2$ are visible already in our decreasing current color plot Fig. 36(a). This plot is reproduced in Fig. 45(a) with the additional steps highlighted. When increasing the coupling at fixed current, these steps extend into spike-like features in the same way as the main $\omega = 1$ plateau, as highlighted in Fig. 45(b). These additional steps are each associated with their own critical coupling values.

A zoom of the $\omega = 1/2$ plateau on the decreasing current path is shown in Fig. 46. This shows an almost identical form to the main $\omega = 1$ plateau which really highlights the self-similar, or fractal, nature of our non-linear equations of motion Eqs. (140) and (141). Further sub-plateaus at smaller fractions are even visible in this zoomed plot. Earlier we discussed that above a critical value of β_2 the energy-induced retrapping on the main $\omega = 1$ plateau do not occur. However, retrapping does still occur on these smaller plateaus, themselves being associated with higher critical β_2 values.

Our analytics of course fails to capture these additional plateaus since we included only terms oscillating at a single frequency ω. In principle it is possible, but challenging, to include higher frequency components and obtain a general theory for the $\omega = n/m$ Shapiro plateau.

4.11 Finite Temperature Effects

In order to experimentally observe the phenomena discussed here, temperatures must be below the critical temperature T_c of the superconducting contacts. These

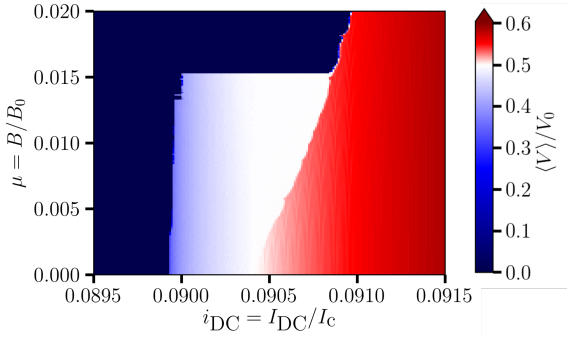

Figure 46: Zoom of the DC voltage plot Fig. 45(a) around the $\omega = 1/2$ plateau, showing how similar it is in form to the main plateau. This smaller plateau is even associated with its own critical coupling value at which there is an increase in the retrapping current.

contacts could be realised with rigid nanostructures based on e.g. niobium nitride [72] or molybdenum rhenium [76] with rather high $T_c \approx 10\mathrm{K}$. Even at these temperatures thermal currents and displacements may exceed the typical scales I_{DC} and x_0, disrupting the experimental signatures. We analysed temperature effects by including a Johnson-Nyquist noise current $\tilde{i}$ to our equations of motion with correlation function

$$\langle \tilde{i}(\tau)\tilde{i}(\tau')\rangle = 2\beta_1 \frac{T}{T_J}\delta(\tau - \tau'), \tag{270}$$

where T_J is a temperature scale related to the Josephson energy $\hbar I_{\mathrm{c}}/2e = k_B T_J$. To minimize the effects of temperature the thermal energy $k_B T$ must be less than the energy scale $\hbar I_{\mathrm{DC}}/2e$ associated with the current I_{DC} i.e. $T < \beta_1 T_J$. In terms of physical parameters, this condition reads

$$k_B T < \left(\frac{\hbar}{2e}\right)^2 \frac{\omega_0}{R}, \tag{271}$$

so that experiments may be optimised using devices with low resistances and high mechanical resonance frequencies. For state of the art CNT devices with $\omega_0 \approx 10\mathrm{GHz}$ [63, 64] and $R \approx 1\mathrm{k}\Omega$ [27, 73] we find $T < 100\mathrm{mK}$.

5 SQUIDs

In 1964, two years after Josephson discovered the Josephson effect, Robert Jaklevic, John Lambe, James Mercereau, and Arnold Silver invented the SQUID (superconducting quantum interference device) [26]. A SQUID consists of two Josephson junctions connected in parallel, forming a superconducting loop. An applied magnetic flux through the loop produces quantum interference between the two junctions so that the total supercurrent becomes sensitively dependent on the applied field. SQUIDs thus make extremely good magnetometers, being able to measure magnetic fields down to 10^{-15}T [77]. In this chapter we will first develop the theory of ordinary DC SQUIDs that have no mechanically vibrating parts. We will then move on to consider SQUIDs where one or both arms may be free to mechanically oscillate, extending our work of the previous sections. The external flux will prove to be a useful experimentally variable parameter, allowing us to redirect the current flow between the two arms. In particular we can choose which of the two arms to excite, or even whether they oscillate in a symmetric or antisymmetric mode. The two arms of the electromechanically coupled SQUID can thus allow the creation of two distinct states that can be switched between controllably.

5.1 DC SQUIDs

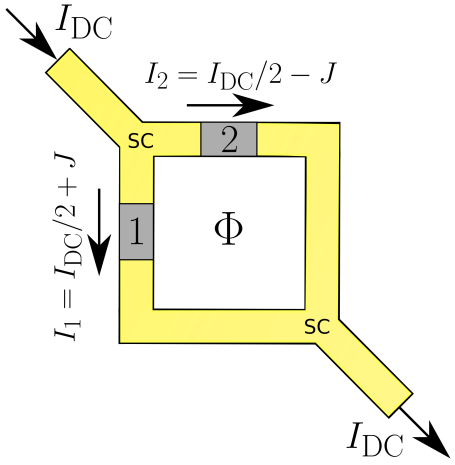

Figure 47: Sketch of a DC SQUID, which consists of a superconductor that branches into two arms which later recombine forming a loop. Inside each arm are Josephson junctions (grey regions) that are associated with their own phase differences φ_1 and φ_2. The SQUID is biased with a DC current I_{DC} and a magnetic field is applied such that a magnetic flux Φ penetrates the loop. This flux imposes a constraint on φ_1 and φ_2 as well as inducing a circulating current J so that the current flowing in the two arms are $I_1 = I_{\mathrm{DC}}/2 + J$ and $I_2 = I_{\mathrm{DC}}/2 - J$.

A DC SQUID is sketched in Fig. 47. Two Josephson junctions are connected in parallel in an otherwise superconducting loop that is biased with a DC current I_{DC}. The current is not split symmetrically in both arms but differs due to a circulating current J that is induced by an applied magnetic flux Φ that penetrates the loop. The current in the two arms can thus be expressed as $I_1 = I_{\mathrm{DC}}/2 + J$ and $I_2 = I_{\mathrm{DC}}/2 - J$. Each junction hosts a supercurrent $I_{cn} \sin \varphi_n$ where φ_n is the gauge-invariant phase difference, related to the voltage drop V_n across the junction by the usual Josephson relation

$$\frac{\mathrm{d}\varphi_n}{\mathrm{d}t} = \frac{2e}{\hbar}\left(V_n - \frac{\mathrm{d}}{\mathrm{d}t}\int \mathbf{A}\cdot d\mathbf{l}\right), \tag{272}$$

derived in section 3.2. In the present case we consider a constant external magnetic field and Josephson junctions that do not mechanically oscillate so that the second term of Eq. (272) does not contribute. Using the now familiar RCSJ model, we can also write down the resistive and capacitive current contributions, V_n/R_n and $C_n \mathrm{d}V_n/\mathrm{d}t$ respectively. In all the above expressions, the subscript $n = 1, 2$ labels the two separate junctions and for generality we have allowed them to have different critical currents I_{cn}, normal state resistances R_n and inter-electrode capacitances C_n. Current conservation in the two arms thus yields the following two equations

$$\frac{I_{\mathrm{DC}}}{2} + J = I_{\mathrm{c1}} \sin \varphi_1 + \frac{\hbar}{2eR_1}\frac{\mathrm{d}\varphi_1}{\mathrm{d}t} + \frac{\hbar C_1}{2e}\frac{\mathrm{d}^2\varphi_1}{\mathrm{d}t^2}, \tag{273}$$

$$\frac{I_{\mathrm{DC}}}{2} - J = I_{\mathrm{c2}} \sin \varphi_2 + \frac{\hbar}{2eR_2}\frac{\mathrm{d}\varphi_2}{\mathrm{d}t} + \frac{\hbar C_2}{2e}\frac{\mathrm{d}^2\varphi_2}{\mathrm{d}t^2}. \tag{274}$$

To completely describe our system we also require a third equation that relates φ_1 and φ_2 to the flux through the loop. This is derived by ensuring that the superconducting phase ϕ is single valued as we now show.

5.1.1 Flux Relation

Applying Stokes' law we can find the total magnetic flux penetrating the SQUID by integrating the vector potential $\mathbf{A}$ anticlockwise around the loop shown in Fig. 47. The fact that the arms have finite width does not matter, we can take the integral as far inside the electrodes as we like, since no flux penetrates them by virtue of

them being superconducting. [11] This integral then produces

$$\oint \mathbf{A} \cdot \mathbf{dl} = \int_{\text{sc}} \mathbf{A} \cdot \mathbf{dl} + \int_{\text{link 1}} \mathbf{A} \cdot \mathbf{dl} - \int_{\text{link 2}} \mathbf{A} \cdot \mathbf{dl}, \tag{275}$$

where the integral over the two weak links are separated from the integral over the superconducting electrodes and we have reversed the final integral so that it is taken in the direction of current flow.

The real (non-gauge invariant) superconducting phase ϕ is related to the vector potential and supercurrent velocity $\mathbf{v}_s$ by the canonical momentum relation

$$\hbar \nabla \phi = 2m\mathbf{v}_s + 2e\mathbf{A}, \tag{276}$$

where m is the mass of an electron and the factors of two arise due to the charge carriers being Cooper pairs. Deep in the electrodes the supercurrent velocity is zero, by virtue of Eq. (4), so that

$$\mathbf{A} = \frac{\hbar}{2e} \nabla \phi \, (\text{in electrodes}). \tag{277}$$

Inserting this into Eq. (275), it becomes

$$\oint \mathbf{A} \cdot \mathbf{dl} = \frac{\hbar}{2e} \int_{\text{sc}} \nabla \phi \cdot \mathbf{dl} + \int_{\text{link 1}} \mathbf{A} \cdot \mathbf{dl} - \int_{\text{link 2}} \mathbf{A} \cdot \mathbf{dl}. \tag{278}$$

The integral over the electrodes may be simplified by realising that the phase ϕ must be single valued so that this integral plus the phase differences ϕ_1, ϕ_2 across the weak links must be zero (mod 2π)

$$\int_{\text{sc}} \nabla \phi \cdot \mathbf{dl} + \phi_1 - \phi_2 = 0 \, (\text{mod } 2\pi). \tag{279}$$

Here we have again reversed ϕ_2 so that it gives the phase difference in the direction of current flow. We thus have

$$\frac{2e}{\hbar} \oint \mathbf{A} \cdot \mathbf{dl} = \left(\phi_2 - \frac{2e}{\hbar} \int_{\text{link 1}} \mathbf{A} \cdot \mathbf{dl} \right) - \left(\phi_1 - \frac{2e}{\hbar} \int_{\text{link 2}} \mathbf{A} \cdot \mathbf{dl} \right) \, (\text{mod } 2\pi). \tag{280}$$

The bracketed expressions on the right hand side are just the definitions of the gauge

[11] Assuming that the dimensions of the SQUID arms are large compared to the London penetration depth.

invariant phase differences φ_1,φ_2 across the two weak links, so that we can write

$$\varphi_2 - \varphi_1 = \frac{2e}{\hbar} \oint \mathbf{A} \cdot \mathbf{dl} \,(\text{mod } 2\pi). \tag{281}$$

The total magnetic flux may differ from the applied contribution Φ due to the natural inductance of the loop. We can account for this by assigning each arm an effective inductance L_n and writing the total flux as

$$\oint \mathbf{A} \cdot \mathbf{dl} = \Phi + L_1 I_1 - L_2 I_2 = \Phi + (L_1 - L_2)\frac{I_{\text{DC}}}{2} + (L_1 + L_2)J. \tag{282}$$

Eq. (281) can then finally be written as

$$\varphi_2 - \varphi_1 = \frac{2\pi}{\Phi_0}\left[\Phi + (L_1 - L_2)\frac{I_{\text{DC}}}{2} + (L_1 + L_2)J\right] (\text{mod } 2\pi), \tag{283}$$

where we have introduced the flux quantum $\Phi_0 = h/2e$. This equation provides an extra constraint for our system and thus when combined with our two equations of motion (273) and (274), the variables φ_1, φ_2 and J are completely determined.

5.1.2 Voltage

We can calculate the voltage across the device

$$V = \frac{\hbar}{2e}\frac{\mathrm{d}\varphi_1}{\mathrm{d}t} + L_1\frac{\mathrm{d}I_1}{\mathrm{d}t} = \frac{\hbar}{2e}\frac{\mathrm{d}\varphi_2}{\mathrm{d}t} + L_2\frac{\mathrm{d}I_2}{\mathrm{d}t}. \tag{284}$$

One can check that the same voltage is obtained by traversing either of the two arms by taking the time derivative of the flux relation Eq. (283). We can also express the voltage in a symmetric form

$$V = \frac{1}{2}\left[\frac{\hbar}{2e}\left(\frac{\mathrm{d}\varphi_1}{\mathrm{d}t} + \frac{\mathrm{d}\varphi_2}{\mathrm{d}t}\right) + (L_1 - L_2)\frac{\mathrm{d}J}{\mathrm{d}t}\right], \tag{285}$$

$$V = \frac{\hbar}{2e}\left(\frac{L_2}{L}\frac{\mathrm{d}\varphi_1}{\mathrm{d}t} + \frac{L_1}{L}\frac{\mathrm{d}\varphi_2}{\mathrm{d}t}\right), \tag{286}$$

where in the second equality we have inserted J from Eq. (283), and written the total inductance of the loop as $L = L_1 + L_2$.

5.1.3 Dimensionless Equations

For simplicity, from now on we shall assume that the inductances of both arms are identical $L_1 = L_2 = L/2$. The flux term proportional to I_{DC} in Eq. (283) then

vanishes, which in any case is a small contribution and only produces a constant shift to the applied flux Φ. We will also no longer explicitly write (mod 2π) when employing the flux equation (283), with the understanding that φ_1 and φ_2 are phases and of course only physical modulo 2π.

Our three equations can be made dimensionless by introducing the average critical current $I_\mathrm{c} = (I_{\mathrm{c}1} + I_{\mathrm{c}2})/2$, average capacitance $C = (C_1 + C_2)/2$ and twice the parallel resistance of the SQUID $R = 2R_1R_2/(R_1 + R_2)$. We can then measure currents in units $i_\mathrm{DC} = I_\mathrm{DC}/I_\mathrm{c}$, $j = J/I_\mathrm{c}$, applied flux in units of the flux quantum $\phi_\mathrm{a} = \Phi/\Phi_0$ and time in units $\tau_\mathrm{c} = \omega_\mathrm{c}t$ where $\omega_\mathrm{c} = 2eI_\mathrm{c}R/\hbar$. We can also introduce the Stewart-McCumber parameter $\beta_\mathrm{c} = \omega_\mathrm{c}RC$ and dimensionless inductance $\beta_L = 2I_\mathrm{c}L/\Phi_0$. This is an obvious generalisation of how we non-dimensionalized the single junction in section 3.3. Eqs. (273), (274) and (283) can then be expressed as

$$\frac{i_\mathrm{DC}}{2} + j = (1 - \alpha_I)\sin\varphi_1 + (1 - \alpha_R)\dot{\varphi}_1 + \beta_\mathrm{c}(1 - \alpha_C)\ddot{\varphi}_1, \tag{287}$$

$$\frac{i_\mathrm{DC}}{2} - j = (1 + \alpha_I)\sin\varphi_2 + (1 + \alpha_R)\dot{\varphi}_2 + \beta_\mathrm{c}(1 + \alpha_C)\ddot{\varphi}_2, \tag{288}$$

$$\varphi_2 - \varphi_1 = 2\pi\left(\phi_\mathrm{a} + \frac{1}{2}\beta_L j\right), \tag{289}$$

where $\alpha_I = (I_{c2} - I_{c1})/(I_{c1} + I_{c2})$, $\alpha_R = (R_1 - R_2)/(R_1 + R_2)$ and $\alpha_C = (C_2 - C_1)/(C_1 + C_2)$ characterise asymmetries in the junction critical currents, resistances and capacitances.

The voltage can then be expressed in units of $I_\mathrm{c}R$ from Eq. (284) as

$$\frac{V}{I_\mathrm{c}R} = \dot{\varphi}_1 + \frac{\pi\beta_L}{2}\dot{j} = \dot{\varphi}_2 - \frac{\pi\beta_L}{2}\dot{j}, \tag{290}$$

or, in symmetric form

$$\frac{V}{I_\mathrm{c}R} = \frac{\dot{\varphi}_1 + \dot{\varphi}_2}{2}. \tag{291}$$

A Lagrangian formulation for the uncoupled SQUID is presented in appendix A.

5.1.4 Static Solutions

We will first consider the simplest case of identical junctions $\alpha_I = \alpha_R = \alpha_C = 0$ and look for static solutions. Eqs. (287) and (288) then simplify considerably to

$$\frac{i_\mathrm{DC}}{2} + j = \sin\varphi_1, \tag{292}$$

$$\frac{i_\mathrm{DC}}{2} - j = \sin\varphi_2, \tag{293}$$

and if we further assume that the inductance is low, $\beta_L \ll 1$, then the flux relation Eq. (289) reduces to

$$\varphi_2 - \varphi_1 = 2\pi\phi_\mathrm{a}. \tag{294}$$

From these equations we find $i_\mathrm{DC} = \sin\varphi_1 + \sin(\varphi_1 + 2\pi\phi_\mathrm{a})$, which can be written as

$$i_\mathrm{DC} = 2\sin(\varphi_1 + \pi\phi_\mathrm{a})\cos(\pi\phi_\mathrm{a}). \tag{295}$$

If we apply a bias current, φ_1 will adjust so that this equation is fulfilled. The maximum supercurrent before we must include dissipative currents is then obtained for $\sin(\varphi_1 + \pi\phi_\mathrm{a}) = \pm 1$. In other words, the SQUID acts as a single junction with a modified critical current

$$I_\mathrm{c}' = 2I_\mathrm{c}|\cos(\pi\phi_\mathrm{a})|, \tag{296}$$

which is heavily dependent on the applied flux. This function is plotted as a blue line in Fig. 48, showing that the maximum supercurrent I_c' is periodic in the applied flux with a period equal to the flux quantum $\Phi_0 = h/2e \approx 2 \times 10^{-15}$Wb. When an integer number of flux quanta penetrate the loop, the superconducting phases are equal $\varphi_1 = \varphi_2$, and thus the supercurrents in both arms flow in the same direction giving $I_\mathrm{c}' = 2I_\mathrm{c}$. However when there is a half integer number of flux quanta, the phases are half a cycle out of phase $\varphi_2 = \varphi_1 + \pi$ so that the supercurrents flow in opposite directions and cancel out yielding $I_\mathrm{c}' = 0$. A small change in the applied flux of the order of one flux quantum can thus produce a large change in the supercurrent, which is the basic principle behind SQUID magnetometers [77].

Plots of I_c' for non-zero inductance $\beta_L \neq 0$ have been calculated numerically and are given in Fig. 48, which shows that the basic principle remains unchanged, I_c' is still periodic in Φ with period Φ_0. The only major change is that the minimum value of I_c' is raised from zero. This is due to the circulating current J being induced that keeps the total flux $\phi_\mathrm{a} + \beta_L j/2$ close to an integer number of flux quanta.

5.1.5 Dynamic Solutions

To study the dynamic solutions to Eqs. (287), (288) and (289) it is convenient to perform a change of variables to $\varphi_+ = (\varphi_1 + \varphi_2)/2$ and $\varphi_- = (\varphi_1 - \varphi_2)/2$. The flux relation is then given by

$$\varphi_- = -\pi(\phi_\mathrm{a} + \beta_L j/2), \tag{297}$$

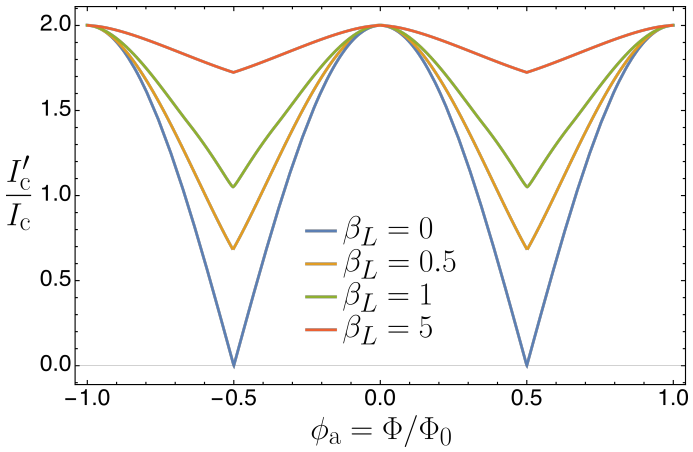

Figure 48: The maximum supercurrent of the SQUID I_c' as a function of the applied flux Φ. This modified critical current is periodic in Φ with a period equal to the flux quantum $\Phi_0 = h/2e$. It is maximum for integer number of flux quantum, $I_c' = 2I_c$, since the supercurrent flows in the same direction in both arms and minimum for half integer number of flux quantum where the supercurrents in both arms tend to cancel out. For zero loop inductance, $\beta_L = 0$ (blue line), this cancellation is perfect and $I_c' = 0$, but for finite inductance (orange, green and red lines) the minimum value is raised due to the circulating current J inducing an extra flux on top of the applied value Φ.

while the other two equations become

$$i_{DC} = 2\cos(\pi\phi_a + \pi\beta_L j/2)\sin\varphi_+ + 2\dot{\varphi_+} + 2\beta_c\ddot{\varphi_+}, \tag{298}$$

$$j = -\sin(\pi\phi_a + \pi\beta_L j/2)\cos\varphi_+ - \frac{\pi\beta_L}{2}\dot{j} - \frac{\pi\beta_c\beta_L}{2}\ddot{j}. \tag{299}$$

where we have again assumed symmetric junctions, $\alpha_I = \alpha_R = \alpha_C = 0$, and inserted Eq. (297) to obtain two coupled equations in φ_+ and j. The voltage Eq. (291) becomes simply

$$\frac{V}{I_c R} = \dot{\varphi_+}. \tag{300}$$

In the limit $\beta_L \ll 1$, Eq. (298) becomes decoupled and is identical to the RCSJ equation for a single junction with a critical current $2I_c\cos(\pi\phi_a)$, resistance $R/2$ and capacitance $2C$.[12] If we are also in the overdamped limit $\beta_c \ll 1$ we can follow the same logic as in section 3.3.2 and exactly solve for the DC voltage as

$$\langle V\rangle = \frac{R}{2}\sqrt{I_{DC}^2 - I_c'^2}. \tag{301}$$

where I_c' is given by Eq. (296) [cf. Eq. (100) for a single junction]. SQUIDs used in practical magnetometers are usually made to satisfy $\beta_L, \beta_c \ll 1$ to eliminate

[12]This resistance and capacitance are simply those of the two arms taken in parallel.

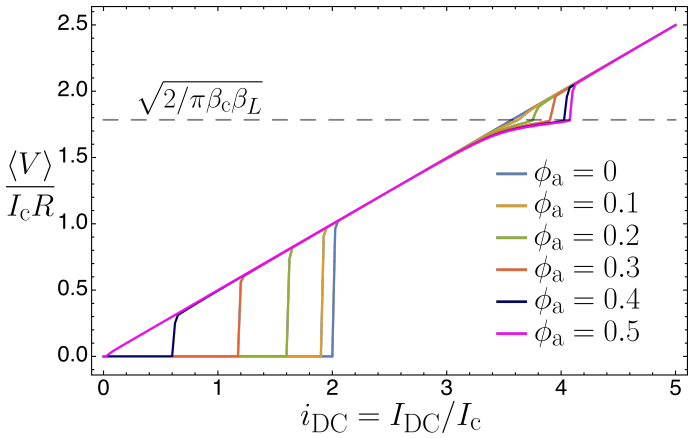

Figure 49: Increasing current I-V curve of a symmetric SQUID calculated from Eqs. (298) and (299). The junction is underdamped with $\beta_c = 10$ and a finite inductance $\beta_L = 0.02$. Plots for various values of applied flux $\phi_a = \Phi/\Phi_0$ from integer flux, $\phi_a = 0$, to half integer flux, $\phi_a = 0.5$, are given (ϕ_a is only physical modulo 1 and the system is symmetric around the point $\phi_a = 0.5$). The modification of the effective critical current I_c' is clearly visible, as well as the addition of a new plateau at a value $\langle V\rangle/I_cR = \sqrt{2/\pi\beta_c\beta_L}$. This plateau is due to an internal LC resonance and thus appears when $\langle \mathrm{d}\varphi_+/\mathrm{d}t\rangle = \sqrt{2/LC}$. Since it is induced by the circulating current the plateau is most prominent at half integer flux and vanishes for integer flux.

both magnetic hysteresis and hysteresis in the I-V curve, so that Eq. (301) is widely used [60]. If the junction is instead underdamped there is no exact analytical solution, but if one can still neglect the inductance, $\beta_L \ll 1$, the SQUID displays all the same behaviour as the single junction discussed in section 3.3.3.

In the more interesting case where both β_c and β_L are finite there is an interesting new phenomenon. The increasing current I-V curves in Fig. 49, calculated from Eqs. (298) and (299), show that a new voltage plateau develops at a finite voltage. Our knowledge of Shapiro plateaus immediately leads us to the conclusion that this must be due to some internal resonance in the circuit. We also expect it to be related to the circulating current since the plateau vanishes at integer flux quantum when there is little circulating current, and reaches maximum size at half integer flux quantum when the circulating current is large. Such steps have been observed experimentally and are due to an LC resonance in the loop induced by the circulating current [78, 79]. The steps thus appear at a frequency $2e\langle V\rangle/\hbar = \langle \mathrm{d}\varphi_+/\mathrm{d}t\rangle = \sqrt{2/LC}$, or in dimensionless units $\langle V\rangle/I_cR = \langle \dot{\varphi}_+\rangle = \sqrt{2/\pi\beta_c\beta_L}$. In fact Eq. (299) can be interpreted as an oscillator equation in j at exactly this frequency, but with an additional non-linear term. The current flowing in each arm thus acquires a component oscillating at this frequency and a Shapiro-like plateau develops. The factor of two arises due to the fact that the total capacitance of the loop taken in

series is $C/2$.

We will now move on to allow the possibility of the two weak links to mechanically oscillate, extending our work of the previous chapter. It is important that we discussed the above LC resonances because it may be necessary in an experiment to distinguish between these Shapiro steps and those due to mechanical oscillations.

5.2 SQUID-Mechanical Coupling

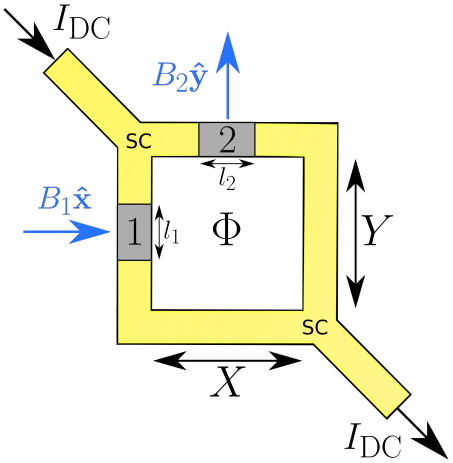

Figure 50: The two weak links that make up the DC SQUID are now suspended and allowed to oscillate out of the plane. The SQUID is exposed to a total magnetic field $\mathbf{B} = B_1\hat{\mathbf{x}} + B_2\hat{\mathbf{y}} + B_3\hat{\mathbf{z}}$, where B_3 controls the applied flux as before while B_1 and B_2 excite mechanical oscillations in the two weak links via the Lorentz force.

We now couple the current flowing through the SQUID to mechanical oscillations in the same way as we did in the single junction case. The SQUID is exposed to a total magnetic field $\mathbf{B} = B_1\hat{\mathbf{x}} + B_2\hat{\mathbf{y}} + B_3\hat{\mathbf{z}}$ such that oscillations in the two weak links are forced independently by B_1 and B_2 while B_3 penetrates the whole loop inducing the applied flux Φ. The supercurrent in each junction is still I_{cn} but Eq. (272) which gives the relation between V_n and φ_n now becomes

$$\frac{\mathrm{d}\varphi_n}{\mathrm{d}t} = \frac{2e}{\hbar}\left(V_n - B_n l_n \frac{\mathrm{d}x_n}{\mathrm{d}t}\right), \tag{302}$$

where l_n are the length of the weak links and x_n are their displacements in the $\hat{\mathbf{z}}$ direction. Analogously to the single junction case, the normal and displacement currents are given by $(V_n - B_n l_n \mathrm{d}x_n/\mathrm{d}t)/R_n$ and $C_n \mathrm{d}V_n/\mathrm{d}t$ respectively, so that the

current conservation equations are

$$\frac{I_{\mathrm{DC}}}{2} + J = I_{c1}\sin\varphi_1 + \frac{\hbar}{2eR_1}\frac{\mathrm{d}\varphi_1}{\mathrm{d}t} + \frac{\hbar C_1}{2e}\frac{\mathrm{d}^2\varphi_1}{\mathrm{d}t^2} + C_1B_1l_1\frac{\mathrm{d}^2x_1}{\mathrm{d}t^2}, \tag{303}$$

$$\frac{I_{\mathrm{DC}}}{2} - J = I_{c2}\sin\varphi_2 + \frac{\hbar}{2eR_2}\frac{\mathrm{d}\varphi_2}{\mathrm{d}t} + \frac{\hbar C_2}{2e}\frac{\mathrm{d}^2\varphi_2}{\mathrm{d}t^2} + C_2B_2l_2\frac{\mathrm{d}^2x_2}{\mathrm{d}t^2}. \tag{304}$$

The flexural modes of each weak link are again modelled as harmonic oscillators with masses M_n, resonance frequencies ω_n, damping coefficients Γ_n and quality factors $Q_{\Gamma n} = \omega_n/\Gamma_n$. Each oscillator is excited by a Lorentz force that acts on the supercurrent and normal currents so that the two mechanical equations of motion are

$$M_1\frac{\mathrm{d}^2x_1}{\mathrm{d}t^2} + 2M_1\Gamma_1\frac{\mathrm{d}x_1}{\mathrm{d}t} + M_1\omega_1^2x_1 = B_1l_1\left(I_{c1}\sin\varphi_1 + \frac{\hbar}{2eR_1}\frac{\mathrm{d}\varphi_1}{\mathrm{d}t}\right), \tag{305}$$

$$M_2\frac{\mathrm{d}^2x_2}{\mathrm{d}t^2} + 2M_2\Gamma_2\frac{\mathrm{d}x_2}{\mathrm{d}t} + M_2\omega_2^2x_2 = B_2l_2\left(I_{c2}\sin\varphi_2 + \frac{\hbar}{2eR_2}\frac{\mathrm{d}\varphi_2}{\mathrm{d}t}\right). \tag{306}$$

We then have four differential equations in the five unknowns φ_1, φ_2, x_1, x_2 and J. We must again use the flux relation to impose another constraint.

5.2.1 Flux Relation

The relation between φ_1, φ_2 and the total flux was derived in section 5.1.1 as

$$\varphi_2 - \varphi_1 = \frac{2e}{\hbar}\oint \mathbf{A}\cdot\mathbf{dl}. \tag{307}$$

Naïvely one might assume that the total flux is $\oint \mathbf{A}\cdot\mathbf{dl} = \Phi + L_1I_1 - L_2I_2$ as in the uncoupled case. Let's be more thorough and actually write down the vector potential for our system and perform the integration. As the flux is gauge-invariant we can freely choose the vector potential to be

$$\mathbf{A} = B_2z\hat{\mathbf{x}} + (B_3x - B_1z)\hat{\mathbf{y}}. \tag{308}$$

For ease of calculation we shall assume a square geometry as shown in Fig. 50 where the whole SQUID has dimensions of X, Y, while the junctions themselves have lengths l_1, l_2. The whole loop is in the $z = 0$ plane, except the junctions which are displaced by $z = x_1$ and $z = x_2$ respectively. We can then split the integral up over the four sides of the SQUID, remembering that the integral is taken

anticlockwise. The contribution from the bottom edge where $y = z = 0$ is

$$\int_0^X B_2 z dx = 0. \tag{309}$$

Similarly for the right side where $x = X$, $z = 0$ we have

$$\int_0^Y (B_3 x - B_1 z) dy = B_3 XY = \Phi. \tag{310}$$

At the top $y = Y$, $z = 0$ except over a distance l_2 where $z = x_2$ so that it contributes

$$\int_X^0 B_2 z dx = -B_2 x_2 l_2. \tag{311}$$

Finally at the left edge $x = 0$, $z = 0$ except over a distance l_1 where $z = x_1$, contributing

$$\int_Y^0 (B_3 x - B_1 z) dy = B_1 x_1 l_1. \tag{312}$$

If we then add the contribution due to the inductances L_1 and L_2 as before, the total flux is

$$\oint \mathbf{A} \cdot \mathbf{dl} = \Phi + B_1 x_1 l_1 - B_2 x_2 l_2 + L_1 I_1 - L_2 I_2. \tag{313}$$

Thus there is an extra contribution to the flux due to the mechanical oscillations. When x_1 and x_2 are non-zero the whole loop does not lie in the $z = 0$ plane so that the field B_1 penetrates an area $x_1 l_1$ while B_2 penetrates an area $x_2 l_2$. While this may seem like a small contribution we will see that we must include this extra flux for our resulting equations to be consistent and to be able to write down a Lagrangian. The flux relation Eq. (307) is then

$$\varphi_2 - \varphi_1 = \frac{2\pi}{\Phi_0} \left[\Phi + B_1 x_1 l_1 - B_2 x_2 l_2 + (L_1 - L_2) \frac{I_{\mathrm{DC}}}{2} + LJ \right], \tag{314}$$

which, when combined with the four equations of motion Eqs. (303)-(306), completely determine φ_1, φ_2, x_1 and x_2.

5.2.2 Voltage

The voltage across the device may again be taken along either of the two arms

$$V = \frac{\hbar}{2e} \frac{\mathrm{d}\varphi_1}{\mathrm{d}t} + B_1 l_1 \frac{\mathrm{d}x_1}{\mathrm{d}t} + L_1 \frac{\mathrm{d}I_1}{\mathrm{d}t} = \frac{\hbar}{2e} \frac{\mathrm{d}\varphi_2}{\mathrm{d}t} + B_2 l_2 \frac{\mathrm{d}x_2}{\mathrm{d}t} + L_2 \frac{\mathrm{d}I_2}{\mathrm{d}t}. \tag{315}$$

Interestingly, if we rearrange and integrate with respect to time, we obtain

$$\frac{\hbar}{2e}(\varphi_2 - \varphi_1) = B_1 x_1 l_1 - B_2 x_2 l_2 + L_1 I_1 - L_2 I_2 + \text{constant}, \tag{316}$$

which is simply the flux relation Eq. (314) with the constant of integration equal to the applied flux Φ. In symmetric form the voltage becomes

$$V = \frac{1}{2}\left[\frac{\hbar}{2e}\left(\frac{\mathrm{d}\varphi_1}{\mathrm{d}t} + \frac{\mathrm{d}\varphi_2}{\mathrm{d}t}\right) + (L_1 - L_2)\frac{\mathrm{d}J}{\mathrm{d}t} + B_1 l_1 \frac{\mathrm{d}x_1}{\mathrm{d}t} + B_2 l_2 \frac{\mathrm{d}x_2}{\mathrm{d}t}\right], \tag{317}$$

$$V = \frac{\hbar}{2e}\left(\frac{L_2}{L}\frac{\mathrm{d}\varphi_1}{\mathrm{d}t} + \frac{L_1}{L}\frac{\mathrm{d}\varphi_2}{\mathrm{d}t}\right) + \frac{L_2}{L}B_1 l_1 \frac{\mathrm{d}x_1}{\mathrm{d}t} + \frac{L_1}{L}B_2 l_2 \frac{\mathrm{d}x_2}{\mathrm{d}t}. \tag{318}$$

5.2.3 Dimensionless Equations

We can non-dimensionalize our mechanically coupled equations in a similar way as we did in the uncoupled case. We define the average junction length $l = (l_1 + l_2)/2$ and a combined mass $M = 2M_1M_2/(M_1 + M_2)$. This allows us to define dimensionless couplings $\mu_n = B_n/B_0$ and displacements $a_n = x_n/x_\mathrm{c}$ where $B_0 = (1/l)\sqrt{M/C}$ and $x_\mathrm{c} = B_0 I_\mathrm{c} l/M\omega_\mathrm{c}^2$. These are mostly the same parameters as in the single junction case, except that we use $x_\mathrm{c} \propto 1/\omega_\mathrm{c}^2$ rather than $x_0 \propto 1/\omega_0^2$. We also measure time in units of $\tau_\mathrm{c} = \omega_\mathrm{c} t$ and frequencies in units of ω_c as $\bar{\omega}_n = \omega_n/\omega_\mathrm{c}$. These modifications make analysing the case $\omega_1 \neq \omega_2$ easier. A more subtle modification is that, when defining a_n, we no longer remove the constant slack due to the constant force $B_0 I_\mathrm{DC} l_n/2$ that is present in both junctions. This is because, unlike in the single junction case, this slack has the physical consequence of increasing the flux through the SQUID by a constant amount.

With the above quantities defined we can write down our full set of dimensionless equations of motion as

$$\frac{i_\mathrm{DC}}{2} + j = (1-\alpha_I)\sin\varphi_1 + (1-\alpha_R)\dot{\varphi}_1 + (1-\alpha_c)[\beta_\mathrm{c}\ddot{\varphi}_1 + \mu_1(1-\alpha_l)\ddot{a}_1], \tag{319}$$

$$\frac{i_\mathrm{DC}}{2} - j = (1+\alpha_I)\sin\varphi_2 + (1+\alpha_R)\dot{\varphi}_2 + (1+\alpha_c)[\beta_\mathrm{c}\ddot{\varphi}_2 + \mu_2(1+\alpha_l)\ddot{a}_2], \tag{320}$$

$$\ddot{a}_1 + \frac{2\bar{\omega}_1}{Q_{\Gamma 1}}\dot{a}_1 + \bar{\omega}_1^2 a_1 = \mu_1(1-\alpha_l)(1-\alpha_M)[(1-\alpha_I)\sin\varphi_1 + (1-\alpha_R)\dot{\varphi}_1], \tag{321}$$

$$\ddot{a}_2 + \frac{2\bar{\omega}_2}{Q_{\Gamma 2}}\dot{a}_2 + \bar{\omega}_2^2 a_2 = \mu_2(1+\alpha_l)(1+\alpha_M)[(1+\alpha_I)\sin\varphi_2 + (1+\alpha_R)\dot{\varphi}_2], \tag{322}$$

$$\varphi_2 - \varphi_1 = 2\pi\phi + \pi\beta_L j + \frac{1}{\beta_\mathrm{c}}[(1-\alpha_l)\mu_1 a_1 - (1+\alpha_l)\mu_2 a_2], \tag{323}$$

where $\alpha_l = (l_2 - l_1)/(l_1 + l_2)$ and $\alpha_M = (M_1 - M_2)/(M_1 + M_2)$ characterise asymmetries in the junction lengths and effective masses. The voltage is similarly expressed

as

$$\frac{V}{I_c R} = \dot{\varphi}_1 + \frac{\pi\beta_L}{2}\dot{j} + \frac{\mu_1}{\beta_c}(1-\alpha_l)\dot{a_1} = \dot{\varphi}_2 - \frac{\pi\beta_L}{2}\dot{j} + \frac{\mu_2}{\beta_c}(1+\alpha_l)\dot{a_2}, \tag{324}$$

or in symmetric form,

$$\frac{V}{I_c R} = \frac{\dot{\varphi}_1 + \dot{\varphi}_2}{2} + \frac{1}{\beta_c}[(1-\alpha_l)\mu_1\dot{a_1} + (1+\alpha_l)\mu_2\dot{a_2}]. \tag{325}$$

Since $\langle\dot{a_1}\rangle = \langle\dot{a_2}\rangle = 0$, the extra contributions due to the mechanical oscillations have zero average so that they do not contribute directly to the measured DC voltage $\langle V\rangle$, just as we saw in the single junction case.

Eqs. (319)-(323) contain a very large number of free parameters in the general case where the junctions are non-identical so that it becomes challenging to draw any general conclusions. For simplicity when we move on to solve these equations we shall generally assume that the junctions are identical so that all the asymmetry parameters α_I etc. become zero. However we will allow the junctions to have distinct resonance frequencies ω_1, ω_2 and electromechanical couplings μ_1, μ_2.

A Lagrangian formulation for the coupled SQUID is presented in appendix B.

5.2.4 Single Junction Equivalence

We now move on to numerically solve our equations of motion (319)-(323). We will reduce the large number of free parameters by assuming identical junctions as usual so that $\alpha_I = \alpha_R = \alpha_C = \alpha_l = \alpha_M = 0$ and $Q_\Gamma = Q_{\Gamma 1} = Q_{\Gamma 2}$, $\bar{\omega}_0 = \bar{\omega}_1 = \bar{\omega}_2$, $\mu = \mu_1 = \mu_2$. The remaining free parameters are then i_{DC}, β_c, β_L, ϕ_a as in the uncoupled case but with the additional parameters μ, ω_0 and Q_Γ.

Just as we did in section 5.1.5 it is convenient to perform a change of variables to $\varphi_+ = (\varphi_1 + \varphi_2)/2$, $\varphi_- = (\varphi_1 - \varphi_2)/2$, $a_+ = (a_1 + a_2)/2$ and $a_- = (a_1 - a_2)/2$. The equations of motion can then be put in the form

$$\frac{i_{\mathrm{DC}}}{2} = \sin\varphi_+\cos\varphi_- + \dot{\varphi}_+ + \beta_c\ddot{\varphi}_+ + \mu\ddot{a_+}, \tag{326}$$

$$j = \sin\varphi_-\cos\varphi_+ + \dot{\varphi}_- + \beta_c\ddot{\varphi}_- + \mu\ddot{a_-}, \tag{327}$$

$$(1+\mu^2)\ddot{a_+} + \frac{2\bar{\omega}_0}{Q_\Gamma}\dot{a_+} + \bar{\omega}_0^2 a_+ = \mu(i_{\mathrm{DC}}/2 - \beta_c\ddot{\varphi}_+), \tag{328}$$

$$(1+\mu^2)\ddot{a_-} + \frac{2\bar{\omega}_0}{Q_\Gamma}\dot{a_-} + \bar{\omega}_0^2 a_- = \mu(j - \beta_c\ddot{\varphi}_-), \tag{329}$$

$$\varphi_- = -\pi(\phi_a + \beta_L j/2) - \frac{\mu}{\beta_c}a_-, \tag{330}$$

and the DC voltage is $\langle V\rangle/I_cR = \langle\dot{\varphi_+}\rangle$. We thus see immediately that the bias current i_{DC} is responsible for exciting the symmetric mode a_+ while the circulating current j is responsible for exciting the antisymmetric mode a_-. This is due to i_{DC} flowing in the same direction in both arms while j flows in opposite directions.

We will take the limit $\beta_L \ll 1$ since we already saw in the uncoupled case that the inclusion of inductance does not produce any qualitative differences, except for the existence of LC resonance steps. In the integer flux case $\phi_a = 0$, Eqs. (327), (329) and (330) are solved by $j = \varphi_- = a_- = 0$ while the remaining two equations become

$$\frac{i_{DC}}{2} = \sin\varphi_+ + \dot{\varphi_+} + \beta_c\ddot{\varphi_+} + \mu\ddot{a_+}, \tag{331}$$

$$(1+\mu^2)\ddot{a_+} + \frac{2\bar{\omega}_0}{Q_\Gamma}\dot{a_+} + \bar{\omega}_0^2 a_+ = \mu(i_{DC}/2 - \beta_c\ddot{\varphi_+}). \tag{332}$$

These are identical to the mechanically coupled single junction equations (140) and (141) except that the bias current is halved by splitting in the two junctions.[13] All the results of section 4 then follow, including all the mechanically induced Shapiro steps, hysteresis loops and retrappings. We now investigate how these results are modified when the applied magnetic flux differs from an integer number of flux quanta.

5.2.5 Effect of Magnetic Flux

We will solve Eqs. (326)-(330) numerically using the same experimentally realistic parameters that we used in the single junction case i.e. $\bar{\omega}_0 = 0.1$, $Q_\Gamma = 10^3$, $\beta_c = 200$ while the relevant dimenzsional scales are $I_cR = 3\mu$V, $B_0 = 10$T and $x_c = 0.1$pm. The bias current i_{DC} and in plane magnetic field $\mu = \mu_1 = \mu_2$ are directly controllable variables as usual, but we can now also vary the applied flux ϕ_a. We will begin with a decreasing current experiment as we did in section 4.6.1.

In Fig. 51 we compare the I-V curves for integer number of flux quanta, $\phi_a = 0$ [panel (a)], to those for half integer flux quanta, $\phi_a = 0.5$ [panel (c)]. The former case exactly emulates the results found in the single junction case as discussed above, while the latter case shows a strikingly different behaviour. The main differences arise due to the effective critical current I_c' approaching zero[14] as was discussed in

[13] The form of the equations are slightly modified due to the different dimensionless units discussed previously. Also note that $\bar{\omega}_0$ is just β_1, but the new notation is used for consistency with the non-symmetric case.

[14] The effective critical current is slightly greater than zero even for $\phi_a = 0.5$ due to the small amount of flux that enters the SQUID from the constant displacements [see Eq. (314)], but this is a very tiny correction unless the coupling reaches unrealistically large values.

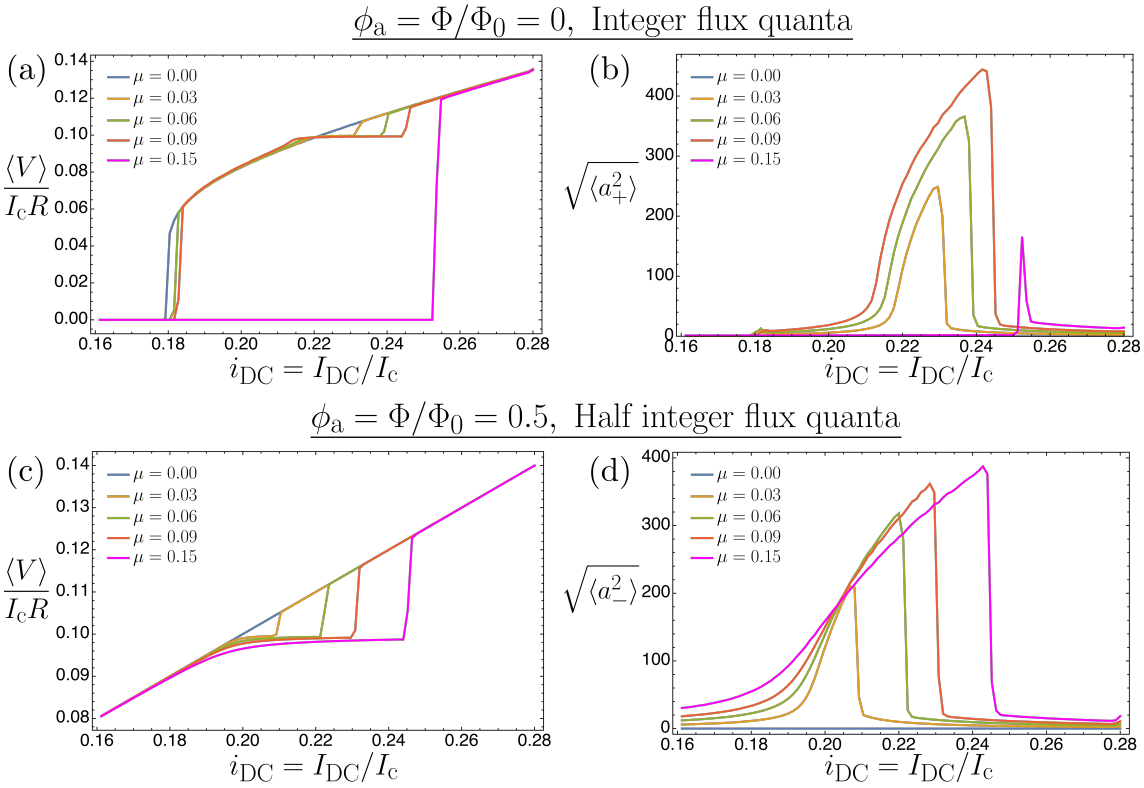

Figure 51: I-V curves and oscillator root mean square displacements on a decreasing current path calculated by numerically solving Eqs. (326)-(330) with the experimentally realistic parameters $\bar{\omega}_0 = 0.1$, $Q_\Gamma = 10^3$, $\beta_c = 200$, $\beta_L = 0$. Panels (a) and (b) show the results for integer flux quanta $\phi_a = 0$, which are equivalent to the single junction case, cf. Fig. 29. Panels (c) and (d) show the results for half integer flux quanta $\phi_a = 0.5$ which differ due to the vanishing effective critical current I_c'. The trapped state then no longer exists so that the plateau is stable for all coupling values. The case $\phi_a = 0$ is characterized by the excitation of the symmetric mode a_+ while the case $\phi_a = 0.5$ is characterized by the excitation of the antisymmetric mode a_-.

section 5.1.4. This means that the trapped state $\langle V \rangle = 0$ no longer exists for any current values. This is useful as one can reach much lower voltages without relying on the hysteresis of underdamped junctions as we had to in the single junction case. The sudden mechanically-induced retrappings also no longer exist since there is no state to become trapped to. For example consider the I-V curves for $\mu = 0.15$ (pink), when $\phi = 0$ [panel (a)] the system becomes retrapped as we decrease the current approaching the plateau whereas when $\phi = 0.5$ [panel (c)] no such retrapping occurs. This latter case thus results in larger voltage plateaus than are observed in the integer flux quanta or single junction case.

We can also study the oscillator displacements which again show very different behaviour in these two opposite cases. For $\phi_{\mathrm{a}} = 0$ the symmetric mode a_+ is strongly excited on the plateau state, as shown in panel (b), while the antisymmetric mode a_- is zero everywhere, as we argued in the previous subsection. In other words, for integer flux quanta the two oscillators are equally excited in phase $a_1 = a_2$ since the circulating current j is vanishingly small and the supercurrents in both arms flow in the same direction. In contrast, the case $\phi_{\mathrm{a}} = 0.5$ displays the opposite behaviour, with the antisymmetric mode a_- being strongly excited, as shown in panel (d). The symmetric mode a_+ is here zero except for a small constant value $\mu i_{\mathrm{DC}}/2\bar{\omega}_0^2$ which is negligible compared to a_- and results from the constant force $BI_{\mathrm{DC}}l/2$ acting on both resonators. Thus in this case the two oscillators are excited antisymmetrically $a_1 \approx -a_2$ due to a strong circulating current j and the supercurrents in both arms flowing in opposite directions.

An increasing current experiment can also be performed, using the mechanically induced hysteresis to access the full plateau width. Fig. (52) compares the I-V curves for $\phi_{\mathrm{a}} = 0$ [panel (a)], equivalent to the single junction, to those for $\phi_{\mathrm{a}} = 0.5$ [panel (c)]. In the former case we must first decrease the current to the plateau before increasing the current just as we did in section 4.6.2, but in the latter case we may increase the current directly from zero due to the vanishing critical current. Panel (c) shows that when $\phi_{\mathrm{a}} = 0.5$ one can explore the full extent of the Shapiro plateau without becoming retrapped, reaching widths in excess of I_{c}. The plateau size asymptotes to a maximum value at a finite coupling, although for the parameters chosen here this occurs at unrealistically large magnetic fields. The regimes $\phi_{\mathrm{a}} = 0$ and $\phi_{\mathrm{a}} = 0.5$ are again characterized by resonances of the symmetric mode a_+ [panel (b)] and of the antisymmetric mode a_- [panel (d)], respectively.

If we fix i_{DC} and μ such that we are in a stable plateau state, we can thus controllably switch between exciting the modes a_+ or a_- simply by varying the applied flux. This behaviour is illustrated in Fig. 53 where we choose $i_{\mathrm{DC}} = 0.22$,

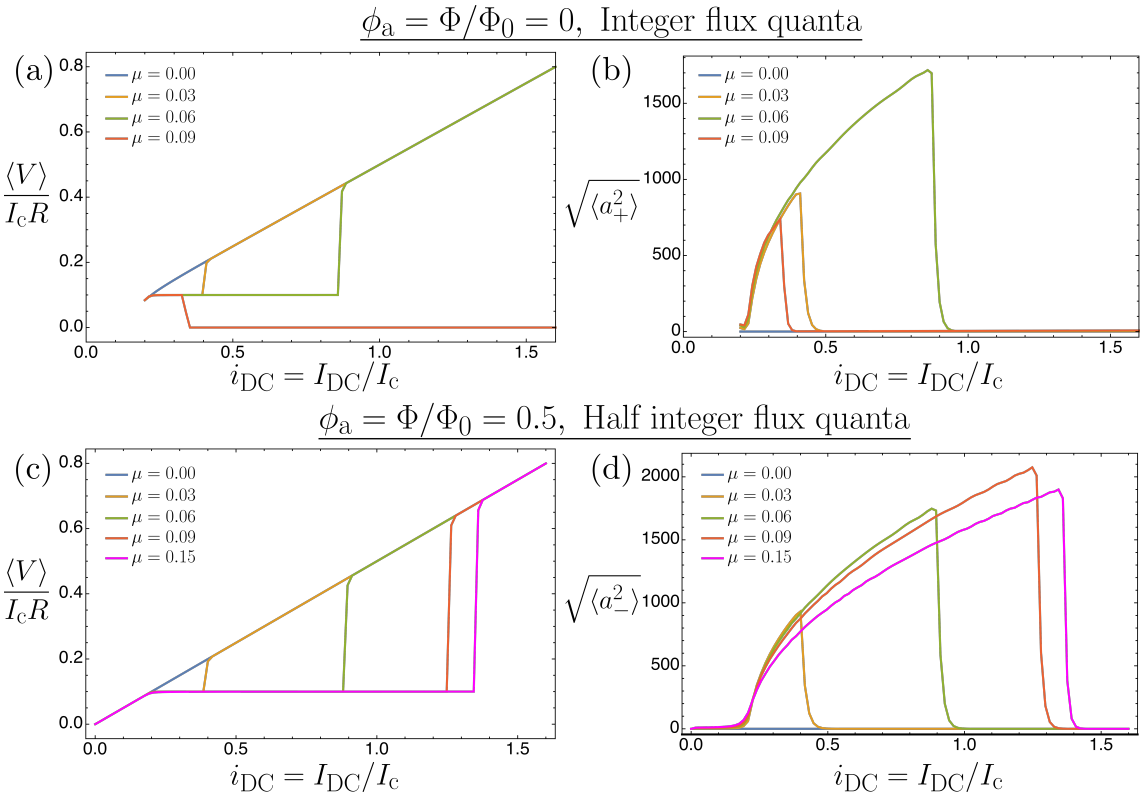

Figure 52: I-V curves and oscillator root mean square displacements on an increasing current path calculated by numerically solving Eqs. (326)-(330) with the same parameters as in Fig. 51. Panels (a) and (b) show results for $\phi_a = 0$, again equivalent to the single junction case cf. Fig. 32, while panels (c) and (d) show results for $\phi_a = 0.5$. One sees much of the same behaviour as the decreasing current path Fig. 51 except that here much larger plateaus are accessed by exploiting the mechanically induced hysteresis. The fact that retrapping does not occur for $\phi_a = 0.5$ means that we can obtain very large plateaus with widths greater than I_c.

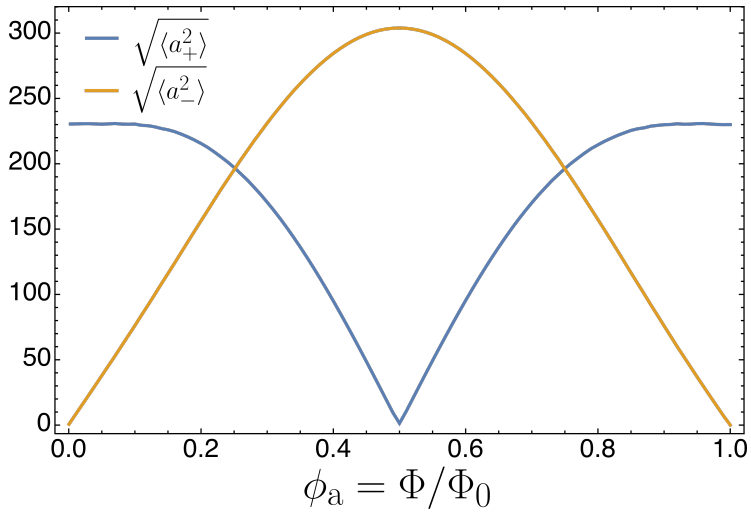

Figure 53: Simulation with varying external flux ϕ_a for fixed current, $i_{DC} = 0.22$, and coupling, $\mu = 0.09$. The system is in a stable plateau state so that mechanical oscillations are excited, but whether these oscillations are excited symmetrically $a_+ = (a_1+a_2)/2$ or antisymmetrically $a_- = (a_1-a_2)/2$ is flux dependent. When $\phi_a = 0$, or more generally an integer, there is no circulating current and the supercurrents in both arms flow in the same direction so that the oscillator is excited symmetrically. In contrast when $\phi_a = 0.5$, or half integer, the circulating current is strong and the supercurrents flow in opposite directions so that the antisymmetric mode is excited.

$\mu = 0.09$ and access the plateau $\langle V \rangle / I_c R \approx \bar{\omega}_0 = 0.1$. The same experiment can be performed at stronger coupling, choosing i_{DC} and μ such that the plateau is unstable for $\phi_a = 0$ but stable for $\phi_a = 0.5$. In this way one can switch between the trapped and plateau states. The results of such an experiment for $i_{DC} = 0.22$ and $\mu = 0.3$ are shown in Fig. 54. Around $\phi_a = 0$ we are in a region where the plateau is unstable so that the system is trapped $\langle V \rangle = 0$. As we then approach $\phi_a = 0.5$ the trapped state vanishes when I_c' becomes less than I_{DC} and the system makes a discrete jump to the plateau state $\langle V \rangle / I_{DC} R \approx \bar{\omega}_0 = 0.1$ which is now stable. In between these two extremes however there is a multistable region where the plateau is stable but the trapped state still exists. Which state the system enters then becomes history dependent, forming the hysteresis pattern depicted in Fig. 54, with the blue and orange lines showing increasing and decreasing flux paths respectively. This multistable region decreases in size as μ increases and more plateau states become unstable.

5.2.6 Double Steps

Up until now we have assumed that the resonance frequencies of both weak links ω_1 and ω_2 are identical, but we will now briefly explore what happens if they are

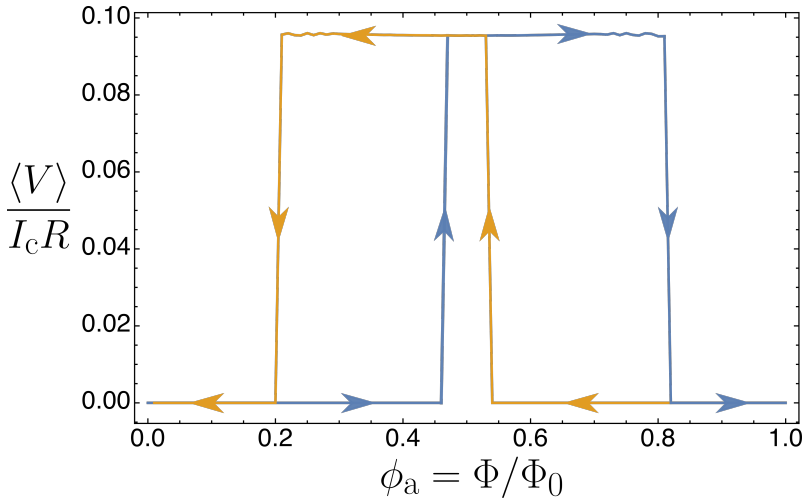

Figure 54: Simulation with varying external flux ϕ_a for fixed current, $i_{DC} = 0.22$, and coupling, $\mu = 0.3$. Here the coupling is large enough that the plateau is unstable when $\phi_a = 0$ and the system is trapped. Increasing the flux to $\phi_a = 0.5$ then forces the system to make a discrete jump to the mechanically resonant plateau state since the trapped state vanishes as $I_c' < I_{DC}$. A multistable region is present where the trapped state exists and the plateau is stable. This multistability leads to the hysteresis pattern shown, with the blue and orange lines corresponding to increasing and decreasing flux respectively.

different. Fig. 55 shows possible I-V curves calculated numerically when $\bar{\omega}_1 = 0.1$, $\bar{\omega}_2 = 0.15$, $\mu = 0.09$, $\phi_a = 0$. The other parameters are the same as we have used previously, $\beta_c = 200$, $Q = 10^3$ and $\beta_L = 0$. As one might expect, instead of a single Shapiro plateau, there are now two plateaus appearing at the frequencies ω_1 and ω_2. On the ω_1 step, the oscillator a_1 is in resonance while on the ω_2 step a_2 is in resonance. The I-V curve is as usual strongly hysteretic and by increasing the current from different starting points we can explore the full width of either of the two steps. The full hysteresis profile is highlighted by the various arrows in Fig. 55. We see that in some regions there are four possible stable solutions for the same current value, a trapped state at $\langle V \rangle = 0$, a non-resonant running state $\langle V \rangle \approx I_{DC}R$ and two resonant plateau states $\langle V \rangle / I_c R = \bar{\omega}_1$ and $\langle V \rangle / I_c R = \bar{\omega}_2$. Thus by varying the current we can choose to excite either of the two oscillators a_1 or a_2.

For larger couplings, the Shapiro steps exhibit energy-induced retrappings, and are each associated with their own critical coupling values. This produces a large number of additional transitions that are not displayed in Fig. 55. If ϕ_a is not an integer value there is of course also different behaviour in the same way as we discussed in the equal frequency case, in particular the aforementioned retrappings do not occur.

We have now analyzed DC SQUIDs whose two constituent weak links can me-

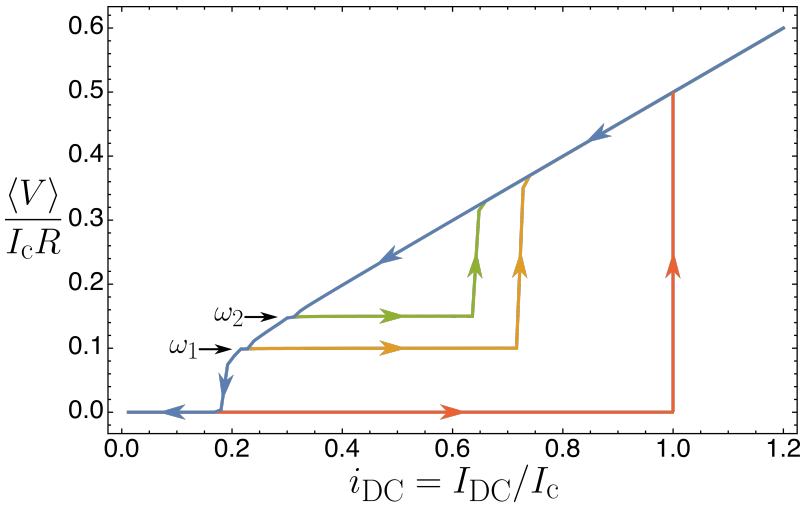

Figure 55: Possible I-V curves of an electromechanically coupled SQUID whose arms have distinct resonance frequencies $\bar{\omega}_1 = 0.1$ and $\bar{\omega}_2 = 0.15$. The other parameters are $\mu = 0.09$, $\phi_a = 0$, $\beta_c = 200$, $Q_\Gamma = 10^3$ and $\beta_L = 0$. Two distinct plateaus are present at the frequencies ω_1 and ω_2. The I-V curves are highly hysteretic, with each line corresponding to different possible paths and the arrows indicating whether the bias current is increased or decreased. In particular by increasing the current from different starting points we can explore the full width of either of the two steps. On the ω_1 step the oscillator a_1 is in resonance while on the ω_2 step the oscillator a_2 is in resonance.

chanically oscillate under the application of DC currents and magnetic fields. This forms a natural extension of the electromechanically coupled single junction discussed in the previous section, where the external flux through the loop becomes an important new parameter. We have seen that varying this external flux allows one to control whether we activate the symmetric mode a_+ or antisymmetric mode a_-. In addition, in the strong coupling regime we can make discrete transitions from a zero voltage state to a mechanically resonant one at finite voltage, while keeping the bias current and coupling fixed. This large increase/decrease in voltage over a very small range of flux could be useful for ultra high-precision magnetometers. The Josephson junctions in this set up do not necessarily need to be underdamped, since we can reach much lower voltages by reducing the effective critical current, and the induced circulating current can provide the electronic AC current. The requirement to reduce thermal noise in our device still remains however, with temperatures still needing to be reduced below 100mK, as discussed in section 4.11.

In principle a full analytical treatment of the electromechanically coupled SQUID is possible using an ansatz similar to Eqs. (170) and (168) although the sheer number of parameters in the general case makes it a challenging problem.

6 Josephson Bloch Oscillations

When subjected to a constant and uniform electric field, electrons in solids may undergo periodic motions known as Bloch oscillations [80]. These oscillations can be revealed either by the transport properties of the solid [81,82] or by the radiation generated by them [83]. One of the most practical aspects of Bloch oscillations is that they can be used to amplify radiation in the terahertz range [84].

Bloch oscillations are not exclusive to solids. In their pioneering work, Likharev *et al.* showed [85–88] that the dynamics of a Josephson junction was formally equivalent to that of an electron moving in a one-dimensional solid. As such, Bloch oscillations also occur in these junctions when driven by a DC current, which plays an analogous role to the constant uniform electric field that induces ordinary electronic Bloch oscillations. Bloch oscillations in a Josephson junction can be revealed in its I-V characteristic in the presence of a probing AC current [89, 90].

In this chapter we will begin by discussing the theory of Josephson Bloch oscillations before moving on to consider how they may be coupled to mechanical oscillations in the weak link. We will consider the same mechanically coupled single junction set up that was considered in chapter 4, but in a regime where Bloch oscillations dominate with respect to the usual Josephson oscillations. We will see that these Bloch oscillations, induced only by a DC current and uniform magnetic field, can excite nano-scale mechanical vibrations that may be detected in the junction's DC I-V characteristic. This could provide a novel way of observing the Bloch oscillations without the need of an AC current, as well as producing non-classical mechanical states that are intimately coupled with the quantum dynamics in the junction.

6.1 Likharev Theory

The following Hamiltonian describes a Josephson junction biased with a current I_{DC}

$$\hat{H} = \frac{\hat{Q}^2}{2C} - \frac{\hbar I_c}{2e}\cos\hat{\varphi} + \frac{\hbar}{2e}(\hat{I}_q - I_{\mathrm{DC}})\hat{\varphi} + \hat{H}_q, \tag{333}$$

where symbols have their usual meanings. In contrast to the previous chapters, dissipation has now been included directly by introducing $\hat{I}_q$, the normal current carried by thermally excited quasiparticles, which serve as a heat bath for the Cooper pair condensate, and $\hat{H}_q$, the Hamiltonian describing these quasiparticles. Recall that $\hat{H}$ is identical in form to the Hamiltonian for a particle in the 'tilted washboard' potential $U(\varphi) = -\hbar(I_{\mathrm{c}}\cos\varphi + I_{\mathrm{DC}}\varphi)/2e$ (see section 3.3.1), except for the coupling to the quasiparticle current that generates damping. We saw that around the local

minima, this potential can be approximated as harmonic with a frequency $\omega_{\rm p} = (2eI_{\rm c}/\hbar C)^{1/2}$, when $I_{\rm DC} \ll I_{\rm c}$. In quantum mechanical terms, we thus expect the first few energy levels of $\hat{H}$ to be separated by a spacing $\hbar\omega_{\rm p}$. When the Josephson energy $E_{\rm J} = \hbar I_{\rm c}/2e$ is much larger than this energy spacing, $E_{\rm J} \gg \hbar\omega_p$, we can neglect the quantum nature of φ and treat it as a classical variable, as has been done throughout the preceding chapters. However in the opposite limit, we must treat the system quantum mechanically. It is in this limit that the Bloch oscillations dominate with respect to the much faster, lower amplitude, Josephson oscillations.

To continue we must then treat the system parameters as quantum mechanical operators, in particular $\hat{\varphi}$ and $\hat{Q}$ must satisfy the canonical commutation relation $[\hat{\varphi}, \hat{Q}/2e] = i$. The first two terms of Eq. (333) make up the bare Hamiltonian $\hat{H}_0$ in the absence of currents. In the coordinate representation this becomes

$$\hat{H}_0 = -4E_C \frac{\partial^2}{\partial\varphi^2} - E_{\rm J}\cos\hat{\varphi}, \tag{334}$$

where we have expressed the charge operator as $\hat{Q} = -2ei\,\partial/\partial\varphi$ and substituted the Josephson energy $E_{\rm J} = \hbar I_{\rm c}/2e$ and the charging energy $E_C = e^2/2C$. The Schrödinger equation is then identical to that of a particle in the periodic potential $-E_{\rm J}\cos\varphi$, so that the solutions are Bloch waves. The energy dispersion is thus a series of energy bands with a periodic dependence within each band i.e.

$$E_n(q) = E_n(q + 2e), \tag{335}$$

where $n = 0, 1, 2...$ is the band index and q is the quasicharge, which differs from the real charge Q in the same way that quasimomentum differs from real momentum in a crystal lattice. We will consider the low temperature $k_{\rm B}T \ll \hbar\omega_{\rm p}$, and low current $\hbar I_{\rm DC}/2e \ll \hbar\omega_{\rm p}$, limits where Zener transitions to higher energy bands have low probability and we can restrict our analysis to the lowest energy band $E(q) = E_0(q)$. Also in this limit, we can perform a semiclassical analysis, treating the currents as small perturbations to $\hat{H}_0$.

We then proceed by analogy with the semiclassical model of electron transport, with the current $I_{\rm DC}$ playing the role of an applied electric field. In what follows we will use unhatted symbols to represent quantum mechanical state averages of the corresponding operators, while angle brackets will be reserved for time averages as usual. The time derivative of φ is then given by the group velocity

$$\frac{{\rm d}\varphi}{{\rm d}t} = \frac{2e}{\hbar}\frac{\partial E(q)}{\partial q}, \tag{336}$$

from which we identify the voltage as

$$V = \frac{Q}{C} = \frac{\partial E(q)}{\partial q}. \tag{337}$$

In the electron transport analogy, the term $(\hat{I}_q - I_{\mathrm{DC}})\hat{\varphi}$ appearing in the Hamiltonian Eq. (333) acts as an effective electronic scalar potential, so that the quasicharge q evolves due to the following applied force

$$\frac{\mathrm{d}q}{\mathrm{d}t} = I_{\mathrm{DC}} - I_q. \tag{338}$$

The expectation value I_q should be determined in a self-consistent way by solving the Heisenberg equations for I_q and H_q, but if the superconducting gaps of the electrodes are much larger than E_{J} it takes the simple form

$$I_q = \frac{V}{R} = \frac{1}{R}\frac{\partial E(q)}{\partial q}, \tag{339}$$

where R is the normal state resistance, in accordance with the RCSJ model. Inserting this into Eq. (338) we obtain the main equation that describes the dynamics of the system.

$$\frac{\mathrm{d}q}{\mathrm{d}t} = I_{\mathrm{DC}} - \frac{1}{R}\frac{\partial E(q)}{\partial q}. \tag{340}$$

When the energy dispersion $E(q)$ is specified, this equation may be solved for the evolution of the quasicharge $q(t)$. The evolution of the voltage is then determined from Eq. (337).

If I_{DC} is smaller than the following threshold value

$$I_{\mathrm{t}} = \max\left(\frac{\partial E(q)}{\partial q}\right)/R, \tag{341}$$

then there is a stationary solution $\dot{q} = 0$ which yields an Ohmic voltage $V = I_{\mathrm{DC}}R$. However, if the DC current is larger than this threshold current, $q(t)$ evolves in time producing oscillations in voltage and energy. These oscillations are a direct analogue of Bloch oscillations. Their time period t_{B} may be calculated by integrating Eq. (340), producing

$$q(t_{\mathrm{B}}) - q(0) = I_{\mathrm{DC}}t_{\mathrm{B}} - \frac{1}{R}\int_0^{t_{\mathrm{B}}} V(q(t))dt. \tag{342}$$

The energy and voltage are periodic in q with period $2e$ so the time period is the time needed for q to increase by $2e$ i.e. $q(t_{\mathrm{B}}) - q(0) = 2e$. Defining the average

voltage as $\langle V \rangle$ we then obtain the frequency as

$$\omega_{\mathrm{B}} = \frac{2\pi}{t_{\mathrm{B}}} = \frac{\pi}{e}\left(I_{\mathrm{DC}} - \frac{1}{R}\langle V \rangle\right). \tag{343}$$

To continue we must specify the energy dispersion $E(q)$. In the limit $E_{\mathrm{J}} \gg E_{\mathrm{C}}$ the potential can be approximated as a series of deep wells so one can use a tight-binding approach.[15] The energy dispersion is then well known, with the lowest band being

$$E(q) = \frac{\Omega_0}{2}\left(1 - \cos(\pi q/e)\right), \tag{344}$$

where Ω_0 is the band width given by

$$\frac{\Omega_0}{E_J} = 16\sqrt{\frac{2}{\pi}}\exp\left(-\sqrt{\frac{8E_J}{E_C}}\right). \tag{345}$$

The equation of motion (340) is then

$$\frac{\mathrm{d}q}{\mathrm{d}t} = I_{\mathrm{DC}} - I_{\mathrm{t}}\sin\left(\frac{\pi q}{e}\right), \tag{346}$$

where the threshold current is $I_{\mathrm{t}} = \pi\Omega_0/2eR$. For ease of calculation we can write these equations in dimensionless form as usual. The current will now be expressed in units of the threshold current by redefining $i_{\mathrm{DC}} = I_{\mathrm{DC}}/I_{\mathrm{t}}$. Time is measured in units of $\tau_{\mathrm{t}} = \omega_{\mathrm{t}}t$, where $\omega_{\mathrm{t}} = \pi I_{\mathrm{t}}/e$ is the Bloch frequency ω_{B} at the threshold current, in the absence of damping. The quasicharge q is conveniently expressed as $\bar{q} = q/q_0$ where $q_0 = e/\pi$ so that the voltage is $V/I_{\mathrm{t}}R = \sin\bar{q}$. Eq. (346) then becomes

$$\dot{\bar{q}} = i_{\mathrm{DC}} - \sin\bar{q}, \tag{347}$$

where a dot over a quantity now denotes a derivative with respect to $\tau_{\mathrm{t}} = \omega_{\mathrm{t}}t$.

This equation can now be solved numerically for $\bar{q}(t)$, and the DC voltage obtained by taking the time average $\langle V \rangle/I_{\mathrm{t}}R = \langle \sin\bar{q}(t) \rangle$. This produces the I-V curve displayed in Fig. 56(a). The regime $I_{\mathrm{DC}} \leq I_{\mathrm{t}}$ is Ohmic $\langle V \rangle = I_{\mathrm{DC}}R$ (blue line), while the oscillatory regime, $I_{\mathrm{DC}} > I_{\mathrm{t}}$, is characterized by a region with negative differential resistance $\mathrm{d}\langle V \rangle/\mathrm{d}I_{\mathrm{DC}} < 0$ (orange line). Panel (b) displays a plot of the energy dispersion $E(q)$, highlighting the evolution of q in time. Below the threshold current q is constant giving a definite energy and voltage, while above the threshold

[15] In the opposite limit $E_C \gg E_{\mathrm{J}}$, the potential is weak so the energy dispersion within the first Brillouin zone is approximately parabolic $q^2/2C$. Bloch oscillations also arise in this limit with little qualitative difference, except that the analysis is more difficult [90].

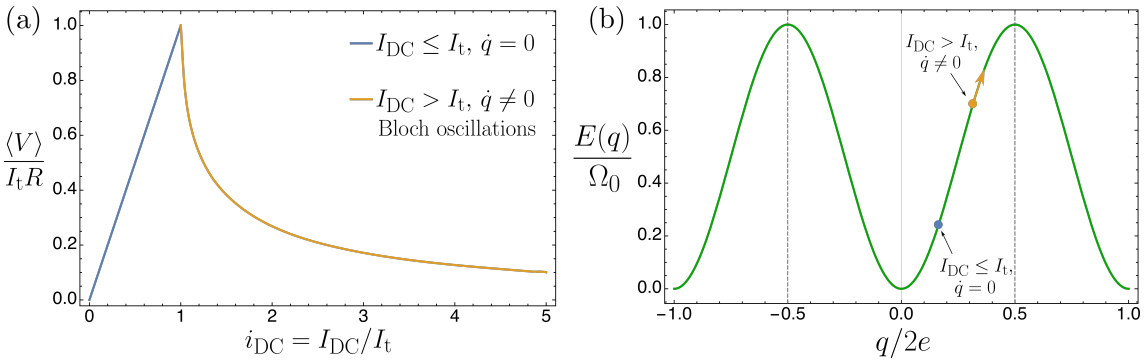

Figure 56: (a) I-V curve obtained from solving Eq. (347). When the DC bias current I_{DC} is less than the threshold current I_t, the DC voltage is Ohmic (blue line) and there are no Bloch oscillations. In contrast, when $I_{DC} > I_t$ there is negative differential resistance $d\langle V\rangle/dI_{DC} < 0$ (orange line) which signals the existence of Bloch oscillations. (b) Energy dispersion $E(q)$ of the lowest energy band, given by Eq. (344). Dashed lines show the boundary of the first Brillouin zone, while the blue and orange dots show the behaviour of q in the two current regimes.

current the quasicharge increases with time, producing oscillations in the energy and voltage.

One may also include an AC current $I_{AC}\sin(\omega_{AC}t)$ on top of I_{DC}, just as we did in the classical limit in section 3.5. Eq. (347) then becomes

$$\dot{\bar{q}} = i_{DC} + i_{AC}\sin(\bar{\omega}_{AC}\tau_t) - \sin\bar{q}, \tag{348}$$

where $i_{AC} = I_{AC}/I_t$ and $\bar{\omega}_{AC} = \omega_{AC}/\omega_t$. The I-V curve obtained in this case is shown in Fig. 57(a) from which we see that the oscillatory region now contains Ohmic branches where the Bloch frequency locks to harmonics or subharmonics of the driving frequency, $\omega_B = (n/m)\,\omega_{AC}$. The fact that this coupling leads to Ohmic branches rather than flat Shapiro plateaus can be readily seen by the fact that ω_B, as defined in Eq. (343), is proportional to $I_{DC} - \langle V\rangle/R$ rather than $\langle V\rangle$ directly. A plot of ω_B as a function of a current is displayed in panel (b), where the frequency locking is easily visible. It was by measuring this frequency locking under the application of an AC current bias that Bloch oscillations were first observed in Josephson junctions [89].

6.2 Bloch-Mechanical Coupling

We now attempt to couple these Bloch oscillations to mechanical vibrations, just as we did with the Josephson oscillations in the classical limit. We use an identical set up to the one used previously, which is extensively discussed in chapter 4 and

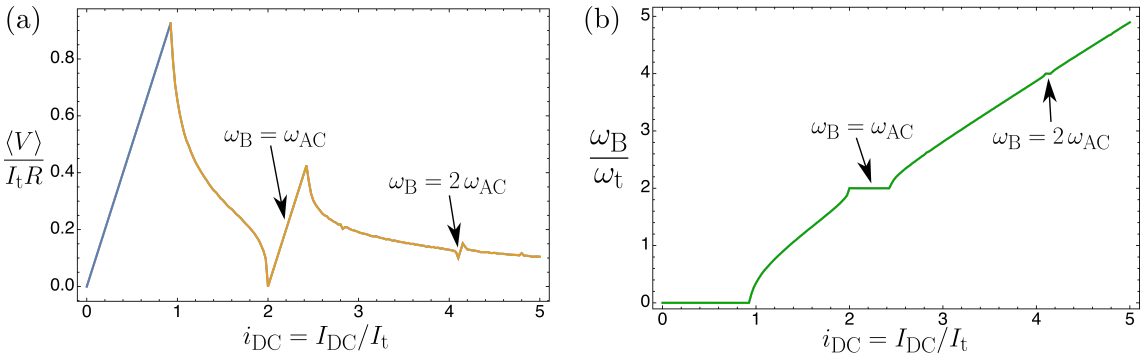

Figure 57: (a) I-V curve obtained from solving Eq. (348) where the bias current contains an AC component with amplitude $I_{AC}/I_t = 1$ and frequency $\bar{\omega}_{AC} = \omega_{AC}/\omega_t = 2$. Two additional Ohmic branches are clearly visible in the region $I_{DC} > I_t$, where the Bloch oscillation frequency locks to multiples of the bias frequency ω_{AC}. This frequency locking is more visible in panel (b) which shows a plot of the Bloch oscillation frequency directly, $\omega_B/\omega_t = i_{DC} - \langle V\rangle/I_t R$.

displayed in Fig. 15. The Josephson weak link is now suspended and allowed to oscillate due to the application of an in-plane magnetic field B. The mechanical oscillations have their usual effect on the electronic system, leading to an effective AC bias current flowing through the weak link. However, instead of forming Shapiro plateaus in the I-V curve, the oscillations are expected to produce Ohmic branches as discussed above.

6.2.1 Coupled Hamiltonian

The following Lagrangian and Hamiltonian for this coupled system were derived in sections 4.4 and 4.5.

$$\mathcal{L} = \frac{1}{2}C\left(\frac{\hbar}{2e}\frac{\mathrm{d}\varphi}{\mathrm{d}t} + Bl\frac{\mathrm{d}x}{\mathrm{d}t}\right)^2 + E_J\cos\varphi + \frac{\hbar}{2e}I_{DC}\varphi + \frac{1}{2}M\left(\frac{\mathrm{d}x}{\mathrm{d}t}\right)^2 - \frac{1}{2}M\omega_0^2x^2 + BI_{DC}lx, \tag{349}$$

$$H = \frac{1}{2}C\left(\frac{\hbar}{2e}\frac{\mathrm{d}\varphi}{\mathrm{d}t} + Bl\frac{\mathrm{d}x}{\mathrm{d}t}\right)^2 - E_J\cos\varphi - \frac{\hbar}{2e}I_{DC}\varphi + \frac{1}{2}M\left(\frac{\mathrm{d}x}{\mathrm{d}t}\right)^2 + \frac{1}{2}M\omega_0^2x^2 - BI_{DC}lx, \tag{350}$$

where symbols have their usual meanings and damping has not yet been included. In order to treat this Hamiltonian quantum mechanically we must of course write it in traditional form in terms of the canonical momenta of the variables φ and x. Instead of φ we will find it is more convenient to perform a change of variables and use $s = \hbar\varphi/2e$ since its conjugate momentum is equal to the charge Q. These

conjugate momenta are then

$$p = \frac{\partial \mathcal{L}}{\partial(\mathrm{d}x/\mathrm{d}t)} = (M + CB^2l^2)\frac{\mathrm{d}x}{\mathrm{d}t} + CBl\frac{\mathrm{d}s}{\mathrm{d}t}, \tag{351}$$

$$Q = \frac{\partial \mathcal{L}}{\partial(\mathrm{d}s/\mathrm{d}t)} = C\left(\frac{\mathrm{d}s}{\mathrm{d}t} + Bl\frac{\mathrm{d}x}{\mathrm{d}t}\right), \tag{352}$$

so that the two commutation relations both take the canonical form $[x, p] = i\hbar$ and $[s, Q] = i\hbar$. In terms of these momenta the Hamiltonian is

$$\hat{H} = \frac{1}{2\widetilde{C}}\left(Q - \frac{\tilde{C}Bl}{M}p\right)^2 - E_J\cos(2es/\hbar) - I_{\mathrm{DC}}s + \frac{p^2}{2\tilde{M}} + \frac{1}{2}M\omega_0^2x^2 - BI_{\mathrm{DC}}lx, \tag{353}$$

where for convenience we have defined a renormalized capacitance $\tilde{C} = C/(1+\mu^2)$ and mass $\tilde{M} = M(1+\mu^2)$, and μ has the usual definition $\mu = B/B_0$ with $B_0 = \sqrt{MC^{-1}}/l$. We can now proceed with quantization and add explicitly terms that produce both the electronic and mechanical damping as follows

$$\begin{aligned}\hat{H} = \frac{1}{2\widetilde{C}}\left(\hat{Q} - \frac{\tilde{C}Bl}{M}\hat{p}\right)^2 - E_J\cos(2e\hat{s}/\hbar) + (\hat{I}_q - I_{\mathrm{DC}})\hat{s} + \hat{H}_q \\ + \frac{\hat{p}^2}{2\tilde{M}} + \frac{1}{2}M\omega_0^2\hat{x}^2 - BI_{\mathrm{DC}}l\hat{x} + \hat{H}_b + \hat{H}_i.\end{aligned} \tag{354}$$

Here $\hat{H}_q$ and $\hat{I}_q$ produce the electronic damping as before, but we have also introduced

$$\hat{H}_b = \sum_\omega \hbar\omega(\hat{b}_\omega^\dagger\hat{b}_\omega + 1/2), \tag{355}$$

which models a mechanical heat bath consisting of a spectrum of harmonic oscillators and

$$\hat{H}_i = \sum_\omega \hbar\lambda_\omega(\hat{a}\hat{b}_\omega^\dagger + \hat{a}^\dagger\hat{b}_\omega) \tag{356}$$

which describes the coupling to this bath. The operators $\hat{b}_\omega$, $\hat{b}_\omega^\dagger$ are the annihilation and creation operators for the heat bath oscillators, while $\hat{a}$ and $\hat{a}^\dagger$ are those for the resonator, yielding $\hat{x} = \sqrt{\frac{\hbar}{2M\omega_0}}(\hat{a} + \hat{a}^\dagger)$ and $\hat{p} = i\sqrt{\frac{\hbar M\omega_0}{2}}(\hat{a}^\dagger - \hat{a})$. The vibron number operator is given by $\hat{n} = a^\dagger a$. The parameters λ_ω are chosen by assuming a white noise distribution for the heat bath, i.e.

$$\sum_\omega \lambda_\omega^2 e^{i\omega(t-t')} = \Gamma_0\delta(t-t'), \tag{357}$$

so that the interaction with the heat bath will lead to the usual velocity dependent damping.

Mathematically, the Hamiltonian Eq. (354) resembles that of an ordinary electronic Bloch oscillator placed in a single mode optical cavity with frequency ω_0. The current $\hat{I}_q - I_{\mathrm{DC}}$ acts as an electronic scalar potential as it did previously, but the mechanical resonator also introduces an effective vector potential proportional to $\hat{p}$. It is through this term that $\hat{Q}$ and $\hat{p}$ are coupled, with the coupling strength $\tilde{C}Bl/M$ being tunable by the field B. Thus, by again employing the analogy with electron transport, the particle velocity $\mathrm{d}s/\mathrm{d}t$ is still given by the group velocity as

$$\frac{\mathrm{d}s}{\mathrm{d}t} = \frac{\hbar}{2e}\frac{\mathrm{d}\varphi}{\mathrm{d}t} = \frac{\partial E}{\partial q}. \tag{358}$$

The voltage however is proportional to the charge Q so that

$$V = \frac{Q}{C} = \frac{\partial E}{\partial q} + Bl\frac{\mathrm{d}x}{\mathrm{d}t} = \frac{1}{1+\mu^2}\frac{\partial E}{\partial q} + \frac{Bl}{\tilde{M}}p, \tag{359}$$

where we have used Eqs. (351) and (352) to write this in terms of momenta. However, since the resonator velocity $\mathrm{d}x/\mathrm{d}t$ has zero time average, the DC voltage is still given by the simple expression

$$\langle V \rangle = \left\langle \frac{\partial E}{\partial q} \right\rangle. \tag{360}$$

Just like the uncoupled case, there is an effective force $I_{\mathrm{DC}} - I_q$ due to the gradient of the scalar potential but now there is an additional component from the time derivative of the effective vector potential $\tilde{C}Blp/M$. The time evolution of q is then given by

$$\frac{\mathrm{d}q}{\mathrm{d}t} = I_{\mathrm{DC}} - I_q - \frac{\tilde{C}Bl}{M}\dot{p}. \tag{361}$$

We can again include electronic dissipation by assuming that the expectation value of the quasiparticle current takes the classical form

$$I_q = \frac{1}{R}\left(V - Bl\frac{\mathrm{d}x}{\mathrm{d}t}\right) = \frac{1}{R}\frac{\partial E}{\partial q}. \tag{362}$$

We must now find how the mechanical resonator evolves in time. This can be achieved by writing down the Heisenberg equations of motion for the operators $\hat{x}$

and $\hat{p}$ as follows

$$\frac{\mathrm{d}\hat{x}}{\mathrm{d}t} = \frac{i}{\hbar}[\hat{H}, \hat{x}] = \frac{\hat{p} - CBl\,\partial E/\partial q}{\tilde{M}}, \tag{363}$$

$$\frac{\mathrm{d}\hat{p}}{\mathrm{d}t} = \frac{i}{\hbar}[\hat{H}, \hat{p}] = BI_{\mathrm{DC}}l - M\omega_0^2\hat{x} - 2M\Gamma_0\frac{\mathrm{d}\hat{x}}{\mathrm{d}t}. \tag{364}$$

The first of these equations follows directly from the definition of p from Eq. (351). By taking quantum mechanical state averages these equations transform simply into ones for the expectation values x and p. Inserting p from Eq. (363) into Eq. (364) one then obtains the following second order differential equation for x

$$M\frac{\mathrm{d}^2x}{\mathrm{d}t^2} + 2M\Gamma_0\frac{\mathrm{d}x}{\mathrm{d}t} + M\omega_0^2x = Bl\left(I_{\mathrm{DC}} - \frac{\mathrm{d}Q}{\mathrm{d}t}\right), \tag{365}$$

which is identical in form to the classical equation obtained in chapter 4 [cf. Eq. (138)]. If we write Q in terms of q using Eq. (359) this equation becomes

$$(1+\mu^2)\frac{\mathrm{d}^2x}{\mathrm{d}t^2} + 2\Gamma_0\frac{\mathrm{d}x}{\mathrm{d}t} + \omega_0^2x = \frac{Bl}{M}\left(I_{\mathrm{DC}} - C\frac{\partial^2 E}{\partial q^2}\frac{\mathrm{d}q}{\mathrm{d}t}\right), \tag{366}$$

which when combined with the equation for the evolution of q

$$\frac{\mathrm{d}q}{\mathrm{d}t} = I_{\mathrm{DC}} - \frac{1}{R}\frac{\partial E}{\partial q} - \frac{\tilde{C}Bl}{M}\dot{p}, \tag{367}$$

completely determine the evolution of x, p and q.

We could immediately solve these equations and produce I-V curves and plots of the root mean square displacement. However, as the mechanical vibration amplitude turns out to be of the order of zero-point motion amplitude, $x_{\mathrm{zp}} = \sqrt{\hbar/2M\omega_0}$, it is desirable to also characterize the resonator by the evolution of the vibron number $\hat{n} = \hat{a}^\dagger\hat{a}$, or more precisely, its expectation value $n(t)$.

6.2.2 Vibron Evolution

We begin by finding how the creation and annihilation operators $\hat{a}^\dagger$ and $\hat{a}$ evolve from the Heisenberg equation of motion, yielding

$$\frac{\mathrm{d}\hat{a}}{\mathrm{d}t} = \frac{i}{\hbar}[\hat{H}, \hat{a}] = -i\omega_0\hat{a} - BlQ\sqrt{\frac{\omega_0}{2\hbar M}} + i\frac{BI_{\mathrm{DC}}l}{\sqrt{2M\hbar\omega_0}} - \Gamma_0\hat{a} + \hat{F}, \tag{368}$$

$$\frac{\mathrm{d}\hat{a}^\dagger}{\mathrm{d}t} = \frac{i}{\hbar}[\hat{H}, \hat{a}^\dagger] = +i\omega_0\hat{a}^\dagger - BlQ\sqrt{\frac{\omega_0}{2\hbar M}} - i\frac{BI_{\mathrm{DC}}l}{\sqrt{2M\hbar\omega_0}} - \Gamma_0\hat{a}^\dagger + \hat{F}^\dagger. \tag{369}$$

where we have used $[\hat{a}, \hat{a}^\dagger] = 1$ and defined $\hat{F} = -i\sum_\omega \lambda_\omega \hat{b}_\omega(0)$. The terms $\hat{F}$ and $\hat{F}^\dagger$, which depend only on the initial configuration of the heat bath, describe the effect of thermal noise and can thus be neglected if we consider the low temperature limit $k_\mathrm{B}T \ll \Omega_0$. For the realistic parameters discussed later, this corresponds to very low but achievable temperatures of the order of 10mK. The evolution of $\hat{n} = \hat{a}^\dagger\hat{a}$ is then found from

$$\frac{\mathrm{d}\hat{n}}{\mathrm{d}t} = \frac{i}{\hbar}[\hat{H}, \hat{a}^\dagger\hat{a}] = \frac{i}{\hbar}\left\{\hat{a}^\dagger[\hat{H}, \hat{a}] + [H, \hat{a}^\dagger]\hat{a}\right\} = \hat{a}^\dagger\frac{\mathrm{d}\hat{a}}{\mathrm{d}t} + \frac{\mathrm{d}\hat{a}^\dagger}{\mathrm{d}t}\hat{a}, \tag{370}$$

yielding

$$\frac{\mathrm{d}\hat{n}}{\mathrm{d}t} = -\frac{Bl\omega_0}{\hbar}\hat{x}\hat{Q} + \frac{BI_\mathrm{DC}l}{\hbar M\omega_0}\hat{p} - 2\Gamma_0\hat{n}. \tag{371}$$

Here the first term on the right hand side describes the excitation of mechanical vibrations by the electromechanical coupling, the second term arises from the constant force $BI_\mathrm{DC}l$ and the final term gives the damping due to the coupling with the heat bath. This operator equation can be easily transformed into a classical equation for the expectation value $n(t)$, producing

$$\frac{\mathrm{d}n}{\mathrm{d}t} = -\frac{Bl\omega_0}{\hbar}\mathcal{C}_1 + \frac{BI_\mathrm{DC}l}{\hbar M\omega_0}p - 2\Gamma_0 n, \tag{372}$$

where $\mathcal{C}_1$ is the state average of $\hat{x}\hat{Q}$. Applying Heisenberg's equation to $\mathcal{C}_1$ and any new quantity that appears in the ensuing equations, one finds

$$\frac{\mathrm{d}\mathcal{C}_1}{\mathrm{d}t} = x\frac{\mathrm{d}Q}{\mathrm{d}t} + \mathcal{C}_2/M - Bl\mathcal{C}_3/M - \Gamma_0\mathcal{C}_1, \tag{373}$$

$$\frac{\mathrm{d}\mathcal{C}_2}{\mathrm{d}t} = p\frac{\mathrm{d}Q}{\mathrm{d}t} - M\omega_0^2\mathcal{C}_1 + BI_\mathrm{DC}lQ - \Gamma_0\mathcal{C}_2, \tag{374}$$

$$\frac{\mathrm{d}\mathcal{C}_3}{\mathrm{d}t} = 2Q\frac{\mathrm{d}Q}{\mathrm{d}t}, \tag{375}$$

where $\mathcal{C}_2$ and $\mathcal{C}_3$ are the state averages of $\hat{p}\hat{Q}$ and $\hat{Q}^2$, respectively. If we again use Eq. (359) to express Q in terms of the quasicharge q, Eqs. (372) - (375) can be solved for $n(t)$, with x, p and q obtained from (366) and (367).

6.2.3 Magnetic Field Dependence of Band Energy

To actually solve the above equations, we must specify the energy dispersion $E(q)$. This is the dispersion of the lowest band of the bare electronic Hamiltonian when the effective scalar and gauge fields are zero, $I_q = I_\mathrm{DC} = p = 0$ i.e. $\hat{H}_0 = \hat{Q}^2/2\tilde{C} - E_\mathrm{J}\cos\hat{\varphi}$. This is identical to the uncoupled case Eq. (334) except that the magnetic field renormalizes the effective capacitance $\widetilde{C} = C/(1+\mu^2)$. If we remain in the

tight-binding limit $E_{\mathrm{J}} \gg E_{\mathrm{C}}(1+\mu^2)$ we can then write down $E(q)$ by analogy with Eqs. (344) and (345) as follows

$$E(q) = \frac{\Omega}{2}\left(1 - \cos(\pi q/e)\right), \tag{376}$$

where Ω is the band width given by

$$\frac{\Omega}{E_J} = 16\sqrt{\frac{2}{\pi}}\exp\left(-\sqrt{\frac{8E_J}{E_C(1+\mu^2)}}\right). \tag{377}$$

Thus the magnetic field acts to slightly increase the band width. For convenience we will define the ratio of Ω to the zero magnetic field band width Ω_0 as

$$D(\mu) = \frac{\Omega}{\Omega_0} = d^{[(1+\mu^2)^{(-1/2)}-1]}, \tag{378}$$

where

$$d = \exp\left(-\sqrt{\frac{8E_J}{E_C}}\right). \tag{379}$$

This modification is usually very small, since $\mu^2 \ll 1$ for realistic magnetic field strengths.

6.2.4 Dimensionless Equations

Before numerically solving our equations of motion (366) and (367), we will write them in dimensionless form. Just as in the uncoupled case we define $i_{\mathrm{DC}} = I_{\mathrm{DC}}/I_{\mathrm{t}}$, $\bar{q} = q/q_0$ and measure time in units of $\tau_t = \omega_t t$. Here $I_{\mathrm{t}} = \pi\Omega_0/2eR$ is the threshold current at zero magnetic field, $q_0 = e/\pi$ and $\omega_t = \pi I_{\mathrm{t}}/e$. We also define the quality factor[16] $Q_\Gamma = \omega_0/\Gamma_0$, dimensionless resonance frequency $\omega = \omega_0/\omega_{\mathrm{t}}$ and displacement $a = x/x_t$ where $x_t = B_0 I_{\mathrm{t}} l/M\omega_t^2$. The equations of motion then take the following form

$$\dot{\bar{q}} = i_{\mathrm{DC}} - D(\mu)\sin(\bar{q}) + \frac{\mu}{1+\mu^2}\left(\omega^2 a + \frac{2\omega}{Q_\Gamma}\dot{a} - i_{\mathrm{DC}}\mu\right), \tag{380}$$

$$(1+\mu^2)\ddot{a} + \frac{2\omega}{Q_\Gamma}\dot{a} + \omega^2 a = \mu(i_{\mathrm{DC}} - \Lambda D(\mu)\cos(\bar{q})\dot{\bar{q}}). \tag{381}$$

Here $\Lambda = \omega_{\mathrm{t}} RC$ is a new parameter that is reminiscent of the Stewart-McCumber parameter $\beta_{\mathrm{c}} = \omega_{\mathrm{c}} RC$ in the classical case. In fact Λ may again be regarded as the ratio $\Lambda = |Z_R|/|Z_C|$, where $Z_R = R$ and $Z_C = -i/\omega_{\mathrm{t}} C$ are the impedances of the

[16] Not to be confused with the charge Q.

resistance and capacitive channels at the frequency ω_{t}, which is the characteristic frequency scale of Bloch oscillations. It is clear from Eq. (381) that in order to excite oscillations Λ should not be too small. This is just the condition that the bias current is mostly shunted by the displacement current so that the electronic current is predominantly AC. This was one of the reasons we needed to use underdamped junctions $\beta_{\mathrm{c}} \gg 1$ in the classical treatment in chapter 4, and the same principle applies here. The voltage may be expressed dimensionlessly as

$$\frac{V}{I_{\mathrm{t}}R} = D(\mu)\sin\bar{q} + \frac{\mu}{\Lambda}\dot{a}, \tag{382}$$

where, as usual, the second term on the right hand side has zero time average so it does not contribute to the DC voltage.

The vibron evolution equations (372) - (375) may also be put in a dimensionless form as follows

$$\dot{n} = \frac{2\Sigma\mu}{\pi^2\omega}\left(\mu i_{\mathrm{DC}}\left(\frac{p}{p_0}\right) - \omega^2 c_1\right) - \frac{2\omega}{Q_\Gamma}n, \tag{383}$$

$$\dot{c_1} = a\left(\frac{\dot{Q}}{q_0}\right) + c_2 - \mu c_3 - \frac{\omega}{Q_\Gamma}c_1, \tag{384}$$

$$\dot{c_2} = \left(\frac{p}{p_0}\right)\left(\frac{\dot{Q}}{q_0}\right) + \mu i_{\mathrm{DC}}\left(\frac{Q}{q_0}\right) - \omega^2 c_1 - \frac{\omega}{Q_\Gamma}c_2, \tag{385}$$

$$\dot{c_3} = 2\left(\frac{Q}{q_0}\right)\left(\frac{\dot{Q}}{q_0}\right), \tag{386}$$

where $p_0 = Mx_0\omega_{\mathrm{t}}$ is a characteristic momentum scale, $\Sigma = E_{\mathrm{c}}/\hbar\omega_{\mathrm{t}}$ while $c_1 = \mathcal{C}_1/x_0q_0$, $c_2 = \mathcal{C}_2/p_0q_0$ and $c_3 = \mathcal{C}_3/q_0^2$ are dimensionless forms of the state averages of $\hat{x}\hat{Q}$, $\hat{p}\hat{Q}$ and $\hat{Q}^2$ respectively. Upon insertion of

$$\frac{p}{p_0} = (1+\mu^2)\dot{a} + \Lambda\mu D(\mu)\sin(\bar{q}), \tag{387}$$

and

$$\frac{Q}{q_0} = \Lambda D(\mu)\sin(\bar{q}) + \mu\dot{a}, \tag{388}$$

these four equations may be solved for $n(t)$ once $\bar{q}$ and a are determined from Eqs. (380) and (381). The fixed parameters of our system of equations are ω, Q_Γ, d, Λ and Σ while i_{DC} and μ may be experimentally tuned as usual. We now finally move on to numerically solve these equations to establish whether mechanical oscillations are excited and what effects they have on the electronic system.

6.2.5 Mechanically Induced Voltage Peaks

We numerically solve Eqs. (380), (381) and the vibron evolution equations (383)-(386) using the following parameters appropriate for carbon nanotube devices $I_c = 1\text{nA}$, $R = 10\text{k}\Omega$, $C = 5 \times 10^{-14}\text{F}$, $l = 1\mu\text{m}$, $M = 10^{-21}\text{kg}$, $\omega_0/2\pi = 1\text{GHz}$, $Q_\Gamma = \omega_0/\Gamma_0 = 10^4$ [27, 63–67, 73]. All other parameters may be derived from these fundamental ones, and in particular the important dimensionless parameters $\omega = \omega_0/\omega_t = 1.92$, $\Lambda = \omega_t RC = 1.64$ and $\Sigma = E_c/\hbar\omega_t = 0.74$. The ratio of the two energy scales E_J and E_C may then be derived as $E_J/E_C = 1.29$ so that our tight-binding approximation is fairly reasonable. The final parameter d that characterizes the change in the energy band width is then calculated to be $d = \exp(-\sqrt{8E_J/E_C}) = 0.04$.

Fig. 58(a) shows the numerically calculated I-V characteristics for a number of different values of the coupling μ, where the characteristic current, voltage and magnetic field scales are $I_t = 0.167\text{nA}$, $V_t = I_t R = 1.67\mu\text{V}$ and $B_0 = 141\text{T}$. In the absence of electromechanical coupling, i.e. $\mu = 0$, the usual Ohmic behaviour for $I_{DC} < I_t$ is observed along with negative differential resistance for $I_{DC} > I_t$. Switching on the coupling causes the oscillator to vibrate, resulting in distinctive voltage peaks in the I-V curve. These peaks develop when the Bloch oscillation frequency ω_B matches the resonance frequency ω_0, due to the gauge field $\tilde{C}Bl\dot{p}/M$ acting as an effective AC current. The inset of Fig. 58 displays a plot of ω_B against current that explicitly shows this frequency locking, similar to the familiar Shapiro plateaus. The voltage peaks reach a maximum size of $\sim 0.2\mu\text{V}$, but if the coupling is increased further the peaks begin to reduce in size. At first glance, it appears that this may be due to the coupling entering the electronic equation (380) as $\mu/(1+\mu^2)$, due to the renormalization of the capacitance, but this reduction begins to occur at low coupling $\mu \approx 0.3$ where the renormalization is still insignificant. The true explanation of this effect seems to be that when the oscillations become too strong, their back action on the electronic degrees of freedom brings the system off resonance.

The excitation of the oscillator may be studied by looking at the expectation value $n(t)$ of the vibron number. Solving Eqs. (383) - (386), we find that the oscillator eventually evolves into a state with $n(t)$ generally oscillatory but highly localized around an average $\langle n \rangle$. In Fig 58(b) we display $\langle n \rangle$ as a function of the bias current I_{DC}, focusing on the region $I_{DC} > I_t$ where mechanical oscillations are excited. Comparing this plot with panel (a) shows that the oscillator excitation coincides with the voltage peaks in the I-V characteristic. As such, the mechanical vibrations have a direct influence on the I-V curve and may be turned on or off by

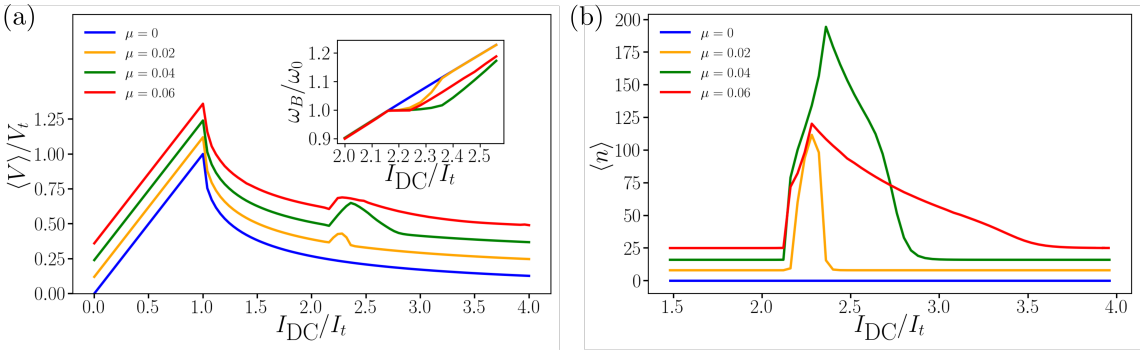

Figure 58: (a) I-V characteristic obtained from Eqs. (380) and (381) for various values of coupling strengths $\mu = B/B_0$ with the parameters quoted in the main text, for which $I_t = 0.167$nA, $V_t = I_t R = 1.67\mu$V, $\omega_0/2\pi = 1$GHz, $B_0 = 141$T. A distinct voltage peak of size $\sim 0.2\mu$V is observable when the Bloch oscillation frequency ω_B locks onto the mechanical resonance frequency ω_0. The inset displays a plot of ω_B against current that explicitly shows this frequency locking. (b) Time average of the vibron number $\langle n \rangle$ as a function of I_{DC}, obtained from Eqs. (383) - (386) for various values of coupling $\mu = B/B_0$ using the same parameters as in Fig. 58. Plots with $\mu \neq 0$ are displaced upward along the vertical axis slightly for clarity.

simply tuning ω_B toward or away from ω_0. Note that the oscillator is not excited gradually, increasing I_{DC} does not increase $\langle n \rangle$ until frequency locking happens, the oscillator is then suddenly activated, increasing n by multiple orders of magnitude within a small range of current, from zero to the peak value ~ 200 for the parameters used here. The zero-point motion of the oscillator is $\sqrt{\hbar/2M\omega_0} \approx 2.9$pm so that we can estimate the maximum amplitude of the oscillations by $x_{zp}\sqrt{2n+1} \approx 58$pm.

To observe in more detail how these voltage and vibron number peaks are modified by the coupling, Fig. 59 displays colour plots of $\langle V \rangle$ [panel (a)] and $\langle n \rangle$ [panel (b)] as functions of both the current and the magnetic field. Only the region $I_{DC} > I_t$ is shown for clarity. A direct correspondence between $\langle V \rangle$ and $\langle n \rangle$ is observed. Optimal values of μ and I_{DC} are observed where $\langle n \rangle$ and $\langle V \rangle$ are peaked, see the red spot in the plots. For the parameters used here the optimal coupling value occurs around $\mu \approx 0.03$, corresponding to a magnetic field of $B \approx 4$T. If μ is increased further, vibrations begin to be suppressed as discussed above.

Thus we have seen that Bloch oscillations in Josephson junctions can be used to amplify mechanical vibrations with only DC techniques, just as the classical Josephson oscillations were used in chapter 4. This could provide a novel way of observing Bloch oscillations without the need of a probing AC current as has been used in previous set ups. Our work may also give an insight into non-classical mechanical states, as the vibrations excited here are intimately coupled to the Bloch oscillations, a strictly quantum phenomenon.

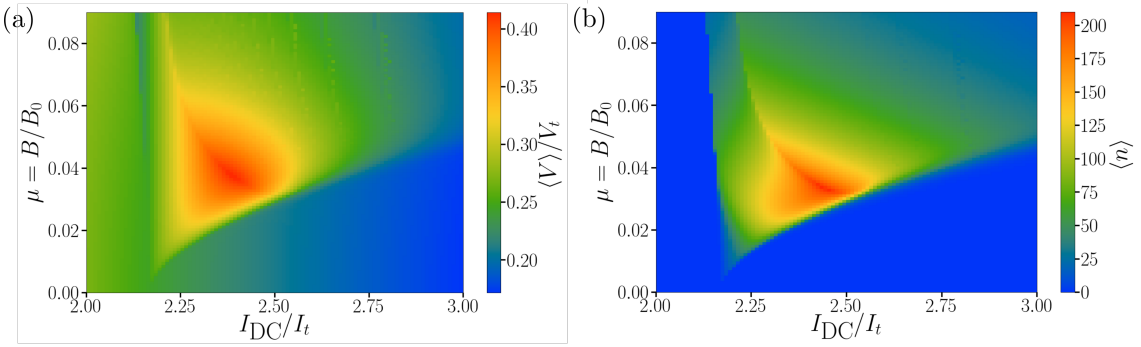

Figure 59: (a) DC voltage $\langle V\rangle$ and (b) average vibron number $\langle n\rangle$ as functions of I_{DC} and μ for the same parameters as in Figs. 58. Optimal values for I_{DC} and μ exist for which the mechanical oscillations are maximally excited, leading to the maximum size of the voltage peak. $\langle V\rangle$ and $\langle n\rangle$ peak at approximately 1μV and 200, respectively.

In order to experimentally realize this proposal, or at least to reach the optimal value of μ, fairly large magnetic fields must be used of the order of 1T. Superconducting contacts with fairly high critical fields of the order of 10T or more should then be used, for example ones based on niobium nitride [91]. The optimal magnetic field value may also be lowered by increasing the quality factor Q_Γ, analogously to the critical values μ_{c1} and μ_{c2} of chapter 4. Additionally, as the coupling strength $\tilde{C}Bl/M$ is proportional to the capacitance C, it is desirable to increase C to enhance the coupling. On the other hand, the peak value of $\langle V\rangle = (\pi\Omega/2e)\langle\sin(\pi q/e)\rangle$ is proportional to the band width Ω which, as Eq. (377) suggests, decreases with increased capacitance. For the best experimental outcome, C should therefore be tuned between these two extremes. Finally, low temperatures are required to ensure that the amplified mechanical vibrations exceed thermal excitations, and also so that voltage fluctuations do not destroy the voltage peak. This latter condition is much stricter, requiring the thermal energy to be lower than the band width, $k_{\mathrm{B}}T \ll \Omega$. For the parameters used here this corresponds to very low but achievable temperatures of the order of 10mK.

7 Conclusions and Perspectives

Throughout this thesis, we discussed the theory of electromechanically coupled Josephson junctions. It is clear that the Josephson effect, via the conversion of a DC bias into an AC supercurrent, allows the excitation of mechanical oscillations in a suspended weak link, removing the need for AC bias in NEMS devices. We analyzed in depth a very simple setup consisting of a weak link, or a SQUID, suspended between two superconducting contacts. A DC current bias and uniform magnetic field, combined with DC voltage measurements, are then all that is required to observe a variety of interesting mechanically induced effects including Shapiro steps, abrupt energy induced retrappings and fractal-like structures.

In state-of-the-art devices with resonance frequencies and quality factors $\omega_0 \approx$ 10GHz and $Q_\Gamma \approx 10^6$ [63, 64], mechanically induced effects are predicted to appear at voltages of the order 1μV and span over large current plateaus of the order of the critical current. There is no difficulty in achieving this level of resolution in present setups [27, 73]. The crossover to the strong coupling regime may be observed in these devices at magnetic fields of the order of 100mT.

One challenge for the experimental observation of the predictions presented here is the need for the Josephson junctions to be in the underdamped regime, $\beta_c = \omega_c RC \gg 1$ (or in the Bloch oscillation regime $\Lambda = \omega_t RC \gg 1$) i.e. devices with large inter-electrode capacitances. Fortunately, many graphene and CNT based junctions seem to naturally operate in this regime [71–73]. In the Bloch oscillation regime, a stricter constraint is placed on the capacitance, as increasing it too much reduces the width of the energy bands, and thus decreases the mechanically induced voltage signal. This difficulty is easily overcome, as the effective capacitance may be tuned by connecting the junction in parallel with an external capacitor [74].

A further challenge is the need to minimize the effects of temperature by decreasing the thermal energy $k_B T$ below the energy scale $\hbar I_{DC}/2e$ associated with the bias current I_{DC}. For the state-of-the-art devices with $\omega_0 \approx$ 10GHz discussed above, we predict that the observation of the proposed effects requires temperatures $T <$ 100mK, compatible with recent measurements [18, 20]. Once again in the Bloch oscillation regime a stricter constraint is placed on the temperature by the requirement that the thermal energy is lower than the energy band width Ω, so that to observe the mechanically induced effects in this regime, lower temperatures of the order of $T \sim$ 10mK are required.

It is hoped that the mechanically induced effects presented here will soon be observed experimentally in suspended Josephson junction resonators. They could subsequently find their use in a number of potential applications. The existence of a

Shapiro plateau, located at precisely the bare resonance frequency of the weak link, could be very useful for metrology as well as further research into NEMS without requiring complicated AC setups. The abrupt transitions that emerge in the strong coupling regime, and in particular their dependence on the magnetic flux in SQUIDs, could result in high precision sensors for current, voltage and magnetic fields.

Acknowledgements

I would like to express my deepest thanks to my supervisor Eros Mariani for his hard work, dedication and continuous support over the four years of my PhD. My second supervisor Saverio Russo provided invaluable stimulating discussions that began this research, for which I am very grateful. This thesis would also have not been possible without my main collaborators who helped with much of the research presented here, so I would like to give a special thanks to Hai-Yao Deng, Jamie Le Signe, Antonio Di Lorenzo and Andreas Isacsson.

Without my close friends I would not have made it to the end of my PhD and I would like to thank in particular Angus Laurenson, Natalie Whitehead and Callum Vincent. Finally, but most importantly, I thank my parents Robert and Elaine, and my brother Matthew, as well as all my extended family for their love and support throughout my life.

A Lagrangian: Uncoupled SQUID

The equations of motion (273) and (274) can be derived from the Euler-Lagrange equations

$$\frac{\mathrm{d}}{\mathrm{d}t}\frac{\partial \mathcal{L}}{\partial(\mathrm{d}q_i/\mathrm{d}t)} - \frac{\partial \mathcal{L}}{\partial q_i} = -\frac{\partial P}{\partial(\mathrm{d}q_i/\mathrm{d}t)}, \tag{389}$$

where $q_i = \{\varphi_1, \varphi_2\}$ are the generalised coordinates and the Lagrangian $\mathcal{L}$ and dissipation function P are given by

$$\mathcal{L} = \sum_n \left\{ \frac{1}{2} C_n V_n^2 + \frac{\hbar I_{cn}}{2e} \cos\varphi_n - \frac{1}{2} L_n I_n^2 \right\} + \int I_{\mathrm{DC}} V \, dt, \tag{390}$$

$$P = \sum_n \frac{V_n^2}{2R_n}, \tag{391}$$

where the summations are over the two arms $n = 1, 2$. These are just the sums of the corresponding functions for two separate junctions, except for the inductance term which couples the two together through the circulating current J. This can be seen by writing $\mathcal{L}$ and P explicitly in terms of φ_1 and φ_2 as

$$\begin{aligned} \mathcal{L} = &\sum_n \left\{ \frac{1}{2} C_n \left(\frac{\hbar}{2e} \frac{\mathrm{d}\varphi_n}{\mathrm{d}t} \right)^2 + \frac{\hbar I_{cn}}{2e} \cos\varphi_n + \frac{\hbar I_{\mathrm{DC}}}{2e} \frac{L_{\mathrm{red}}}{L_n} \varphi_n \right\} \\ &- \left(\frac{\hbar}{2e} \right)^2 \frac{1}{2L} \left(\varphi_2 - \varphi_1 - \frac{2\pi\Phi}{\Phi_0} \right)^2, \end{aligned} \tag{392}$$

$$P = \sum_n \frac{1}{2R_n} \left(\frac{\hbar}{2e} \frac{\mathrm{d}\varphi_n}{\mathrm{d}t} \right)^2, \tag{393}$$

where $L_{\mathrm{red}} = L_1 L_2 / L$ is the reduced inductance. Here we can see that the inclusion of the energy stored in the inductance leads to a term that couples φ_1 and φ_2. The following equations of motion can then be derived

$$I_{\mathrm{DC}} \frac{L_{\mathrm{red}}}{L_n} \pm \frac{\hbar}{2eL} \left(\varphi_2 - \varphi_1 - \frac{2\pi\Phi}{\Phi_0} \right) = I_{cn} \sin\varphi_n + \frac{\hbar}{2eR_n} \frac{\mathrm{d}\varphi_n}{\mathrm{d}t} + \frac{\hbar C_n}{2e} \frac{\mathrm{d}^2\varphi_n}{\mathrm{d}t^2}, \tag{394}$$

where the plus sign is taken for $n = 1$ and the minus sign for $n = 2$. Using the flux relation (283) to write J in terms of φ_1 and φ_2 we see that the LHS of (394) is just $I_{\mathrm{DC}}/2 \pm J$ so that these correctly produce Eqs. (273) and (274).

The Hamiltonian may also be derived from the usual relation

$$H = \sum_n \frac{\mathrm{d}q_n}{\mathrm{d}t} \frac{\partial \mathcal{L}}{\partial(\mathrm{d}q_n/\mathrm{d}t)} - \mathcal{L}, \tag{395}$$

$$= \sum_n C_n \left(\frac{\hbar}{2e}\frac{\mathrm{d}\varphi_n}{\mathrm{d}t}\right)^2 - \mathcal{L}. \tag{396}$$

So that, compared to the Lagrangian, the kinetic energy terms keep the same sign while the potential energy terms reverse sign as usual, producing

$$H = \sum_n \left\{ \frac{1}{2} C_n \left(\frac{\hbar}{2e}\frac{\mathrm{d}\varphi_n}{\mathrm{d}t}\right)^2 - \frac{\hbar I_{cn}}{2e}\cos\varphi_n - \frac{\hbar I_{\mathrm{DC}}}{2e}\frac{L_{\mathrm{red}}}{L_n}\varphi_n \right\} + \left(\frac{\hbar}{2e}\right)^2 \frac{1}{2L}\left(\varphi_2 - \varphi_1 - \frac{2\pi\Phi}{\Phi_0}\right)^2. \tag{397}$$

For completeness the total energy is given by $E = H + \int I_{\mathrm{DC}} V \mathrm{d}t$ as follows

$$E = \sum_n \left\{ \frac{1}{2} C_n \left(\frac{\hbar}{2e}\frac{\mathrm{d}\varphi_n}{\mathrm{d}t}\right)^2 - \frac{\hbar I_{cn}}{2e}\cos\varphi_n \right\} + \left(\frac{\hbar}{2e}\right)^2 \frac{1}{2L}\left(\varphi_2 - \varphi_1 - \frac{2\pi\Phi}{\Phi_0}\right)^2. \tag{398}$$

If the junctions are symmetric, we can express each of these functions in terms of dimensionless quantities, $\bar{\mathcal{L}} = \mathcal{L}/E_{\mathrm{J}}$, $\bar{P} = P/E_{\mathrm{J}}\omega_{\mathrm{c}}$, $\bar{H} = H/E_{\mathrm{J}}$ and $\bar{E} = E/E_{\mathrm{J}}$, where $E_{\mathrm{J}} = \hbar I_{\mathrm{c}}/2e$, as follows

$$\bar{\mathcal{L}} = \sum_n \left\{ \frac{\beta_{\mathrm{c}}}{2}\dot{\varphi}_n^2 + \cos\varphi_n + \frac{i_{\mathrm{DC}}}{2}\varphi_n \right\} - \frac{1}{2\pi\beta_L}(\varphi_2 - \varphi_1 - 2\pi\phi_{\mathrm{a}})^2, \tag{399}$$

$$\bar{P} = \frac{1}{2}\sum_n \dot{\varphi}_n^2 \tag{400}$$

$$\bar{H} = \sum_n \left\{ \frac{\beta_{\mathrm{c}}}{2}\dot{\varphi}_n^2 - \cos\varphi_n - \frac{i_{\mathrm{DC}}}{2}\varphi_n \right\} + \frac{1}{2\pi\beta_L}(\varphi_2 - \varphi_1 - 2\pi\phi_{\mathrm{a}})^2, \tag{401}$$

$$\bar{E} = \sum_n \left\{ \frac{\beta_{\mathrm{c}}}{2}\dot{\varphi}_n^2 - \cos\varphi_n \right\} + \frac{1}{2\pi\beta_L}(\varphi_2 - \varphi_1 - 2\pi\phi_{\mathrm{a}})^2. \tag{402}$$

B Lagrangian: Coupled SQUID

The Lagrangian and dissipation functions of the mechanically coupled SQUID are given by

$$\mathcal{L} = \sum_n \left\{ \frac{1}{2} C_n V_n^2 + \frac{\hbar I_{cn}}{2e} \cos\varphi_n - \frac{1}{2} L_n I_n^2 + \frac{1}{2} M_n \left(\left(\frac{\mathrm{d}x_n}{\mathrm{d}t} \right)^2 - \omega_n^2 x_n^2 \right) \right\} + \int I_{\mathrm{DC}} V \mathrm{d}t, \tag{403}$$

$$P = \sum_n \left\{ \frac{(V_n - B_n l_n \mathrm{d}x_n/\mathrm{d}t)^2}{2R_n} + M_n \Gamma_n \left(\frac{\mathrm{d}x_n}{\mathrm{d}t} \right)^2 \right\}. \tag{404}$$

which in terms of our generalized coordinates $q_i = \{\varphi_1, a_1, \varphi_2, a_2\}$ become

$$\mathcal{L} = \sum_n \left\{ \frac{1}{2} C_n \left(\frac{\hbar}{2e} \frac{\mathrm{d}\varphi_n}{\mathrm{d}t} + B_n l_n \frac{\mathrm{d}x_n}{\mathrm{d}t} \right)^2 + \frac{\hbar I_{cn}}{2e} \cos\varphi_n + \frac{\hbar I_{\mathrm{DC}}}{2e} \frac{L_{\mathrm{red}}}{L_n} \left(\varphi_n + \frac{2e}{\hbar} B_n l_n x_n \right) \right.$$
$$\left. + \frac{1}{2} M_n \left(\left(\frac{\mathrm{d}x_n}{\mathrm{d}t} \right)^2 - \omega_n^2 x_n^2 \right) \right\} - \frac{1}{2L} \left[\frac{\hbar}{2e} (\varphi_2 - \varphi_1) - \Phi + B_2 l_2 x_2 - B_1 l_1 x_1 \right]^2, \tag{405}$$

$$P = \sum_n \left\{ \frac{1}{2R_n} \left(\frac{\hbar}{2e} \frac{\mathrm{d}\varphi_n}{\mathrm{d}t} \right)^2 + M_n \Gamma_n \left(\frac{\mathrm{d}x_n}{\mathrm{d}t} \right)^2 \right\}. \tag{406}$$

We note that this Lagrangian (405) is obtained from the uncoupled one (392) by first adding the purely mechanical terms, and then replacing φ_n with $(\varphi_n + (2e/\hbar) B_n l_n x_n)$ everywhere except the Josephson energy (cosine) term. This reflects the fact that the voltage is related to $\dot{\varphi_n}$ in this new way, while the supercurrents remain as $I_{cn} \sin\varphi_n$. The Hamiltonian and energy are then derived in the usual way, yielding

$$H = \sum_n \left\{ \frac{1}{2} C_n \left(\frac{\hbar}{2e} \frac{\mathrm{d}\varphi_n}{\mathrm{d}t} + B_n l_n \frac{\mathrm{d}x_n}{\mathrm{d}t} \right)^2 - \frac{\hbar I_{cn}}{2e} \cos\varphi_n - \frac{\hbar I_{\mathrm{DC}}}{2e} \frac{L_{\mathrm{red}}}{L_n} \left(\varphi_n + \frac{2e}{\hbar} B_n l_n x_n \right) \right.$$
$$\left. + \frac{1}{2} M_n \left(\left(\frac{\mathrm{d}x_n}{\mathrm{d}t} \right)^2 + \omega_n^2 x_n^2 \right) \right\} + \frac{1}{2L} \left[\frac{\hbar}{2e} (\varphi_2 - \varphi_1) - \Phi + B_2 l_2 x_2 - B_1 l_1 x_1 \right]^2, \tag{407}$$

$$E = \sum_n \left\{ \frac{1}{2} C_n \left(\frac{\hbar}{2e} \frac{\mathrm{d}\varphi_n}{\mathrm{d}t} + B_n l_n \frac{\mathrm{d}x_n}{\mathrm{d}t} \right)^2 - \frac{\hbar I_{cn}}{2e} \cos\varphi_n \right.$$
$$\left. + \frac{1}{2} M_n \left(\left(\frac{\mathrm{d}x_n}{\mathrm{d}t} \right)^2 + \omega_n^2 x_n^2 \right) \right\} + \frac{1}{2L} \left[\frac{\hbar}{2e} (\varphi_2 - \varphi_1) - \Phi + B_2 l_2 x_2 - B_1 l_1 x_1 \right]^2. \tag{408}$$

Finally, the dimensionless forms in the symmetric junction case are

$$\bar{\mathcal{L}} = \sum_n \left\{ \frac{\beta_c}{2}(\dot{\varphi}_n + \mu_n \dot{a}_n/\beta_c)^2 + \cos\varphi_n + \frac{i_{DC}}{2}(\varphi_n + \mu_n a_n/\beta_c) + \frac{1}{2\beta_c}(\dot{a}_n^2 - \bar{\omega}_n^2 a_n^2) \right\} - \frac{1}{2\pi\beta_L}\left[\varphi_2 - \varphi_1 - 2\pi\phi_a + (\mu_2 a_2 - \mu_1 a_1)/\beta_c\right]^2, \quad (409)$$

$$\bar{P} = \sum_n \left\{ \frac{1}{2}\dot{\varphi_n}^2 + \frac{\bar{\omega}_n}{Q_\Gamma \beta_c}\dot{a_n}^2 \right\}, \quad (410)$$

$$\bar{H} = \sum_n \left\{ \frac{\beta_c}{2}(\dot{\varphi}_n + \mu_n \dot{a}_n/\beta_c)^2 - \cos\varphi_n - \frac{i_{DC}}{2}(\varphi_n + \mu_n a_n/\beta_c) + \frac{1}{2\beta_c}(\dot{a}_n^2 + \bar{\omega}_n^2 a_n^2) \right\} + \frac{1}{2\pi\beta_L}\left[\varphi_2 - \varphi_1 - 2\pi\phi_a + (\mu_2 a_2 - \mu_1 a_1)/\beta_c\right]^2, \quad (411)$$

$$\bar{E} = \sum_n \left\{ \frac{\beta_c}{2}(\dot{\varphi}_n + \mu_n \dot{a}_n/\beta_c)^2 - \cos\varphi_n + \frac{1}{2\beta_c}(\dot{a}_n^2 + \bar{\omega}_n^2 a_n^2) \right\} + \frac{1}{2\pi\beta_L}\left[\varphi_2 - \varphi_1 - 2\pi\phi_a + (\mu_2 a_2 - \mu_1 a_1)/\beta_c\right]^2. \quad (412)$$

References

[1] J. R. Schrieffer, *Theory of superconductivity* (Benjamin, New York, 1964).

[2] P. G. De Gennes, Rev. Mod. Phys. **36**, 225 (1964).

[3] B. D. Josephson, Phys. Lett. **1**, 251 (1962).

[4] S. Shapiro, Phys. Rev. Lett. **11**, 80 (1963).

[5] S. Shapiro, A. R. Janus and S. Holly, Rev. Mod. Phys. **36**, 223 (1964).

[6] *Resolutions of the CGPM: 18th meeting*, (1987).

[7] X. Zhou and A. Mizel, Phys. Rev. Lett. **97**, 267201 (2006).

[8] E. Buks and M. P. Blencowe, Phys. Rev. B **74**, 174504 (2006).

[9] M. P. Blencowe and E. Buks, Phys. Rev. B **76**, 014511 (2007).

[10] E. Buks, E. Segev, S. Zaitsev, B. Abdo, and M. P. Blencowe, Europhys. Lett. **81**, 10001 (2008).

[11] J.-X. Zhu, Z. Nussinov, and A. V. Balatsky, Phys. Rev. B **73**, 064513 (2006).

[12] G. Sonne, R. I. Shekhter, L. Y. Gorelik, S. I. Kulinich, and M. Jonson, Phys. Rev. B **78**, 144501 (2008).

[13] G. Sonne, M. E. Peña-Aza, L. Y. Gorelik, R. I. Shekhter, and M. Jonson, Phys. Rev. Lett. **104**, 226802 (2010).

[14] G. Sonne and L. Y. Gorelik, Phys. Rev. Lett. **106**, 167205 (2011).

[15] C. Padurariu, C. J. H. Keijzers, and Y. V. Nazarov, Phys. Rev. B **86**, 155448 (2012).

[16] A. Marchenkov, Z. Dai, B. Donehoo, R. N. Barnett, and U. Landman, Nat. Nanotechnol. **2**, 481 (2007).

[17] H. Keijzers, *Josephson Effects in Carbon Nanotube Mechanical Resonators and Graphene*, Ph.D. thesis, Delft University of Technology (2012).

[18] B. H. Schneider, S. Etaki, H. S. J. van der Zant, and G. A. Steele, Sci. Rep. **2**, 599 (2012).

[19] S. Etaki, F. Konschelle, Y. M. Blanter, H. Yamaguchi, and H. S. J. van der Zant, Nat. Commun. **4**, 1803 (2013).

[20] A. Kretinin, A. Das, and H. Shtrikman, arXiv:1303.1410v2.

[21] J. Koch and F. von Oppen, Phys. Rev. Lett. **94**, 206804 (2005).

[22] J. Koch, F. von Oppen, and A. V. Andreev, Phys. Rev. B **74**, 205438 (2006).

[23] S. Sapmaz, P. Jarillo-Herrero, Y. M. Blanter, C. Dekker, and H. S. J. van der Zant, Phys. Rev. Lett. **96**, 026801 (2006).

[24] R. Leturcq, C. Stampfer, K. Inderbitzin, L. Durrer, C. Hierold, E. Mariani, M. G. Schultz, F. von Oppen, and K. Ensslin, Nature Phys. **5**, 327 (2009).

[25] K. K. Likharev, Rev. Mod. Phys. **51**, 101 (1979).

[26] R. C. Jaklevic, J. Lambe, A. H. Silver, and J. E. Mercereau, Phys. Rev. Lett. **12**, 159 (1964).

[27] J.-P. Cleuziou, W. Wernsdorfer, V. Bouchiat, T. Ondarçuhu, and M. Monthioux, Nat. Nanotechnol. **1**, 53 (2006).

[28] T. McDermott, H.-Y. Deng, A. Isaccson, E. Mariani, Phys. Rev. B **97**, 014526 (2018).

[29] H. Kamerlingh-Onnes, Comm. Phys. Lab. Univ. Leiden, Nos. 119, 120, 122 (1911).

[30] W. Meissner and R. Ochsenfeld, Naturwiss. **21**, 787 (1933).

[31] F. London and H. London, Proc. Royal Soc. Lond. **A149**, 866 (1935).

[32] V. L. Ginzburg and L. D. Landau, Sov. Phys. JETP. **20**, 1064 (1950).

[33] C. A. Reynolds, B. Serin, W. H. Wright and L. B. Nesbitt, Phys. Rev. **78**, 487 (1950).

[34] E. Maxwell, Phys. Rev. **78**, 477 (1950).

[35] H. Fröhlich, Phys. Rev. **79**, 845 (1950).

[36] W. S. Corak, B. B. Goodman, C. B. Satterthwaite and A. Wexler, Phys. Rev. **96**, 1442 (1954).

[37] W. S. Corak, B. B. Goodman, C. B. Satterthwaite and A. Wexler, Phys. Rev. **102**, 656 (1956).

[38] J. G. Daunt and K. Mendelssohn, Proc. Royal Soc. Lond. **A185**, 225 (1946).

[39] R. E. Glover, III and M. Tinkham, Phys. Rev. **108**, 243 (1957).

[40] I. Giaever, Phys. Rev. Lett. **5**, 147 (1960).

[41] L. N. Cooper, Phys. Rev. **104**, 1189 (1956).

[42] J. Bardeen, L. N. Cooper and J. R. Schrieffer, Phys. Rev. **106**, 162 (1957).

[43] J. Bardeen, Rev. Mod. Phys. **23**, 261 (1951).

[44] P. W. Anderson, J. Phys.: Conf. Ser. **449** 012001 (2013).

[45] M. R. Schafroth, J. M. Blatt and S. T. Butler, Helv. Phys. Acta **30**, 93 (1957).

[46] N. N. Bogoliubov, Nuovo Cimento **7**, 794 (1958).

[47] J. G. Valatin, Nuovo Cimento **7**, 843 (1958).

[48] L. P. Gor'kov, J. Exp. Theor. Phys. **9**, 1364 (1959).

[49] P. W. Anderson and J. M. Rowell, Phys. Rev. Lett. **10**, 230 (1963).

[50] P. W. Anderson and A. H. Dayem, Phys. Rev. Lett. **13**, 195 (1964).

[51] J. Clarke, Proc. Roy. Soc. A **308**, 447 (1969).

[52] V. Ambegaokar and A. Baratoff, Phys. Rev. Lett. **10**, 486 (1963).

[53] I. O. Kulik and A. N. Omel'yanchuk, Sov. J. Low Temp. Phys. **3**, 459 (1978).

[54] K. D. Usadel, Phys. Rev. Lett. **25**, 507 (1970).

[55] G. Eilenberger, Z. Phys. **214**, 195 (1968).

[56] R. P. Feynman, R. B. Leighton and M. Sands, *The Feynman Lectures on Physics Vol. III* (Addison-Wesley, Reading Mas., 1964).

[57] R. P. Feynman and A. R. Hibbs, *Quantum Mechanics and Path Integrals* (Dover, New York, 1965).

[58] W. C. Stewart, Appl. Phys. Lett. **12**, 277 (1968).

[59] D. E. McCumber, J. Appl. Phys. **39**, 3113 (1968).

[60] M. Tinkham, *Introduction to Superconductivity* (Dover, New York, 2004).

[61] T. Fulton and L. N. Dunkleberger, Phys. Rev. B **9**, 4760 (1974).

[62] P. Russer, J. Appl. Phys. **43**, 2008 (1972).

[63] H. B. Peng, C. W. Chang, S. Aloni, T. D. Yuzvinsky, and A. Zettl, Phys. Rev. Lett. **97**, 087203 (2006).

[64] D. Garcia-Sanchez, A. San Paulo, M. J. Esplandiu, F. Perez-Murano, L. Forró, A. Aguasca, and A. Bachtold, Phys. Rev. Lett. **99**, 085501 (2007).

[65] A. K. Hüttel, G. A. Steele, B. Witkamp, M. Poot, L. P. Kouwenhoven, and H. S. J. van der Zant, Nano Lett. **9**, 2547 (2009).

[66] E. A. Laird, F. Pei, W. Tang, G. A. Steele, and L. P. Kouwenhoven, Nano Lett. **12**, 193 (2012).

[67] J. Moser, A. Eichler, J. Güttinger, M. I. Dykman, and A. Bachtold, Nat. Nanotechnol. **9**, 1007 (2014).

[68] J. S. Bunch, A. M. van der Zande, S. S. Verbridge, I. W. Frank, D. M. Tanenbaum, J. M. Parpia, H. G. Craighead, and P. L. McEuen, Science **315**, 490 (2007).

[69] C. Chen, S. Rosenblatt, K. I. Bolotin, W. Kalb, P. Kim, I. Kymissis, H. L. Stormer, T. F. Heinz, and J. Hone, Nat. Nanotechnol. **4**, 861 (2009).

[70] N. Morell, A. Reserbat-Plantey, I. Tsioutsios, K. G. Schädler, F. Dubin, F. H. L. Koppens, and A. Bachtold, Nano Lett. **16**, 5102 (2016).

[71] H. B. Heersche, P. Jarillo-Herrero, J. B. Oostinga, L. M. K. Vandersypen, and A. F. Morpurgo, Nature **446**, 56 (2007).

[72] N. Mizuno, B. Nielsen, and X. Du, Nat. Commun. **4**, 2716 (2013).

[73] P. Jarillo-Herrero, J. A. van Dam, and L. P. Kouwenhoven, Nature **439**, 953 (2006).

[74] K. K. Likharev, *Dynamics of Josephson Junctions and Circuits* (Gordon and Breach Science Publishers, New York, 1986).

[75] L. D. Landau and E. M. Lifshitz, *Mechanics Vol. 1* (Pergamon Press, Oxford, 1969).

[76] M. Aziz, D. C. Hudson, and S. Russo, Appl. Phys. Lett. **104**, 233102 (2014).

[77] F. Wellstood, C. Heiden, and J. Clarke, Rev. Sci. Instrum. **55**, 952 (1984).

[78] J. E. Zimmerman and D. B. Sullivan, Appl. Phys. Lett. **31**, 360 (1977).

[79] Y. Song and J. P. Hurrell, IEEE Trans. Mag. **15**, 428 (1979).

[80] C. Zener, Proc. R. Soc. Ser. A **145**, 523 (1934).

[81] K. Leo, P. H. Bolivar, F. Bruggemann, R. Schwedler and K. Kohler, Solid State Communications **84**, 943 (1992).

[82] T. Dekorsy, R. Ott, H. Kurz and K. Kohler, Phys. Rev. B **51**, 17275 (1995).

[83] C. Waschke, H. G. Roskos, R. Schwedler, K. Leo, H. Kurz and K. Kohler, Phys. Rev. Lett. **70**, 3319 (1993).

[84] K. Unterrainer, B. J. Keay, M. C. Wanke and S. J. Allen, Phys. Rev. Lett. **76**, 2973 (1996).

[85] K. K. Likharev and A. B. Zorin, in *Proceedings of the 17th conference on low temperature physics*, edited by U. Eckern, A. Schmid, W. Weber and H. Wühl (North Holland, Amsterdam, 1984), pp. 1153-1154.

[86] D. V. Averin, A. B. Zorin and K. K. Likharev, Sov. Phys. JETP **61**, 407 (1985).

[87] K. K. Likharev and A. B. Zorin, J. Low. Temp. Phys. **59**, 347 (1985).

[88] D. V. Averin and K. K. Likharev, J. Low. Temp. Phys. **62**, 345 (1986).

[89] L. S. Kuzmin and D. B. Haviland, Phys. Rev. Lett. **67**, 2890 (1991).

[90] H. Vora, R. L. Kautz, S. W. Nam and J. Aumentado, Phys. Rev. B **96**, 054505 (2017).

[91] T. H. Courtney, J. Reintjes and J. Wulff, J. Appl. Phys. **36**, 660 (1965).